

Dissertation

submitted to the

Combined Faculties for the Natural Sciences and for Mathematics
of the Ruperto-Carola University of Heidelberg, Germany

for the degree of

Doctor of Natural Sciences

presented by

Diplom-Physiker Andreas Engler
born in Frankfurth/M.

Oral examination: June 24th, 2009

Adaptive elements for STED microscopy

Referees: Prof. Dr. Stefan W. Hell
Prof. Dr. Karl-Heinz Brenner

Zusammenfassung

Moderne fluoreszenz Mikroskope sind nicht mehr durch Beugung in ihrer erreichbaren Auflösung beschränkt. Diese Eigenschaft erhöht ihren Einfluss auf die Bildgebung von zellbiologischen Objekten. Die vorliegende Arbeit befasst sich mit Verfahren, die die Eigenschaften dieser modernen Mikroskope wesentlich verbessern. Exemplarisch an stimulated emission depletion (STED) Mikroskopie wird der Einfluss des Schaltmusters für die Auflösungserhöhung und die detektierbaren Photonen durch die Nutzung eines spatial light modulators (SLM) optimiert. Mit diesem programmierbaren Werkzeug wird eine nie dagewesene Flexibilität und Qualität des Schaltmusters erreicht. Weiterhin wurde zur effizienten Abbildung von lebenden Proben mit STED ein schnelles lokal adaptives Strahlscanverfahren entwickelt, welches die Abbildungszeit um ein vielfaches verkürzt und dabei gleichzeitig die Probe schon ohne an Bildqualität einzubüßen. Dieses Konzept wurde um ein weiteres neuartiges lokal adaptives Beleuchtungsverfahren erweitert, welches das Bleichen und phototoxische Wirkungen in den Proben um ein vielfaches reduziert. Der Schutz der Probe nimmt interessanter Weise mit der Auflösung des Mikroskops zu. Die Kombination der neuen adaptiven Verfahren erlaubt die Beobachtung schneller Lebensprozesse und ermöglicht 3D Aufnahmen, die bislang durch zu rasches Bleichen verhindert wurden.

Abstract

Modern fluorescence far-field microscopes are not resolution limited by diffraction, anymore. This property increases the impact of these microscopes for cell-biological imaging. This thesis covers methods, that considerably improve the quality of ensemble scanning microscopes, a subclass of modern fluorescence microscopes. The influence of the PSF is optimized with a spatial light modulator (SLM) in case of stimulated emission depletion (STED) microscopy to increase the resolution and the signal noise ratio of the microscope. Together with a novel error correction routine the SLM provides unrivaled flexibility and quality for the generated STED-PSF. Furthermore, a new adaptive beam scanning pattern is proposed, which shortens image acquisition time and simultaneously reduces illumination load of the sample with else unimpaired image quality. This concept is extended by another novel locally adaptive illumination method, which reduces photo bleaching, dark state transitions and phototoxic effects several factors. These effects are further decreased with better resolution. A combination of these adaptive methods enables unprecedented scan times for imaging of fast dynamic processes and enables 3D STED images previously frustrated by photo bleaching.

Contents

1	Introduction to far-field optical microscopy	1
1.1	Major advancements in optical far-field microscopy	1
1.2	Image formation in confocal microscopy techniques	2
1.3	Breaking the diffraction limit	5
1.4	The adaptive concepts for STED microscopy	11
2	Adaptive STED-PSF creation	13
2.1	SLMs for STED microscopy	13
2.2	The error correction procedure	15
2.3	Experimental validation of the SLM error correction	20
2.4	The advantage of an error corrected SLM	24
3	Adaptive pattern beam scanning STED microscopy	26
3.1	Beam scanning and RESOLFT microscopy	26
3.2	Experimental implementation of the beam scanning concept	29
3.3	Decoupling beam shift and mirror rotation	32
3.4	Experimental evaluation of the QuadScanner performance	38
3.5	Adaptive scanning pattern in STED microscopy	41
3.6	Conclusions and limitations of adaptive pattern beam scanning	45
4	Adaptive illumination to reduce photo bleaching in STED microscopy	49
4.1	The reduction of the total number of switching cycles and its benefit	49
4.2	The basic principles of RESCue	51
4.3	Implementation of RESCue in STED microscopy	55
4.4	Experimental results	57
4.5	Discussion and Summary	66
5	Conclusion and Outlook	68
	Bibliography	78
A	Appendix	79

Abbreviations

2D	two-dimensional
3D	three-dimensional
AD	Alzheimer Disease
AI	analog input
AO	analog output
AOTF	acousto optical tunable filter
AOM	acousto optical modulator
APD	avalanche photo diode
APP	aminoid precursor protein
AFM	atomic force microscope
APD	avalanche photo diode
CLEM	controlled light exposure microscopy
CPU	central processing unit
cT	cycle time
CTF	contrast transfer function
CW	continuous wave
dT	pixel dwell time
DM	deformable mirror
DMA	direct memory access
D-Rex	dark state relaxation
EM	electron microscopy
FCS	fluorescence correlation spectroscopy
FLIM	fluorescence lifetime imaging
FOV	field of view
FPGA	field programmable gate array
FRAP	fluorescence recovery after photo bleaching
FRET	Förster resonance energy transfer
FWHM	full-width half-maximum
GFAP	glial fibrillary protein
GSD	ground state depletion

IO	input output
LC	liquid crystals
LED	light emitting diode
lTh	lower threshold
LUT	look up table
OP	operation amplifier
PC	personal computer
PBS	polarizing beam-splitter
PMF	polarizing maintaining single mode fiber
PMT	photo multiplier tube
PP	phase plate
PSF	point spread function
QE	quantum efficiency
RESCue	reduction of excitation and signal suppression cycles
RESOLFT	reversible saturable optical (fluorescent) transition
RMS	root mean squared
ROI	region of interest
rT	reached time
SLM	spatial light modulator
SM	single mode fiber
SN	signal noise
STED	stimulated emission depletion
T-Rex	triplet state relaxation
TFT	thin film transistors
Ti:Sa	titanium-sapphire
TPS	thin plate splines
TTL	transistor-transistor logic
uTh	upper threshold
UV	ultra violet (light)

1 Introduction to far-field optical microscopy

1.1 Major advancements in optical far-field microscopy

Cell biology aims at getting a deeper understanding of life. New insights into cellular procedures are essential to understand and cure major diseases such as cancer or Alzheimer leading to a better and longer life for human kind. Since components of and interactions within the cell can not be observed by the naked eye, the application of tools is necessary. This interest in the microcosm triggered the development of the first optical far-field microscope by Hans and Sacharias Jansen, which represents the cornerstone for still ongoing research in the field of microscope development. Hereby, the far-field light microscope holds a notable position compared to other microscopic techniques such as Atomic Force Microscopes (AFM) [1] or Electron Microscopes (EM) [2, 3], because optical far-field microscopes are capable to observe structures and processes inside living cells. The first optical microscopes were hindered by their poor contrast, which was based on absorption and reflection. This flaw experienced steady progress over the decades by developments such as the phase contrast by Zernike [4] or the dark field microscopy [5]. The major breakthrough was however the introduction of fluorescence, which provides a completely different approach for contrast generation.

Fluorescence is the spontaneous emission of a photon by a fluorophore after the absorption of a photon with a shorter wavelength due to solvent relaxation and fast radiation-less vibrational relaxation of the fluorochrome in the excited state the energy of the emitted photon is shifted to lower energy relative to the energy of the absorbed photon. This energy loss is strongly dye dependent and called after its discoverer: Stokes shift [6]. The Stokes shift hereby allows the separation of the contrast generating signal and the excitation light by the use of simple dichroic mirrors or optical filters (see fig. 1.1 and fig. 1.3). Since fluorophores can stain distinct structures of the cell the usage of them offers the possibility to produce contrast independent of absorption or refraction index variations. This concept of fluorophores as contrast agent was greatly enhanced by the invention of immuno fluorescence labeling and the discovery of fluorescence proteins as mark-

ers [7]. With the aid of fluorescent proteins, specific proteins inside the living cell can be labeled and imaged [8]. In general, the immuno fluorescence labeling uses organic dyes with a primary-secondary antibody binding to the protein of interest. This procedure has several advantages. The labeled site as well as the dye can be changed by just replacing the primary or the secondary antibody respectively. Additionally, several secondary antibodies can bind on each primary antibody. This enhances the signal and therefore the contrast. The other major labeling technique is the use of fluorescence proteins. A cell line can be transfected to produce a fluorescent protein connected to the protein of interest. This way, an immuno-labeling of the cell is not necessary anymore. By using dyes or fluorescent proteins with different excitation and/or emission spectra more than one structure can be detected simultaneously. Therefore interactions and localizations can be measured with respect to each other. The attributes of a fluorescent molecule depend strongly on its environment. Several other techniques use this characteristic to collect further information about the labeled protein structures, for example Fluorescence Lifetime Microscopy (FLIM) [9], Fluorescence Resonance Energy Transfer (FRET) [10], Fluorescence Recovery After Photo bleaching (FRAP) [11, 12] and Fluorescence Correlation Spectroscopy (FCS) [13, 14]. Although all these inventions provided more specificity and contrast to structures of interest the remaining weak elements of far-field light microscopy were its diffraction limited excitation spot and the wide field detection. The invention of the laser, high performance detection devices like the Photon Multiplier Tube (PMT) and computational data processing made the confocal microscope, first proposed by Minsky possible [15]. This microscope represents the first step to overcome this remaining limitation of optical far-field microscopy.

1.2 Image formation in confocal microscopy techniques

Contrast generation as the most important aspect in image formation

One of the key domains of fluorescence microscopy is the imaging of biological structures. To distinguish structures inside a sample the contrast of these structures is the major attribute. It is commonly generated by the difference of photon counts in the miscellaneous areas of the image. Other attributes of light such as polarization or wavelength can also be used.

A higher contrast is equivalent to higher spatial information of the object of interest. Structures cannot be resolved, if the generated contrast becomes too low. The Rayleigh criterion defines the minimum contrast at which point two point-like objects are still resolvable as 25% [16]. The resulting smallest distance between two objects still fulfilling the Rayleigh criterion is defined as resolution of the imaging system. Although the term resolution is defined arbitrarily it rep-

resents a good assumption of the spatial information which can be gained using a certain imaging instrument. The resolution represents no exact barrier of what can be resolved or not. It would not even be of relevance for an ideal imaging system with no sources of noise and infinite measurement time. Nevertheless real optical imaging systems are challenged by noise. Especially optical microscopes suffer from intrinsic Poisson noise.

The link between contrast and the PSF

One possibility to increase the contrast in fluorescence microscopy is to reduce the volume emitting the detected photons. This circumstance can be proven by the Contrast Transfer Function (CTF) [17] and is of greatest interest for optical microscopy as presented in the following.

The transformation of a point like object by an imaging system is described by its point spread function (PSF). This function denotes the illumination of the sample with $h_{exc}(x)$ and the detection of photons out of the illuminated volume with $h_{det}(x)$. Assuming a linear dependency between the excitation intensity and the emitted incoherent fluorescence an effective PSF $h_{eff}(x)$ for the entire detection process can be defined by:

$$h_{eff}(\bar{x}) = h_{det}(\bar{x}) h_{exc}(\bar{x}). \quad (1.1)$$

The smallest possible extension of h_{exc} as well as h_{det} is limited due to the wave nature of light. Hence, also the contrast of an optical system is limited. Abbe described this restriction first in 1887 [18]. In his extensive work about microscopy he showed, that the smallest possible size of a light spot produced by a lens is given by:

$$\begin{aligned} \Delta x, \Delta y &\approx \frac{\lambda}{2n \sin \alpha} = \frac{\lambda}{2NA} \\ \Delta z &\approx \frac{\lambda}{2n \sin^2(\alpha/2)} \end{aligned} \quad (1.2)$$

where λ is the used wavelength, n the refractive index, α the semi-aperture angle and NA the numerical aperture of the objective lens. Δx , Δy and Δz represent the Full Width at Half Maximum (FWHM) of the PSF in the focal plane and the axial direction of the microscope, respectively.

Today's objective lenses feature NAs up to 1.5 corresponding to semi-aperture angles of about 70° . Further improvement is restricted by the lack of usable materials and by geometrical limits. In practice the wavelength is limited to the visible spectrum above 400nm since ultra-violet (UV) light has a phototoxic

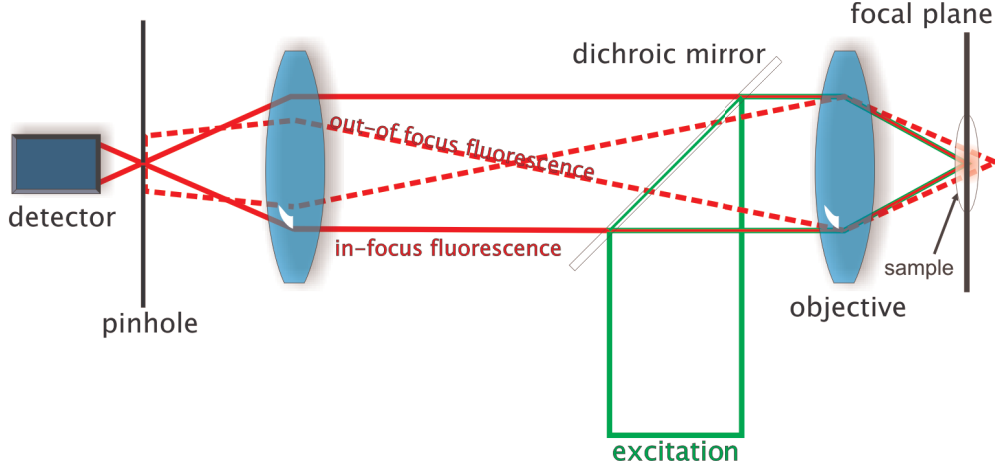


Figure 1.1: A schematic confocal setup. The excitation light is reflected by a dichroic mirror and focused by the objective lens into the sample. The fluorescent light is collected by the same objective lens, passes the dichroic mirror and is focused through the pinhole onto the detector. The out of focus fluorescence does not pass the pinhole.

effect on living cells [19]. Both aspects limit the smallest possible PSF extension for biological applications to around 140nm in the focal plane and around 450nm along the axial direction.

The confocal microscope, its advantages, its handicaps

Abbe's theorem became a dogma, which virtually inhibited the research for higher optical far-field resolution methods for a long time. However, many functional structures and processes in living cells, such as protein interactions, are in the range of a angstroms to tens of nanometers. Therefore, microscopes with a smaller effective PSF would be of highly desirable to gain deeper insights into life.

The confocal fluorescence microscope, designed by Minsky, can be considered as the first step in this direction. The confocal design is characterized by a detection pinhole, which reduces the out-of focus light introducing an h_{det} very similar to h_{exc} for pinhole sizes similar to the FWHM of the h_{exc} . Fig. 1.1 presents a sketch of a confocal setup based on the design by Ploem [20].

When the size of the pinhole decreases the number of collected photons is reduced. This limits the attainable resolution improvement with smaller pinholes. An usual tradeoff between resolution and photon collection efficiency is a pinhole size of one Airy-disk [17]:

$$\Delta r \approx \frac{0.61\lambda}{2NA} \quad (1.3)$$

The size of one Airy is exactly the diameter of the first minimum ring of the h_{exc} in the focal plane. This setting allows 80% of the fluorescence to pass through the pinhole and significantly improves the contrast along the axial direction of the microscope. For the first time 3D sectioning of cell structures with diffraction limited resolution became possible.

The major handicap which was introduced by the pinhole is that only one volume element of the sample is registered per time. The digital representation of this volume element is called pixel for two dimensional (2D) images and voxel in case of 3D scans. Classically, the image is reconstructed in a sequential way. For this case the PSF must be scanned through the sample or vice versa pixel by pixel. The time during which light is detected from each volume element is called the pixel dwell time (dT). The image is reconstructed out of all pixels/voxels. The pixel/voxel sampling of the specimen must be spatially dense enough to fulfill the Nyquist-Shannon theorem [21, 22]. For larger field of views (FOV) the scan time increases quadratically for 2D images and by the power of three for 3D scans respectively. Several concepts exist for accelerating the scanning process [23]. However, until today even the most advanced of these techniques cannot fully combine the advantages of the confocal point scanning setup and the image registration speed of a wide-field microscope. On the other hand sequential registration comes along with the advantage that highly efficient and fast detectors can be engaged. Systems like the PMT or the Avalanche Photo Diode (APD) provide high quantum efficiencies (QE), high illumination linearity and very high read-out speeds. The confocal microscope is still the gold standard for cell biology and is the vintage point for many new concepts (see next section).

1.3 Breaking the diffraction limit

The introduction of multi-photon [24–27] and 4-pi microscopy [28] extended the confocal concept. Multi-photon microscopy renders the confocal pinhole redundant as excitation is restricted to a very confined depth inside the sample. This selective excitation reduces the bleaching of the fluorophores in the out of focus regions [27]

In 4pi microscopy, a second objective lens is placed opposing the original lens for coherent illumination of the sample and therefore effectively doubling the NA. Foremost the axial direction profits from the 4pi concept by increased resolutions down to 100nm [29]. Still, the diffraction limit prohibits substantially higher resolutions for both microscopes.

The nanoscopy concept

Not until the invention of the STimulated Emission Depletion (STED) micro-

scope by Hell and Wichmann 1994 the link between resolution and effective PSF extension was broken [30]. This was the birth of a new concept in microscopy enabling new insights into cell biology [31–36].

The new concept, known as nanoscopy, relies on the dye itself to enable higher resolutions. The reason why two spherical objects cannot be resolved is that both are in the same indistinguishable state and the produced signals overlap too much. In contrast they become resolvable if they are in different detectable states, say A and B. The microscope must therefore provide a way to control these two states. During the detection of object one in "signal-giving" state A it must be ensured that the remaining objects in the diffraction limited volume are in "dark" state B. Hence, the signal produced from the object in state A can be discriminated against the signal of all other objects in state B. By sequentially switching all objects between the states A and B, the complete volume can be registered. Diffraction itself is not limiting anymore for the generation of the image contrast.

Depending on the read-out method, the states A and B, as well as the established control of the states different methods were introduced (see fig. 1.2) [37].

STED microscopy

STED can be sorted into the family of REversible Saturable Optical (Fluorescent) Transition (RESOLFT) techniques [38–40]. Another example is Ground State Depletion (GSD) [41, 42]. Exemplary for all RESOLFT techniques, the mode of operation of STED is explained in detail in the following, since all measurements in this thesis are directly related to STED microscopy. STED uses the fluorescent and non-fluorescent state of a fluorophore as state A and B respectively. These are the S_1 (first excited state, fluorescent, A) and the S_0 (ground state, non-fluorescent, B) state. Today's STED microscopes are based on confocal microscopes. Besides the excitation beam, which transfers the dye from B to A, a second depletion beam has to be implemented, which controls the transition back from A to B (see fig. 1.3a,b). The intensity distribution of this stimulated emission beam features a minimum located at the position x_{zero} . Typically, STED setups apply a doughnut shaped intensity profile with a zero at the middle for 2D and a hollow sphere for 3D resolution enhancements (see fig. 1.3b) [43–45]. Both patterns are arbitrary since other shapes such as strips are also possible. The stimulated emission generates photons with lower energy than the fluorescence photons. Hence, these photons do not disturb the detection of state A. The control patterns are scanned sequentially through the sample. At each pixel/voxel the excitation transfers all fluorophores inside the diffraction limited volume into state A, followed directly by a STED beam, which transfers all dyes which are not located at x_{zero} into state B. Hence, all detected photons must have been originated from the location x_{zero} . This concept is called ensemble switching, as more than one fluorophore can be located inside

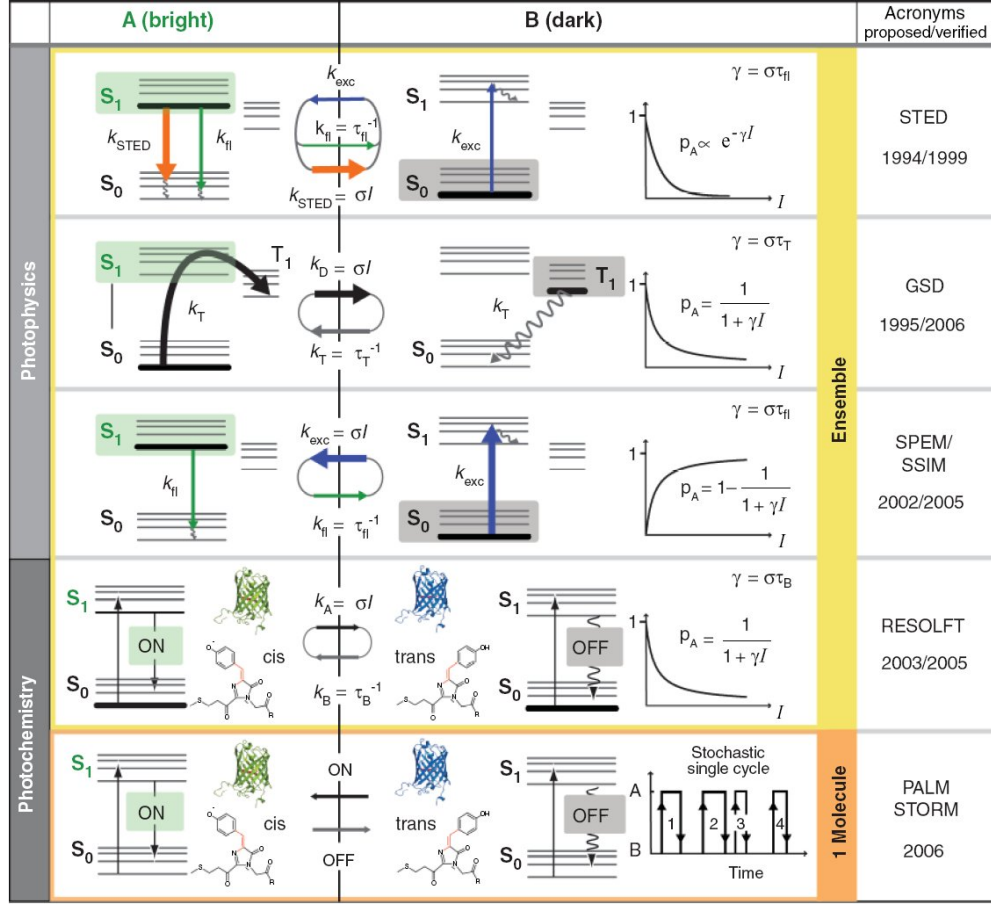


Figure 1.2: Overview of commonly used nanoscopy techniques. They are sorted on the left side to their switching mechanism and their read-out modality to the right. In each group further discriminations are possible mainly by the actually used transition between the state A and B (adapted from [37]).

the non depleted volume and therefore contribute to the photon signal. The size of this volume and therefore the resolution depends mainly on the efficiency of the transition from state A to state B. A more theoretical approach bases on the rate equation for the state A in areas outside x_{zero}

$$\frac{dN_A}{dt} \approx \sigma_1 I_{exc} N_B - \sigma_2 I_{STED} N_A, \quad (1.4)$$

where $N_{A,B}$ represents the population of each state, I_{exc} and I_{STED} represents the excitation and depletion intensity, and $\sigma_{1,2}$ depicts the cross section of the fluorophores for absorption of a excitation or a depletion photon respectively. This differential equation demonstrates that the efficiency of the depletion transition can be increased by higher STED intensities or a higher cross section for the depletion transition.

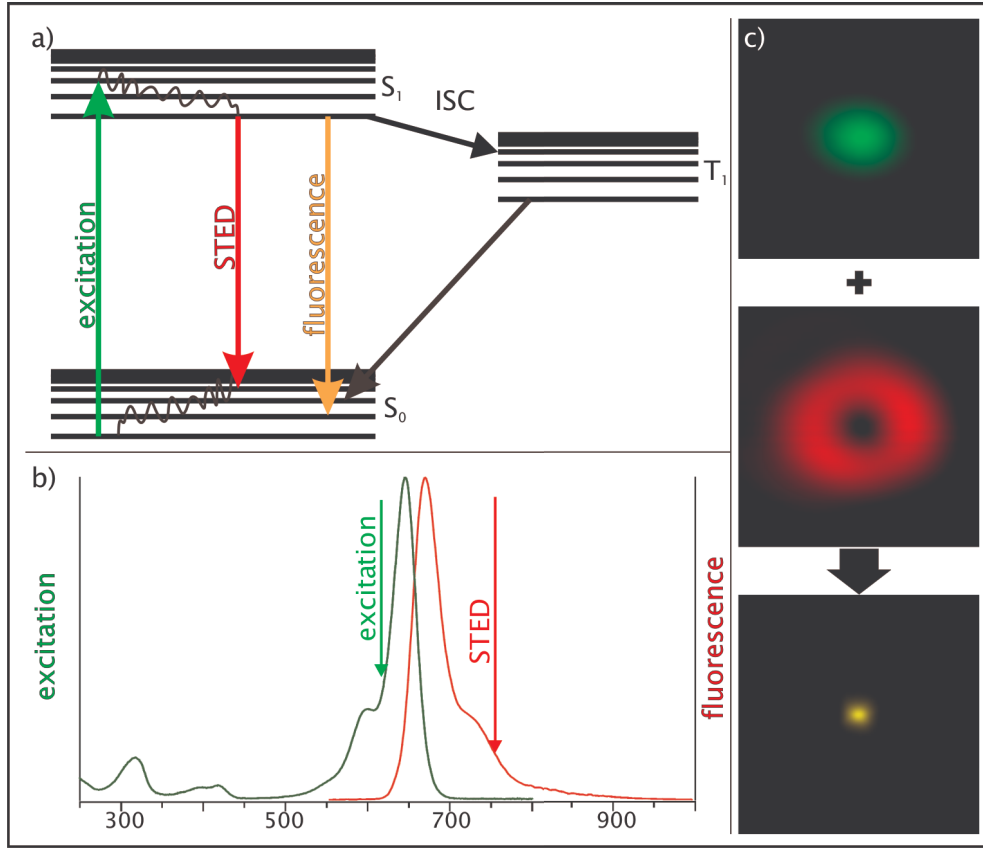


Figure 1.3: Fluorescent dyes enable high contrast and specific labeling of proteins and provide the foundation for STED. Due to the Stokes shift a fluorescent dye emits photons with lower energy than the energy provided by the excitation photon. So the fluorescence photons can be distinguished by the longer wavelength (a,b). The STED pulse depletes excited molecules with even longer wavelength down to the ground-state (a,b). An inter system crossing (ISC) to the triplet state could be a pre-step for photo bleaching (a). The excitation PSF in xy is a single Gaussian beam (c, green). The STED beam is typically transformed to a doughnut mode (Gauss-Laguerre₀₁ mode) with a minimum in the middle to deplete fluorophores located everywhere but x_{zero} (c, red). The remaining volume of fluorescence is restricted to a much smaller size.(c, yellow).

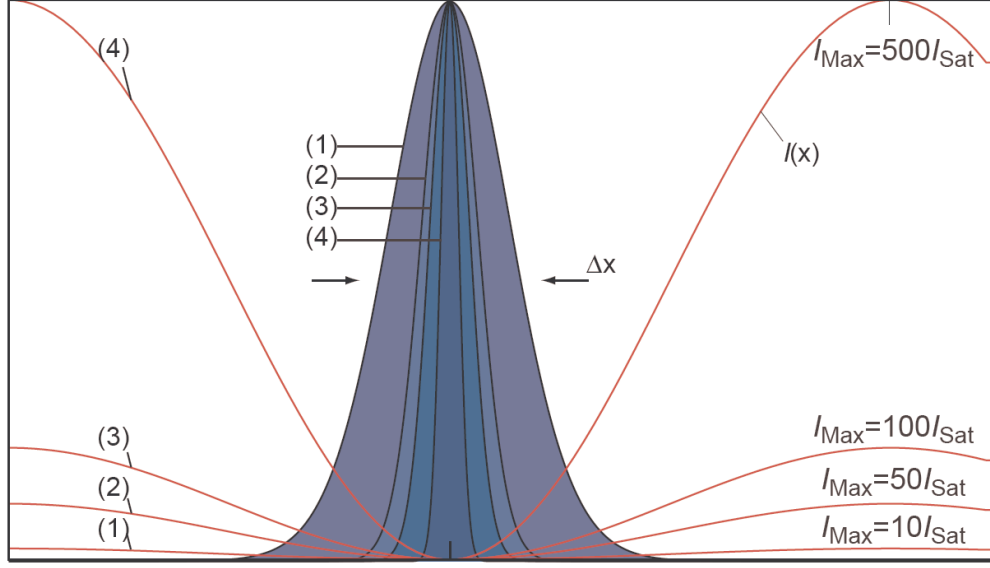


Figure 1.4: The figure illustrates the saturable STED effect for different STED intensities compared to I_S (1-4). With higher STED intensities the probability increases that fluorophores localized near x_{zero} are depleted to state B. Therefore the effective PSF is reduced (adapted from [47]).

Stimulated emission competes against the spontaneous fluorescence emission. With a fluorescence lifetime of τ_A of the state A a saturation intensity can be defined by $I_S = (\tau_A \sigma_1)^{-1}$ for which half of the population is quenched to the ground state before fluorescence can occur. With $I_{STED} \gg I_S$ an effective depopulation of state A can be ensured and the fluorescence is confined to the position x_{zero} (see fig. 1.4). The combination of the lateral resolution of a confocal system Δr and the assumption of a quadratic steepness of the minimum located at x_{zero} results in the lateral resolution of the STED microscopy Δr_{STED} [46]:

$$\Delta r_{STED} \approx \frac{\lambda}{2NA \sqrt{1 + \Delta r a^2 \frac{I_{STED}}{I_S}}}. \quad (1.5)$$

Attributes of STED microscopy

Since the intensity as well as sometimes the cross-section can be adjusted the resolution of the system can be controlled and is only limited by the laser power available and the bleaching of the dye. Since A is in the order of 10^{-9} s for common fluorescent dyes the STED intensities applied for decent resolution improvements are in the order of hundreds of MW/cm². These high laser intensities are not deposited in the specimen. Ideally the photons of the STED beam are not absorbed but only induce stimulated emission. It can be stated that STED even

with high power beams is reasonable well compatible with live cell measurements [48]. Still, an excited fluorophore hit by a STED photon has a certain probability to bleach, mainly through the triplet channel [49]. In this case, not only the energy remains inside the specimen but the dye cannot further contribute to the signal.

A phase mask or a phase modulation element such as the spatial light modulator (SLM) shapes the actual intensity distribution of the STED PSF. An imperfect implementation of the minimum limits the maximal achievable resolution and contrast, since the depletion transition would deplete also fluorophores which located at x_{zero} in such a case resulting in less detectable signal from state A (see chapter 2) [46].

Different nanoscopy concept in comparison

Instead of the ensemble read-out technique with its confocal approach a stochastic read-out employing wide-field detection can be performed. It ensures sequential detection inside each diffraction limited volume by sparse illumination. This illumination must ensure that in each illumination PSF volume only one single dye molecule is turned to state A per detection cycle. By collecting sufficient photons of this single marker the position can be localized with high accuracy [50]. Localization of single events has been widely used before. Triggered by the discovery of new fluorescent proteins [51] the localization resolution becomes possible for imaging by sequentially detecting each dye molecule by the use of several wide-field images and a later reconstruction of all localized marker into one image. Till today several tricks were implemented to ensure a sequential stochastic read-out [52–54]. Each stochastic method as well as all RESOLFT methods has its own advantages and disadvantages.

In the case of RESOLFT, the position of the fluorescence is confined by the applied pattern which has to be scanned over the specimen. Small FOVs can therefore be scanned very fast, enabling the measurement of rapid dynamics inside living cells [36]. Due to the switching pattern and the confocal nature of detection 3D resolution enhanced nanoscopic images are possible [45]. Combined with 4pi microscopy, the ensemble technique delivers even isotropic high resolution 3D images [44].

STED can use conventional dyes and has the advantage to tune its resolution by the depletion beam intensity (see chapter 3). However the scan process contains certain disadvantages like long image acquisition times for large FOVs and a high number of excitation and depletion cycles of each fluorescent molecule (see chapter 3 and 4).

The stochastic methods record the complete specimen but only a fraction of the dye molecules per switching process. A common way to prevent redundant registration in the same reconstructed high resolution image is to bleach the fluorophore during the localization, which can lead to sparse sample feature

representations in repetitive scans. As 2D detectors become faster these methods will gain linear until the fluorescence lifetime of the dye becomes limiting. However, very high resolutions can only be achieved with very stable dyes because not the applied laser power controls the resolution but the number of collected photons. The achieved resolution depends on the number of photons collected.

1.4 The adaptive concepts for STED microscopy

STED microscopy is a rapidly growing field of research. Designed as an imaging instrument for cell biology its key benefit is the higher resolution compared to confocal microscopy by else equal conditions. However, the field of applications of most of today's STED microscopes is limited by the used hardware and intrinsic attributes of STED. Foremost, as mentioned before, the quality and the shape of the minimum of the STED depletion pattern have a major impact on the performance of the system [46, 47]. A corrupt implementation of the minimum reduces the number of collectable photons and the resolution of the system. Precisely fluorescence images of rapid dynamic movements and imaging of fluorescent proteins needs the maximum achievable contrast and resolution for later biological interpretation of the recorded images.

The common way to introduce a minimum inside the STED PSF is by interference effects introduced into the beam by phase masks. Static patterns cannot compensate for the errors of the rest of the system or even the errors introduced by themselves. Hence, an investigation of spatial light modulators (SLM) as phase pattern generators for STED microscopy is performed in the following chapter. These devices are freely programmable and provide therefore the possibility to apply arbitrary phase masks and to pre-compensate for setup aberrations. Using such a device provides the freedom to test new phase masks with very little effort. Yet, the quality of commercially available SLMs renders them useless for STED phase mask generation. Hence, a novel error correction process is proposed and evaluated (see chapter 2). For the first time, the usability of such an error correction is demonstrated at STED measurements.

Besides the optimal STED resolution performance the image acquisition speed is another major factor for the usefulness in biological applications. The observation of fast dynamic processes and 3D structures of living cells are the most important fields of application for a far-field microscope. A STED setup based on a stage scanner cannot deliver the necessary image acquisition speeds. Recent publications introduced beam scanning concepts for STED microscopy and demonstrated the advantages of such an approach [34–36].

For the first time, a beam scanner for STED based on galvanometers is presented in chapter 3, which delivers the highest ever announced image acquisition speed

for biological samples. The scanner provides this high performance by using a novel adaptive scan pattern approach, which does not decrease the image quality compared to a normal scan. This approach can only be applied in ensemble switching high resolution microscopy. Besides the image acquisition time reduction, demonstrated by a factor of 13 compared to a normal galvanometer scanner, the adaptive beam scanner reduces the light dose applied to the sample and therefore reducing bleaching and dark state transitions of the fluorophores.

However, even high resolution and image acquisition speed are useless if the fluorophore is photo bleached or phototoxicity introduces artifacts during the image registration. Therefore, the influence of illumination regarding photo bleaching and dark state transitions is a major topic of ongoing research [55–59]. Repetitive and 3D scans as well as the usage of fluorescent proteins, call for low bleaching image registration methods. Actual STED systems need many more excitation and depletion cycles for image creation than a for example a stochastic read-out microscope. These switching cycles are closely related to bleaching and dark-state transitions (see chapter 4). Hence, the idea behind the adaptive beam scanning was transferred to an adaptive dT measurement in chapter 4. There, a novel approach is presented to reduce the total number of switching cycles needed for image generation. This method reduces the switching fatigue of the fluorophores thereby reducing the photo bleaching up to a factor of 12 compared to a normal STED scan and enabling 3D measurements of biological samples.

The resulting STED microscope provides an adjustable high quality STED intensity pattern. In combination with the newly proposed adaptive beam scanner the methods enable fields of biological relevant applications for high resolution STED imaging, which are otherwise not possible to achieve. In addition, the introduced adaptive beam scanning STED and the adaptive reduction of the switching cycles can be combined also with other methods to deliver an image acquisition speed and a bleaching behavior which is even outperforming a confocal microscope.

2 Adaptive STED-PSF creation

2.1 SLMs for STED microscopy

The last chapter emphasized the major role of the PSF with respect to the microscope performance (see section 1.2). In case of STED microscopy the form of the depletion PSF and the quality of its minimum greatly influences the effective PSF of the microscope (see section 1.3). Regarding these circumstances it is of great interest to have a device, which gives control over the STED PSF. With the spatial light modulator (SLM) this chapter will introduce such a device. Since the wave front exactness of most SLMs is unacceptable for STED PSF creation, a procedure is implemented to correct for erroneous phase generation and give rise to programmable aberration free depletion patterns.

The use of SLMs in STED microscopy

The so far introduced ensemble switching high resolution microscopy needs a control pattern with a minimum located at x_{zero} . The shape and quality of the minimum is essential for the performance of the microscope. In case the produced intensity profile is asymmetric or even the minimum is substantially worse than 1% the effective PSF becomes asymmetric accordingly and with it the maximal fluorescence signal and the resolution of the system [60, 61].

The intensity pattern for actual STED microscopes is generated by imprinting a phase pattern onto the depletion beam of microscope. Most conventional phase masks are made of vapor deposited structures on glass or tilted coplanar glass plates depending on the phase mask structure[45]. The creation of more complex phase structures is conjunct with considerable efforts to minimize the introduced wavefront errors [62].

Adaptive optics represents an alternative to conventional phase masks. Since some of these devices can produce any spatial phase shift mask they are convenient for phase mask testing and additionally provides the opportunity to correct for optical aberrations of the STED beam [63–67] .

Major criterions for SLMs

The devices usable for phase mask generation can be categorized in two major classes. One of them consists of deformable mirrors (DM), which apply actuators beneath a flexible mirror to control the position of the surface with respect to the neighbor actuators [67]. The other class consists out of liquid crystal (LC)

devices.

Besides intensity modulating LC SLMs mainly used for holographic illumination [68], phase only modulating LC SLMs are commercially available [69]. For an easier understanding the term SLM classifies just phase only modulating LC SLM in the further work.

DMs have certain advantages over SLMs as they have a higher fill-factor, faster update rates and they can introduce larger phase shifts. Nevertheless, the relatively low number of interdependent actuators makes them less attractive for STED phase mask generation [70]. Instead, SLMs provide a very high number of actuators in form of mostly independent pixels. In case of a common SLM the LCs are aligned in parallel and an applied voltage leads to an according refractive index variation [69]. In total the single phase shifts introduced per pixel form a phase mask for coherent light.

In this work SLMs from two different suppliers were analyzed. The SLMs are based on different techniques. One uses a continuous LC layer which is optically structured by a back illuminated intensity pattern which in turn is generated by a LCD display. The image is cleared of high frequencies to suppress ringing from diffraction patterns. The advantage of concept is a very high fill-factor compared to SLMs of other vendors. Yet, the incompatibility to produce sharp phase steps, respectively high frequencies can hinder the generation of certain phase masks. The other used group of SLMs analyzed applies the classical concept of LCDs to LC cells with parallel aligned crystals. Hence, the SLM provides a higher update speed to around 30Hz instead of 1Hz and has no problems with sharp edges. According to the thin film transistor (TFT) concept these SLMs provide only a fill factor of around 84% and produce diffraction patterns.

The needed error correction process

Both device classes often provide not the necessary wavefront exactness for effective depletion pattern generation, as the typical wavefront error is not better than $\lambda/4$. In the past years several methods for error correcting SLMs were proposed [62, 71]. Foremost, the method presented by Xun et al. provided a pixel wise calibration of the SLM for the complete usable phase range [72].

Firstly, this calibration method is greatly enhanced by combining it with a polynomial fit algorithm. Furthermore, the exactness of the error correction according to phase shifting interferometer is increased by a factor of around 2. These advancements made it possible to apply the error correction to enable STED measurements with unrivaled resolution [73, 74]. Further on, the newly proposed method is much more suitable for SLMs with high resolutions, commonly used in diffraction alignments [75].

In the following the error correction procedure is shown. In detail, the optical setup applied for SLM characterization is disclosed. It can be used with two phase reconstruction methods. The optimized correction method is described for

these two modes of operation. The error correction capability of both methods is compared with measurements of the produced phase. To characterize the influence of the error correction with respect to the STED performance, PSF measurements demonstrated the usability of the introduced method with low STED intensity for the first time. Finally, the influence of an error correction for a SLM is distinguished under real STED conditions with a doughnut shaped intensity pattern by measurements of fluorescent beads for the first time. These fully corrected SLMs are not only capable to produce high quality phase mask but can also be used to pre-correct for setup aberrations (see appendix A).

2.2 The error correction procedure

The optical setup

Continuous wave (CW) laser diodes with different wavelength (532nm, 635nm, 650nm, 750nm, Roithner, Austria) were used to illuminate the SLMs/reference mirror placed in a Michelson interferometer. For later beam-splitter compensation, the SLM, respectively the reference mirror, could be positioned exactly at the same position by using the very short coherence length (below 5 μm) of a common light emitting diode (LED). Each of the mentioned lasers was coupled into 2m single mode fiber (SM) (ThorLabs, USA) to generate a planar wavefront. After collimation and polarization cleanup by a polarizer, the laser beam was split by a 50/50 beam-splitter (both: B.Halle, Germany) into the two arms of the Michelson interferometer. One beam hit the SLM (PAL-SLM, Hamamatsu, Japan or P512, Boulder Nonlinear Systems, USA) or a $\lambda/20$ reference mirror (20Z40, Newport, USA) positioned onto a linear stage for coarse beam path adjustments (M-443, Newport, USA); the other illuminated a $\lambda/20$ precision mirror positioned onto a piezo linear stage with a repetitive position precision of 0.1nm (P-752.11C, PI, USA). The interference pattern was imaged by a charged coupled device (CCD) camera (A641f, Basler Vision, Germany). In the intensity calibration mode (see section) the polarizer could be rotated to 45° with respect to the extraordinary axis of the liquid crystals (LC) of the SLM and an additional analyzer (B.Halle, Germany) was positioned ahead of the detection unit. Fig. 2.1 shows a schematic of the calibration setup.

Phase reconstruction

After the error correction of the SLM it should produce the desired phase shift for each pixel. The generated phase shift is controlled by the voltage applied to the pixel which itself is actuated for both vendors by an 8-bit control gray value. As result the calibration delivers for each pixel the correct gray value which must be applied to the SLM to produce the desired phase shift. The capability to measure the generate wavefront is the first step to error correct the phase

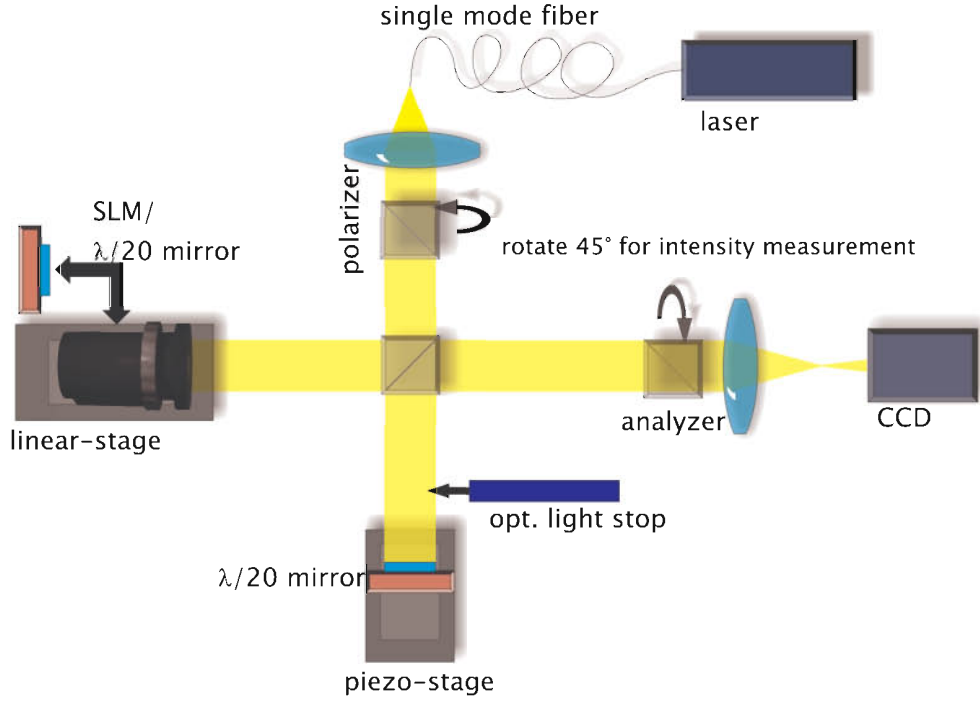


Figure 2.1: A schematic drawing of the calibration setup. It can be operated in intensity and interference mode by rotating the polarizer and analyzer by 45°. The collimated light of a single mode fiber coupled diode laser passes collimated the polarizer and is split in the Michelson interferometer arms. It hits the SLM or a reference mirror positioned onto a linear stage for beam path adjustment in one arm. In the other arm the light is reflected by a reference mirror positioned on a piezo-stage for phase shifting in case of interference measurements. In case of intensity calibration this beam path is blocked by a light stop. Coming out of the Michelson interferometer the light passes the analyzer and is detected on a CCD camera.

modulation device.

Currently commercially available Hartmann-Shack wavefront sensors, however inexpensive, do not provide a sufficient resolution to measure the produced phase masks of the used SLMs. Actual phase stepping interferometer, mainly used for quality control mostly do not provide the geometrical conditions to calibrate the SLMs. Instead a phase reconstruction method proposed by Xun et al. was implemented and refined [72].

With an intensity and an interference measurement the phase reconstruction is based on two different techniques. For both methods, a homogeneous phase value is set to all pixels of the SLM, and the actually generated phase by each SLM pixel is measured with the respective method. This measurement is repeated at equidistant control gray value steps, typically 32 over the whole range of 256 gray values. The number of steps can be provided by the user. For both modalities a

camera records one or four intensity images of the SLM pixels at each of the 32 sample points. The introduced transformation between camera and SLM pixels is compensated by use of a calibration image to obtain the necessary parameters for the inverse transformation. Besides an affine transformation in homogenous coordinates the option to use a nonlinear warping algorithm based on thin plate splines (TPS) was provided [76]. In both operation modes the applied wavelength defines the measured phase modulation.

Intensity measurement

For the intensity measurement the mirror in the interferometer arm is blocked to the light. The analyzer is placed before the detector with an angle of 45° between the extraordinary axis of the SLM and its polarization axis (see fig. 2.1). Further on the polarizer is rotated by 45° . Therefore, the polarization vector between the laser light irradiating the SLM and the extraordinary axis of its LCs include an angle of 45° . Since the LCs are parallel aligned a part of the light is delayed and therefore the polarization is transformed from linear to elliptic to circular and back again according to the introduced phase shift of the SLM.

Without phase shift the analyzer is parallel oriented against the incident light and the illumination reaches the detector. As a result the phase modulation is transformed into an intensity modulation according to Malus' law [16] (see fig. 2.2a). The phase can be reconstructed via a set of transformations. At first, the 1D intensity function recorded for each pixel at position x,y for each phase step i : $gray(i)_{x,y}$ is normalized to -1 to 1 (fig. 2.2b). Since the intensity is probably under-sampled the measured minimal and maximal intensity values has not to represent the actual minimum and maximum. This circumstance can introduce errors during the normalization routine. Second, an arcsin transformation reconstructs the phase out of the normalized intensity values (fig. 2.2c). As the arcsin function is not unique we must assume that the produced phase modulation is monotonic increasing. This provides us with the necessary transformation to correct the phase to its final form (fig. 2.2d).

The reconstructed phase holds the complete information of the phase shift introduced by the LCs. Yet, all not birefringent materials such as the coverslip as well as the reflective surface at the back of the LC induce further constant phase shifts not measurable with the intensity measurement.

Interference measurement

The mentioned disadvantages of the intensity measurement made it obligatory to provide a possibility in the calibration stand to measure the total phase modulation introduced by all parts of the SLM. For this purpose the shutter is removed from the previous calibration setup and the analyzer and the polarizer are rotated to 0° compared to the LCs. To be able to obtain interference fringes, the path-length in both arms have to be matched by the coarse stage to less than

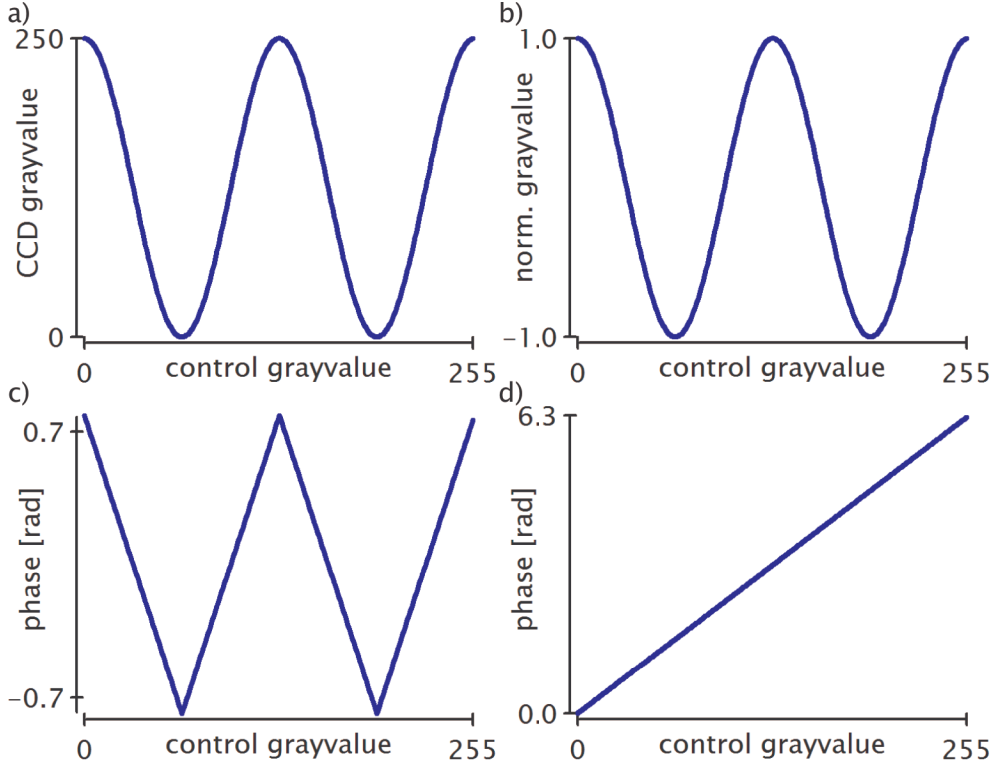


Figure 2.2: The figure illustrates the simulated different stages of phase reconstruction for the intensity calibration. Starting with the detected intensity on the CCD (a) this intensity modulation is normalized in a first step (b). Thereafter an arcsin function is applied (c). In the last step, the assumption of a monotone increasing phase results into the final phase representation (d).

the coherence length of the light-source employed. The optical path length in one of the arms of the generated Michelson interferometer can be altered fast and with a precision of 0.1nm by the linear piezo stage (see fig. 2.1). This so called phase shifting interferometer provides the possibility to reconstruct the phase difference of both interferometer arms by four sequential intensity measurements [72]:

$$phase(i)_{x,y} = \arctan 2 \left(\frac{I(i)_{2,x,y} - I(i)_{4,x,y}}{I(i)_{1,x,y} - I(i)_{3,x,y}} \right) + n2\pi \quad (2.1)$$

where $I_{1..4}$ represent intensity values recorded each with a phase shift of $\lambda/2$ in succession at the positions x, y . i represents one of the 32 sample points. Phase errors introduced by the piezo stage as well as vibrations cannot be compensated for. However, drifts between different applied gray-values can be compensated with the following described process. Three corners of the SLM remain with a constant phase while the phase ramp is applied to the rest of the SLM pixels.

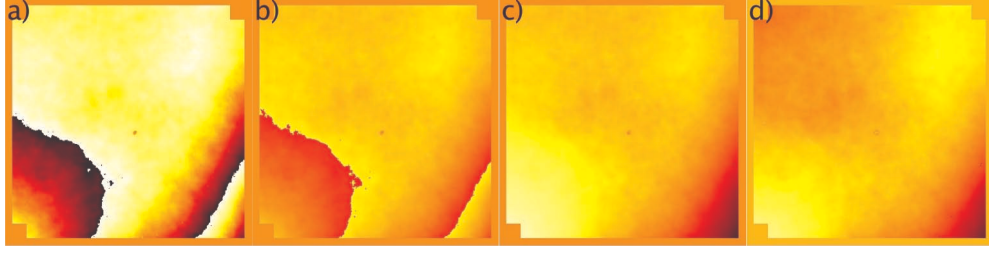


Figure 2.3: The images represent the reconstructed phase after different computation steps at some phase point in the middle of the measured phase ramp. First the raw phase-step reconstructed phase is shown (a). After a 2D unwrapping of the very first phase image further 2π jumps can occur for each pixel (b). These jumps are compensated during a fast 1D unwrapping algorithm for each pixel starting at the first image (c). Finally the drift in x,y and the beam splitter can be compensated (d).

Constant optical path differences of the setup, drifts and tilts in the x- and y-direction can therefore be compensated afterwards. In contrast to the method proposed by Xun et al. this method significantly improves the absolute error correction of the SLM. The interference phase reconstruction measures the over all optical path difference. The method cannot distinguish between phase shifts introduced by SLM components or differences introduced by the remaining optical components such as the mirror in the other interference arm or the 50/50 beam-splitter surfaces. For the first time the proposed method provides the option to compensate for these effects. For this purpose the measurement is split into two parts. In a first step a reference mirror is stationed at the SLM position. Both mirrors utilized provide a $\lambda/20$ surface quality. An interference phase shift measurement with these mirrors in both optical paths will consequently supply the phase difference of the setup paths with an exactness of around $\lambda/14$. In a second step the SLM is positioned at the reference mirror slot and the described calibration routine is performed. Afterwards the constant errors introduced by the optical components can be compensated for according to the reference mirror measurement.

The so reconstructed phases incorporate 2π jumps (see fig. 2.3a). A 2D unwrapping of the first 2D phase image of the SLM [ref.] and a 1D unwrapping of each pixels phase function afterwards [ref.] unravels these discontinuities (see fig.

First, the generated phase shift as a function of the applied control value has to be inverted. Second a 5th order polynomial is fitted to this *controlvalue(phase)* function (see fig. 2.4b). Fortunately, all investigated SLMs showed no significant errors according to the fit.

Instead, simulations showed a superior performance of a least square fit with polynomials of 5th order against bilinear interpolation between the next neighbor

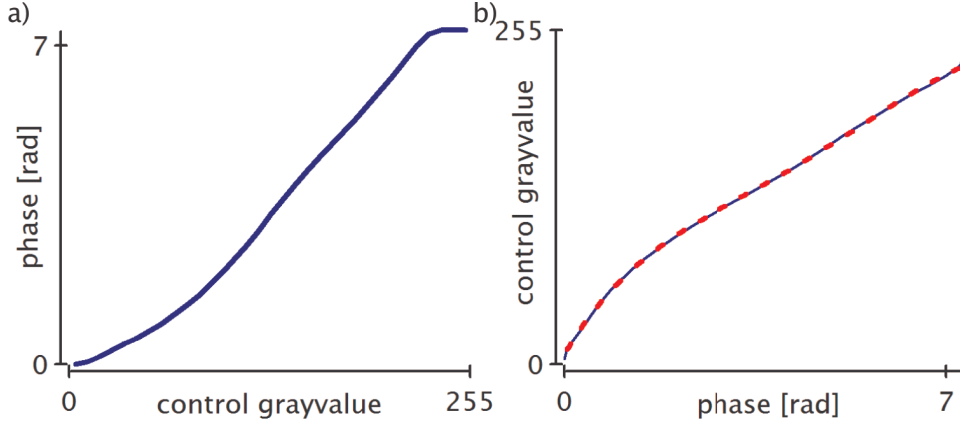


Figure 2.4: The figure shows the principle approach to fit each pixel's phase response with a polynomial of 5th order. On the left a typical phase response of a single SLM pixel is presented (a). On the right this phase response function is inverted (blue) and fitted with a polynomial of 5th order (red dotted) (b). The typical fit error is below 4 gray values in maximum.

phase points in case of 32 phase sampling points (data not shown). Hence, only the six coefficients of the polynomial must be stored for each pixel. This is a reduction of needed storage space by a factor of 42 compared to a LUT for all 256 grayvalues.

2.3 Experimental validation of the SLM error correction

After the error correction procedure the direct measurement of the SLM generated phase shift in the Michelson setup offers a possibility to verify the performance of the described approach. Since no altering elements like different specimen preparations, different alignment in the microscopic setup or high laser intensities are introduced this measurement delivers the most accurate performance check of the error correction method at disposal.

Nevertheless, error correction and check of the error correction were performed with the same procedure. The possibility exists, that errors introduced by the interference phase shifting method were not discovered.

To validate the repeatability the phase offset of both reference mirrors were measured for six independent adjustments and compared. The maximal error encountered was 0.12rad. The typical mean root mean squared (RMS) over all measurements was 0.1rad. Compared to the $\lambda/14$ exactness due to the mirror precision the error introduced by the other components such as stage positioning

errors or vibrations were negligible.

The importance of the SLM devices for STED lies mainly in the PSF generation for the STED depletion beam. Consequently, a validation of the resulting PSF has to be performed to determine the influence of phase errors for the Laguerre-Gauss₀₁ mode. Finally, all described effort for the SLM error correction is only expedient if the actual STED performance is increased.

Direct error correction checking

The error correction was performed with seven different SLMs from the two distinct vendors. Both vendors used an 8-bit control signal to modulate the LC voltage. The phase shift sampling was performed with the proposed 32 steps for the complete phase modulation ramp. Since the intensity calibration conceals the constant offsets only a subgroup of SLMs were calibrated via this modality and compared against the interference calibration. Depending on the SLM a different amount of offset error was introduced in comparison to the interference calibration. Typical errors introduced were in the order of $\lambda/6$ and formed smooth functions in x,y (see fig. 2.5). According to these circumstances all further results will implicate only interference measurement data.

The quality of the complete applied interference error correction for different SLMs and vendors was compared. The calibration significantly reduced the produced error of all SLMs. An improvement of up to a factor 11 RMS error reduction was generated. Typical factors were around 6-7 for all SLMs. In absolute values the mean RMS-error was reduced from over 100nm to around 10nm (fig. 2.6). This implied exactness better than $\lambda/50$, which had to be limited to $\lambda/14$ due to the mirrors deployed in the interferometer setup. To verify the assumption of linear wavelength dependency one SLM of each vendor was calibrated at a minimum of two different wavelengths. The measured phase modulation can be compared providing the wavelength information. Since the observed error is similar to the typical generated measurement error due to the interference calibration it is believed in a linear wavelength dependency of the typical SLM (data not shown).

Point spread function measurements

Encouraged by the greatly increased accuracy of the SLMs due to the interference calibration the PSF generation capability of the SLM was measured directly in the STED setup described in section 3.2. The PSF were measured by reflected light at gold spheres (see appendix A) without a pinhole. To achieve a fair comparison the SLM was optimized each time by phase offset and phase range modulation. The doughnut shaped PSF with out and with calibration shows dramatic differences in symmetry (see fig. 2.7). This difference should result in a more uneven intensity distribution for further fluorescence measurement with a

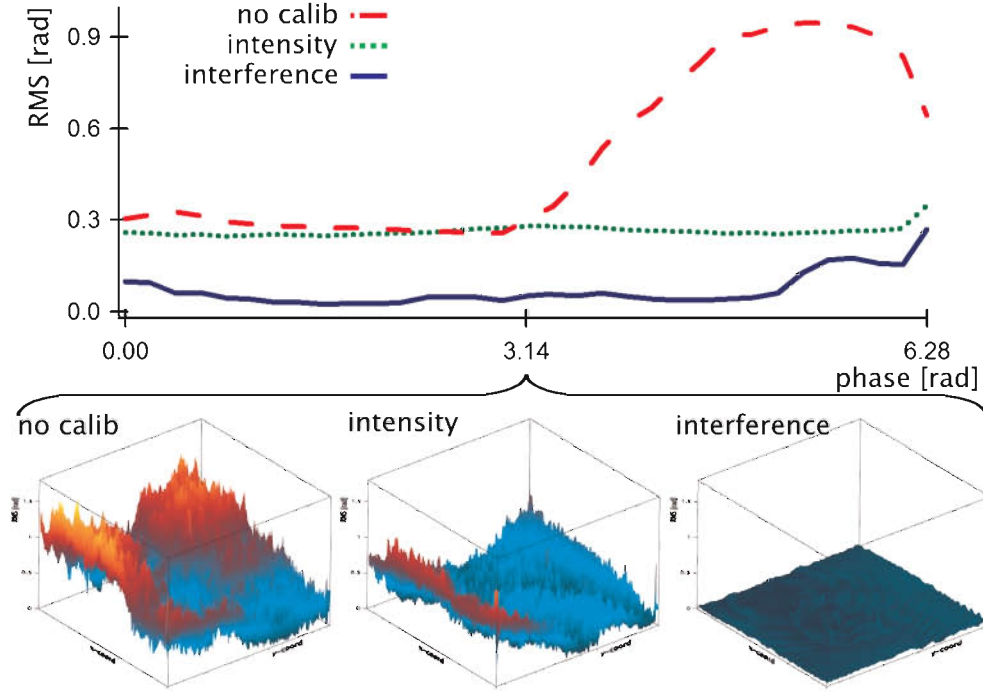


Figure 2.5: The figure presents the root mean square error between the applied uniform phase and the produced phase for the SLM in the raw state from the vendor (red, no calib), in the intensity calibrated state (green, intensity) and in the interference error corrected state (blue, interference). It can easily be seen that the interference calibration provides over the complete phase shift a much better performance than the intensity error correction procedure. However, both methods perform clearly superior to the SLM in its not corrected form (upper row). The same holds true for the 2D RMS distribution over the SLM at a phase shift of π (lower row).

resolution difference between these two vectors (see fig. 2.8). However, even the not calibrated SLM provided a similar minimum intensity in the middle of the PSF (fig. 2.7).

STED performance comparison

The information gained from the PSF measurements were further increased by real STED measurements. The measurements were performed with the STED setup described in chapter 3. For an ideal performance comparison between different modes of operation the sample should introduce no additional effect. Fluorescent beads provide near spherical objects with little bleaching and no dipole effects [77, 78]. According to the lasers applied for the STED measurements Fluospheres polystyrene microspheres [Invitrogen, USA] with Crimson fluorescence

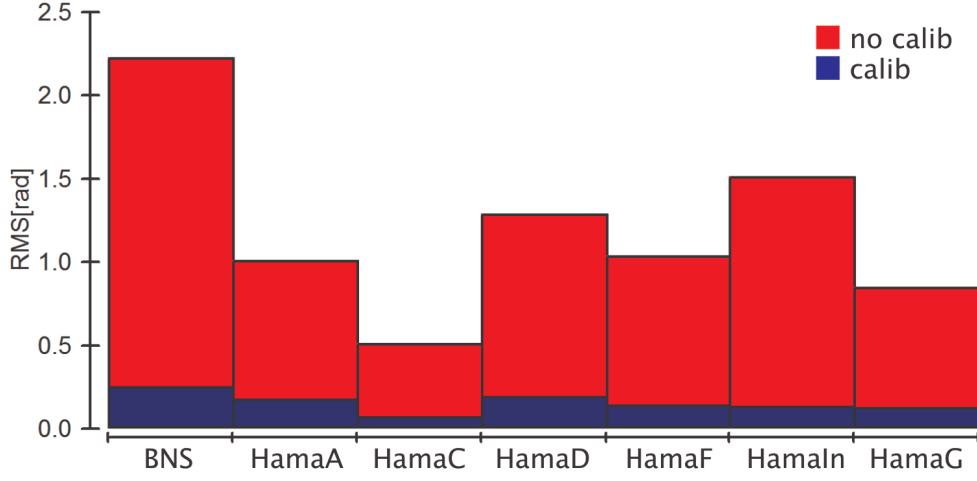


Figure 2.6: The error correction reduces the overall error of all SLMs significantly below $\lambda/14$ no matter, which error was produced by the SLM in its original state.

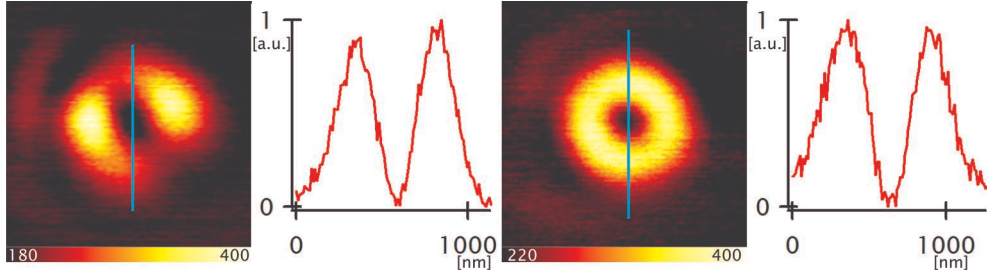


Figure 2.7: The PSF produced by the SLM without calibration was asymmetric (a). This should reduce the maximal achievable performance. After calibration the SLM provides a nearly perfect doughnut shaped STED PSF (b). However, the minimum of both STED PSFs are comparable in quality.

and a typical size of 36nm were utilized as sample (see appendix A). The excitation laser power was measured to around $50\text{W}/\text{cm}^2$ in the focus. The STED power was set to around $250\text{MW}/\text{cm}^2$ accordingly. The Crimson beads were recorded first in confocal mode with a pixel size of 50nm at a pixel dwell time of 200 μs . Second, a STED image with a error corrected SLM (calib) and finally with the same SLM not error corrected (no calib) were recorded. For the latter two the pixel size was reduced to 20nm, with the same pixel dwell time. Assumed to be linear, bleaching influences were minimized, by measuring a second sequence with reversed STED image order. Images belonging together were summed for an easy comparison (fig. 2.8). A close look exposes a signal to noise increase of around 25% and a more spherical representation of the beads due to the error correction at certain areas of the image (fig. 2.8 no calib, calib). Furthermore,

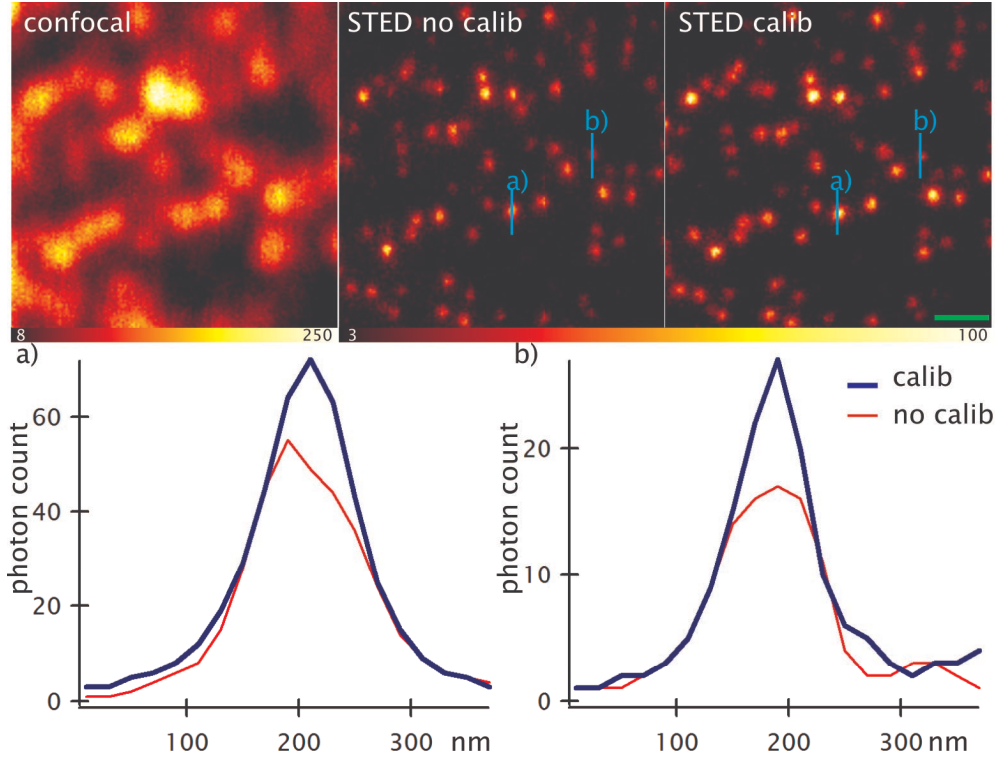


Figure 2.8: The figure demonstrates the influence of the SLM error correction at STED images of fluorospheres. An improvement in resolution in one distinct axis was achieved by 20%. This asymmetry in resolution increase due to STED without error correction was predictable as the not error corrected SLMs incline to asymmetric intensity distributions for the STED PSF (see fig. 2.7). The scale bar corresponds to 500nm.

the resolution was slightly increased by a factor of around 1.2 along one direction inside the focal plane.

2.4 The advantage of an error corrected SLM

In conclusion, the SLM error correction provides a guaranteed phase reproduction of $\lambda/14$ RMS for all calibrated SLMs at all usable wavelength. This result was only limited by the utilized $\lambda/20$ reference mirrors. With more accurate mirrors exactness down to $\lambda/50$ should be possible. Compared to the typical precision provided by the vendors the calibrated SLM delivers up to six times better performance. A measurable improvement both in PSF exactness as well as signal to noise during image acquisition with a STED microscope could be verified. Additionally, even if the SLM provides with vendor exactness an accurate STED

performance the actual produced phase modulation can only be checked in the calibration setup. Comparing the complexity and cost of a STED setup against the calibration stand one can ensure the SLM performance beforehand at the calibration stand. This way time and costs can be saved for the planning and construction of the actual STED setup.

The calibrated SLM can be used to test different phase plates and to compensate for STED beam path aberrations. For a two color STED setup the SLM could provide the phase plate for both colors sequentially.

The intensity measurement should provide a possibility to ensure a calibrated phase ramp of each SLM pixel even in the STED setup. However, each pixel's phase offset has to be measured beforehand or compensated by the use of offset aberrations. In addition we described a new variation of phase shifting interferometer calibration which is capable to ensure SLM phase modulation exactness without the use of an intensity measurement and even for high resolution SLMs.

3 Adaptive pattern beam scanning STED microscopy

3.1 Beam scanning and RESOLFT microscopy

The adaptive PSF generation for the STED beam, as described in the last chapter, makes it possible to apply various high quality depletion patterns without the need to alter the setup. This adaptive element increases the flexibility of the microscope.

In the following chapter, a new adaptive scan-pattern approach is introduced. This concept is tailored to STED microscopy and requires the local adjustability of the microscope resolution to provide a major increase in image acquisition speed. This adaptive pattern benefits from a scanner with low inertia. Hence, it is combined with a novel galvanometer beam-scanning concept for STED microscopy.

In the following the implementation of the beam scanner into a STED microscope will be described. The applicability will be demonstrated on technical and biological samples. Thereafter the adaptive scan pattern approach will be presented. The unrivaled image acquisition speed due to the combination of both concepts is confirmed by imaging technical and biological samples. It will be shown that besides the acquisition speed the concept provides a superior SN ratio and FOV size compared to other scanning approaches. Additionally, the light dose applied to the imaged sample is reduced, which is another characteristic no other scanner offers today.

Today's RESOLFT microscopy

The major aim of diffraction unlimited microscopy, such as RESOLFT microscopy, is the combination of high resolution with the benefits of far-field optical microscopy, as mentioned in chapter 1. Such instruments are great tools for analyzing dynamic protein interactions and 3D structures inside the living cell.

In the past years the resolution of RESOLFT microscopes continuously improved [73][77] and even isotropic resolution below 50nm became feasible [44]. Since in theory the resolution is unlimited more stable dyes and lasers with higher power will enable even higher resolutions. Only recently the use of crystal color centers enabled resolutions down to 6nm in the focal plane [79].

Despite those improvements in resolution, most of the used STED microscopes utilize piezo stage scanners [60, 73, 79–81]. A STED microscope, which applies a stage scanner, is simpler in design. This convenience mainly results from fewer components needed compared to other designs. Fewer components lead to a more reliable system as fewer sources of possible errors are introduced. Furthermore a higher number of components in an optical setup produce a higher loss of power. This is an unwanted attribute, especially in STED microscopy.

Some major disadvantages of stage scanning are restricted acquisition speed and acceleration of the sample. Both drawbacks limit the field of application of these STED microscopes. The important domains of imaging dynamic processes and 3D structures inside living cells are mostly excluded. Furthermore, the field of view (FOV) of common piezo stage scanners is limited to 30-40 μm [57]. When complete cellular structures are of interest, this restricted FOV correspond to another disadvantage.

Resonant beam scanners in STED microscopy

In confocal microscopy these drawbacks are circumvented by scanning the beam through the sample instead of sweeping the sample through the focal region. Recently, Westphal et al. introduced the first beam scanning STED microscope, which applies a resonant scanning mirror [82]. Resonant scanning is one common approach for video rate scanning speeds. The usability of the concept was firstly demonstrated on a technical sample but was used later to firstly record STED images of dynamic processes inside a living cell in a FOV of 1.8 μm x 2.5 μm with an effective dT of around 7 μs [36]. Newer revisions produce astonishing images of living cells [34, 35].

Despite its high physical scanning speed, the concept has several disadvantages. First of all Westphal et al. uses a resonant mirror only for beam scanning of one axis. The orthogonal axis is still controlled by a piezo stage. Second, different dTs can only be achieved by summing up multiple detection cycles. Sample movement and dynamics occurring between several line scans can normally not be compensated for. These motion artifacts can lead to deteriorated resolution. Moreover, the commonly sinusoidal trace of the resonant scanner results in non-linear illumination of the specimen and nonlinear pixel registration times, both unwanted aspects. The limitation of the FOV to the nearly linear area of the sine function resolves the problem to some extent as it introduces the additional disadvantage that information is only collected a fraction of the scan time. This inefficient duty cycle results in the resonant mirror performing well below the theoretical limit. Furthermore, the FOV and the dT are linked reciprocal. A larger FOV produces higher scanning speeds. This circumstance results in several handicaps as not only the duty cycle decreases for larger FOVs but also more lines must be detected and summed in a short time to achieve the needed SN. Hence, the available speed of the acquisition unit and the data processing unit

can limit the size of useful FOVs. The same holds for higher resolutions.

A two mirror concept

The inefficient duty cycle of the resonant scanner reduces the actual usable scanning speed for STED images to regions of ordinary galvanometers [83].

Therefore, the usage of regular galvanometers results in comparable scanning speeds but provides more freedom of application, since they can be randomly positioned at the required speed for achieving the desired dT. Furthermore, no piezo stage is needed for 2D imaging. This concept, as applied in confocal microscopes, uses commonly two scanning mirrors for the orthogonal axes of the focal plane. The axial direction is scanned by a single linear piezo actuator at the stage or the objective lens.

Besides the rotation of the beam the rotation of the mirrors introduces a shift of the beam position at the back focal plane of the objective lens. To minimize this shift both mirrors are normally positioned near the conjugated back focal plane. Nonetheless, even a marginal shift results in an asymmetric cut-off of the light beam at the back focal plane. In case of the doughnut STED beam this cut-off will produce an imperfect intensity distribution of the STED depletion profile as the phase profile cannot destructively interfere (see also chapter 2) [47].

Beam shifting at the pupil can be avoided by employing an additional galvanometer [84]. Two of the three mirrors are coupled for one scanning axis. The remaining mirror scans the orthogonal axis. The single mirror is positioned at the conjugated back focal plane, whereas the two mirrors for the remaining axis decouple beam shift and scanning rotation. This concept makes it necessary to position the single mirror unit with high precision. A disadvantage left here is that the distance from the mirror to the back focal plane of the objective lens cannot be changed.

The Quad-scanner and its usage for adaptive pattern scanning

The following section rounds this two mirror concept out by introducing a galvanometer scanner with two mirror unit for each axis resulting in four mirrors for the complete scan unit (Quad-scanner). For the first time this scanner concept is applied to a STED microscope. It provides random scanning and ensures at the same time the beam position in the back focal plane. This optimally positioned beam allows the STED setup to perform with best efficiency. To fix the pupil position with adequate exactness over the complete FOV independent of the mirror position, a calibration of the galvanometer mirror movement is presented in section 3.3. Here also the efficiency of this calibration procedure is demonstrated with direct measurements of the beam position in the back focal plane, PSF measurements and STED imaging of fluorescent beads.

In section 3.4 the fast scanning capability of the system is demonstrated by imaging moving beads on a glycerol surface and by imaging of dynamic processes

inside living cells.

The freedom to move and even jump along any direction in the focal plane enables a new adaptive scanning concept. Common confocal microscopes provide the possibility to rotate the FOV by optical means. Since both scanning axes can be moved independently, this feature is also demonstrated for the STED microscope in this section. The rotation provides the possibility to use a rectangular FOV with higher efficiency because the object of interest can be rotated to fit best into the smallest possible FOV. Propelled by the idea to reduce the FOV to regions with information the STED microscope provides even greater advantages. Since the resolution of the STED microscope can be tuned by the STED laser intensity a pre-scan can be performed with confocal resolution, which locates the fluorophores inside the FOV. The actual STED scan with high resolution is then adaptively restricted to this pre-localization mask. Hereby, an image acquisition speed improvement of a factor of 13 and a factor of 8 will be demonstrated at fluorospheres and densely labeled biological samples, respectively. The adaptive scan pattern can increase the overall effective scanning speed of the normal galvanometer scanner over the effective speed achieved by the resonant scanner by else better SN ratio and less applied light dose. Combined with the large FOV available the adaptive Quad-scanner opens up new possibilities for STED microscopy in living cell applications.

The last part of the chapter will conclude the presented concept.

3.2 Experimental implementation of the beam scanning concept

Experimental setup

The starting point of the beam scanning implementation for STED microscopy was a common STED setup similar to the one presented by Harke et al. [Ben]. It is shown in fig. 3.1. Since many other STED setups that have been presented so far, the used microscope inherits the two basic laser beams for excitation and depletion of the fluorophores. For excitation a triggered laser diode (LDH-P-635, Picoquant, Germany) emitted pulsed laser light of approximately 80ps pulses at a repetition rate of 80MHz and a wavelength of 635nm. The excitation light was spatially filtered by a 50 μm pinhole to guarantee a TEM_{00} mode. The STED beam was generated by a Ti:Sa solid state laser (MaiTai, Spectra Physics, USA). The system produced ultra short laser pulses of 100fs at a repetition rate of 80MHz. For all measurements presented here, the wavelength was tuned to 755nm. The pulses were pre-stretched by a 50cm SF6 glass rod and then coupled into 100m of polarization-maintaining single mode optical fiber (PMF) (AMS, Germany). Nonlinear self-phase-modulation and regular dispersion resulted in

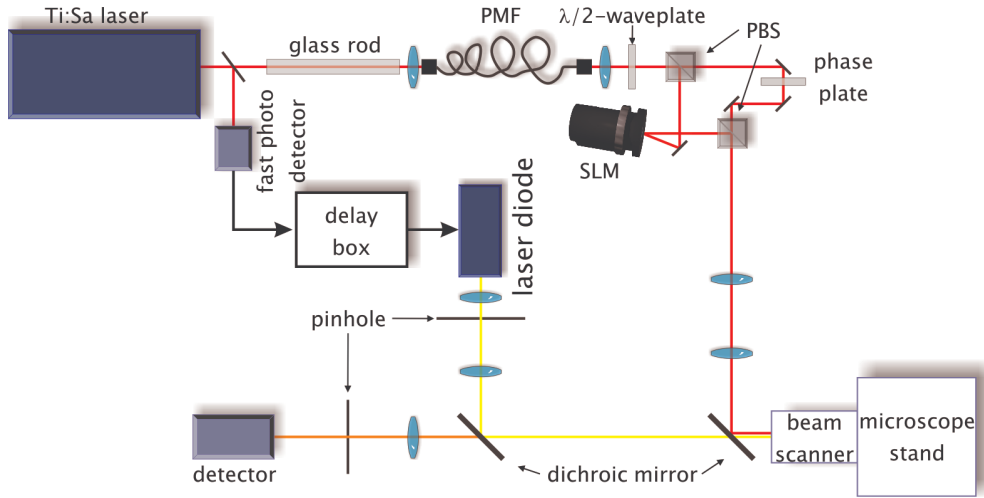


Figure 3.1: A schematic drawing of the STED setup. A Ti:Sa laser was used to generate the STED beam. The beam pulse was stretched by a glass rod and a PMT fiber before a phase modulation was imprinted by a SLM or a vortex phase plate. The beam was superimposed with the excitation light of a diode laser via dichroic mirrors and coupled into the beam scanner. The beam scanner was positioned in front of a commercially available microscope stand. The fluorescence photons were detected by an APD positioned behind a confocal pinhole.

pulses of approximately 200ps. After the fiber the STED beam was expanded. A $\lambda/2$ wave plate and a polarizing beam splitter (both B. Halle, Germany) were used to adjust the intensity ratio between the beam reflecting on the SLM (Hamamatsu, Japan or BNS, USA) and the one passing a vortex phase plate (RPC Photonics, USA). This phase plate was used to generate a doughnut-shaped intensity pattern without the need to operate the SLM. Furthermore, this arrangement offers the possibilities to use both components simultaneously or only the SLM.

Both beams were superimposed using dichroic filters (AHF, Germany). The trains of pulses from both lasers were synchronized by an ultra fast photo detector and a custom built electronic delay box, that supplied the trigger signal for the excitation laser with a transistor-transistor logic (TTL) signal.

After the dichroic filters, the beam was coupled into the beam scanning unit with four galvanometers (6210H, Cambridge Technology, USA). The scanner was attached to a commercially available microscope stand (DM IRBE, Leica Microsystems, Germany). After the scan lens and the tube lens, the linearly polarized illumination passed a quarter wave plate (B. Halle, Germany) and was coupled into an oil-immersion objective lens (100x NA 1.4 HCX PL APO CS, Leica Microsystems, Germany).

The detection was performed with an APD (SPCM-AQR-13-FC, Perkin Elmer,

USA) or a PMT (H722P-40, Hamamatsu, Japan), which both were positioned behind a confocal pinhole.

The beam scanner was controlled by a field programmable gate array (FPGA) (NI-PCI-7833R, National Instruments, USA). A customized hardware board provided the signal input and output (IO) of the FPGA.

Beam scanner control

Typically, the image registration speed is much higher for a beam scanning microscope than for a stage scanning system. Therefore, the coordinates must be provided faster to the mirror controller in order to actually benefit from the possible scanning speed. Common personal computers (PC) used for data processing and storing are not real-time capable. This means, that small dTs in orders below ms can not be guaranteed by an ordinary operating system nonetheless how fast the central processing unit (CPU) of the PC clocks.

Additional circuit hardware boards with fixed functionality fulfill the major application tasks of a typical scanning device. Nonetheless, for highest flexibility (see chapter 4) and to establish the required calibration (see section 3.3) a hardware board based on a field programmable gate array (FPGA) was chosen. A FPGA can be freely programmed, therefore providing a fully adjustable real-time data acquisition and processing solution [85]. For the data presented in this chapter, the FPGA provided the function of actually moving the mirrors to their designated position. It simultaneously counted the photons over the desired pixel scan time and transferred the image information to the host computer. Moreover, several minor control tasks such as beam blanking and shutter usage were covered. FPGAs provide a highly parallel architecture; hereby the different tasks did not hinder each other.

The FPGA operated at 80MHz for the internal logic and the digital IOs (DIO). The analog inputs (AI) were sampled at only 200kHz. However, they were not used for any data presented. The analog output (AO) was updated with 1MHz which limited the smallest possible dT to 1 μ s. For fast data transfer between host and FPGA, the board provided three direct memory access (DMA) channels. The whole logic for the FPGA as well as the scanning software was written in Labview 8.5 (see appendix A).

Since miscellaneous hardware components were controlled by the FPGA an additional IO board was needed. Therefore, a customized circuit board was designed. It provided eight operation amplifiers (OP) (Analog devices, USA) circuits to amplify signal voltages from the FPGA to the scanner controller and back. Photon counting was done via a DIO line directly from the APD. At the PMT a trans-impedance amplifier was used to generate the signal voltage for digitization. Five analog amplifiers were implemented for further actuator control. Lastly, several DIOs interfaces were provided for shutter and TTL control (see section 4.3). The actual layout is presented in appendix A.

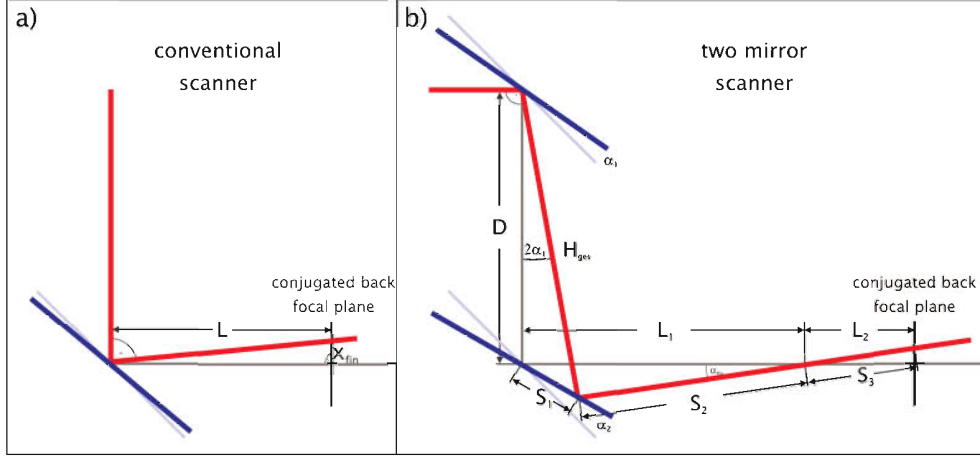


Figure 3.2: The figure presents the two scanning concepts. a) The rotation of a single mirror (blue line) produces besides the rotation also a shift of the beam (red line). b) An additional second mirror introduces the freedom to rotate and position the beam depending on the rotation ratio of the two mirrors freely in space.

3.3 Decoupling beam shift and mirror rotation

The Quad-scanner concept

The last section described the hardware used for the presented STED measurements in this chapter. This section covers the novel beam scanner used in more detail. It presents the necessary steps taken to calibrate the system and validates the beam position in the back focal plane and the STED performance over the complete FOV.

As mentioned, a simple beam scanner design of one mirror per orthogonal scanner axis positioned near the conjugated back focal plane holds drawbacks. This design does not only rotate the laser beams and scan the focal spot, but also shifts the beam in the back focal plane position (fig. 3.2a and fig. 3.4a). For a confocal microscope this concept brings about minor disadvantages.

In contrast, for STED microscopy these minor disadvantages result in major performance impairments through the asymmetric beam and phase pattern cutoff.

The STED beam must not move in the pupil plane during scanning because this would fill up the central zero in the doughnut shaped PSF in the focus. This precondition is achieved by the Quad-scanner. The ratio to fix the beam position in the conjugated back focal plane can be deduced from (see fig 3.2b):

$$\begin{aligned}
\frac{x_{fin}}{\sin(\alpha_{fin})} &= \frac{L_2}{\sin(90^\circ - \alpha_{fin})} \\
\frac{S_1}{\sin(\alpha_{fin})} &= \frac{L_1}{\sin(135^\circ + \alpha_2 - \alpha_{fin})} \\
\frac{S_1}{\sin(2\alpha_1)} &= \frac{D}{\sin(45^\circ - 2\alpha_1 + \alpha_2)}.
\end{aligned} \tag{3.1}$$

These can be transformed by the use of

$$L_2 = L - L_1 \tag{3.2}$$

to

$$x_{fin} = L \tan \alpha_{fin} - D \frac{\sin 2\alpha_1}{\cos \alpha_{fin}}. \tag{3.3}$$

For $L=D$ and $x_{fin} \equiv 0$ this equation results in a simple equation for the rotation ratio of the two mirrors:

$$2\alpha_1 = \alpha_2. \tag{3.4}$$

The implantation of this two mirror scanning unit into each of the classical two-mirror scanner results into the QuadScanner. This technique decouples mirror rotation and beam shift for both scanning axes. The pupil can also axially be freely positioned and the ratio of each mirror couple is adjusted so that the point of rotation reclines on the pupil plane of the system.

To provide an alignment near the theoretical $L = D$ the mirrors must be positioned in a way, that the conjugated back focal plane is located between both scanner units. In contrast to the three mirror concept [84] the galvanometers no longer need to be precisely positioned at a certain location. A calibration of the mirror ratio allows for complete compensation of mounting tolerances.

Galvanometer calibration

To unlink the achieved beam stabilization from mirror positing errors a calibration is necessary. Unfortunately, the beam position errors in the back focal plane cannot be detected and compensated during the scan with the applied setup. Instead, a procedure must be applied for calibrating the point of rotation for the complete FOV.

To measure the beam shift for the calibration routine a four quadrant diode (4-QD) (S6695-01, Hamamatsu, Japan) was placed in the pupil plane. This device

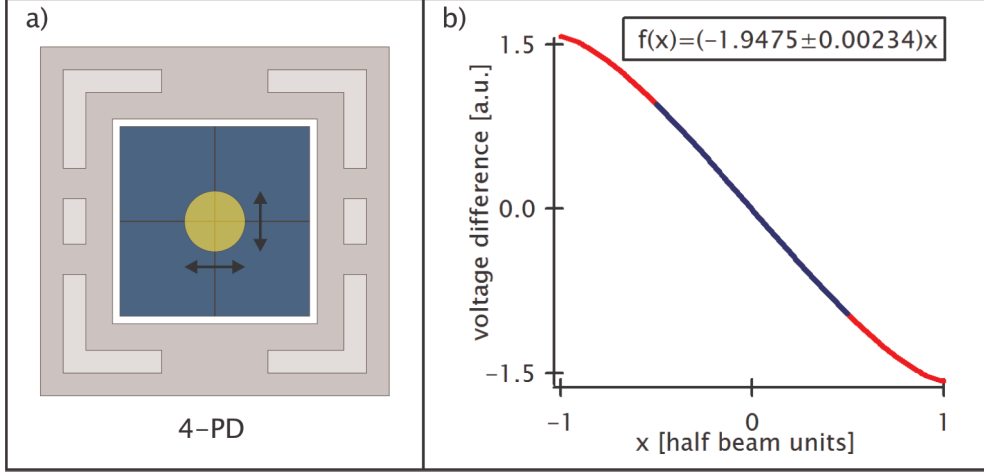


Figure 3.3: The figure demonstrates schematically the position measurement with a 4-QD. The 4-QD is illuminated by a circular beam spot (a). The movement of the illumination spot away from the center generates a voltage difference (b). In the central region the function between movement and voltage difference is nearly linear (blue line in b).

incorporates four photo diodes of identical size that form a connected detection surface (see fig. 3.3a).

The voltage of the four diodes can be used to localize the center of a circular beam falling on all four diodes, as long as the beam does not cover the whole detection surface. A displacement Δx_1 of the beam away from the center leads to a signal, which can be described by (see fig. 3.3b):

$$voltage_{Diff} = -x_1 \sqrt{1 - x_1^2} - \arcsin x_1. \quad (3.5)$$

For small misalignments of the beam, the voltage feedback of the 4-QD can be approximated by a linear function (see fig 3.3b blue line). This linearity holds also true for the beam shift, if one of the two mirrors of each unit rotates by only a small angle. Therefore, any rotation misalignment generates mainly a linear response on the 4-QD (see fig. 3.4b).

In conclusion, the calibration routine corrects this linear factor from the theoretical derived mirror rotation ratio of two to a factor with minimal beam shift. Alone this calibration step produces nearly perfect positioning of the point of rotation in the back focal plane (see fig. 3.4c).

In our setup the linear calibration reduces the induced beam shift to around $20 \mu\text{m}$ in total.

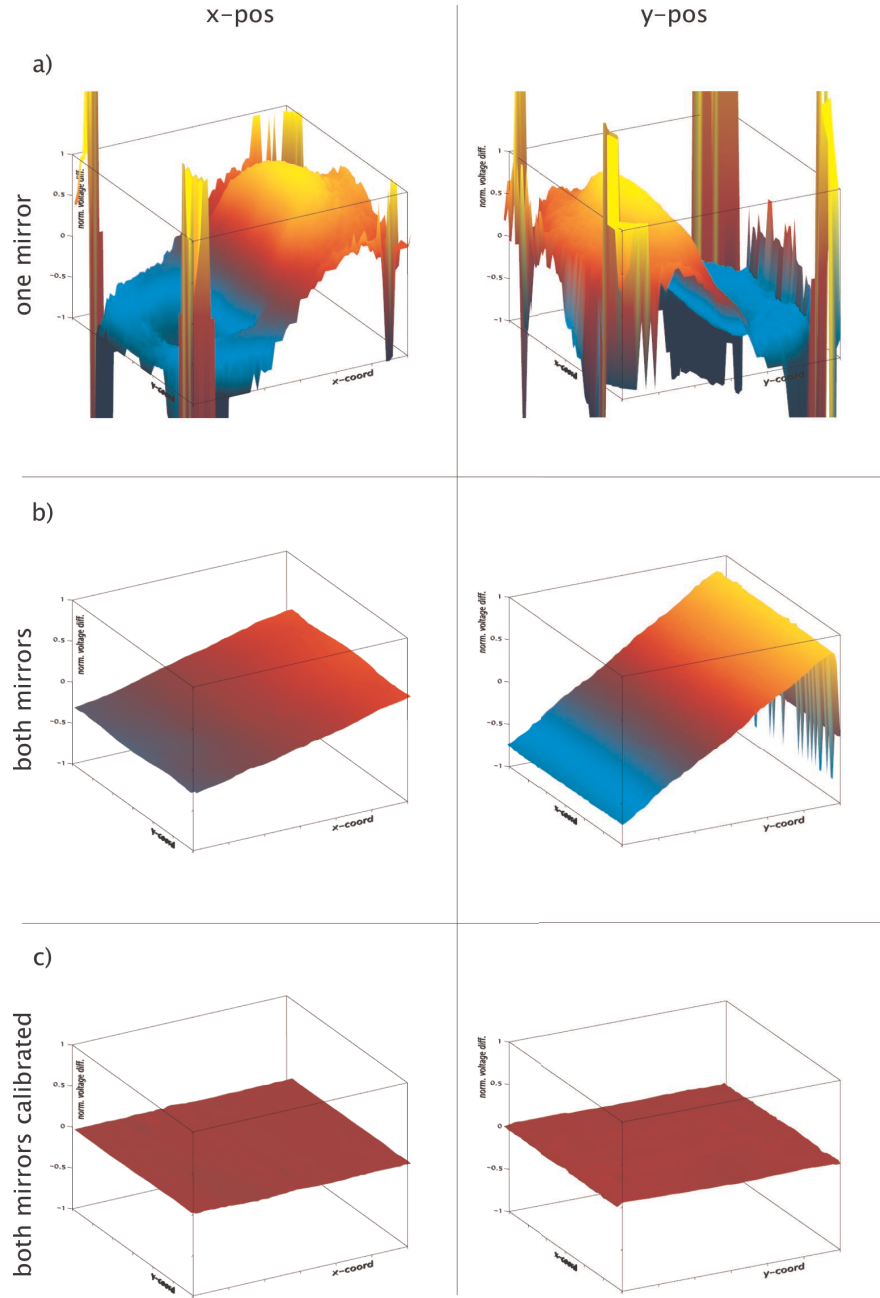


Figure 3.4: The figure shows the normalized 4-QD voltage difference for a FOV of $60\mu\text{m} \times 60\mu\text{m}$ for three different position concepts. For small differences the figure represents directly the beam position difference to the optical axis. With one mirror per scan axis the beam is shifted even for small angles to positions outside the active 4-QD area corresponding to a shift of more than 1mm (a). After both mirrors are used with the theoretically derived rotation ratio the shift is reduced to a linear function of the scanning angle (b). The calibration of this linear factor results in a central beam positioning in the back focal plane for the complete FOV. The remaining variance is below $\pm 1\%$ absolute, corresponding to position errors below $10\mu\text{m}$.

Experimental validation of the calibrated QuadScanner at STED measurements

The measured beam shift provides the data of the beam position in the back focal plane. The actual more important information of the resulting STED performance is not covered through such measurements. Instead the achieved STED performance must be validated for the different modalities. As is the case for the SLM calibration presented in chapter 2, this was done by verifying the actual depletion PSF and STED performance at each point of the FOV.

Like before, the PSF is validated by measuring the scattering of the illumination at 80nm gold beads (see appendix A. Fig. 3.5 illustrates the influence of the calibration on the STED PSF in different areas of the FOV. The first two columns represent scans with increasing scanning angle (left to right). The last column shows a detailed line profile along the axis with the most asymmetric intensity distribution of the PSF of the second column. The rows cover the different concepts of beam position stabilization. As can be seen, the disabling of one mirror in each unit resulted in slight disadvantage in the middle of the FOV. However, in outer regions the STED doughnut was completely destroyed (fig. 3.5a).

The application of the Quad-scanner resulted even non-calibrated in a greatly enhanced STED PSF in areas with increased scanning angles (see fig. 3.5b).

Finally, the linearly calibrated galvanometer ratios showed a clear improvement over the theoretical ratio in form of a more symmetric intensity distribution and a minor enhanced minimum in the outer regions of the FOV (see fig. 3.5c).

The final STED performance check for the galvanometer calibration was performed with a sample containing fluorescent beads. Like mentioned in chapter 2, the usage of fluorospheres is much more precise than the usage of single molecules. Again a sample of Crimson beads was used to experimentally verify the performance difference of each scanning concept. The bead sample was prepared as mentioned before (see appendix A). The excitation power was set to around $50\text{kW}/\text{cm}^2$ whereas the STED intensity was limited to around $270\text{MW}/\text{cm}^2$. For all images, the dT was adjusted to $50\text{ }\mu\text{s}$. The pixel size was set to 20nm . Fig. 3.6 shows the different STED performances. The rows and columns of the figure are organized as in fig. 3.5. Each row presents a different degree of beam position correction. The first two columns present ROIs with increasing distance from the optical axis. The last column shows a line profile along the marked position indicated in the second column. Clearly, the STED microscope is not usable if the beam is not centered when only one mirror per axis is active (see fig. 3.6a). Not only is the resolution of the system corrupted, but no fluorescence can be recorded at all.

In contrast, with the two mirror concept the STED microscope works well even

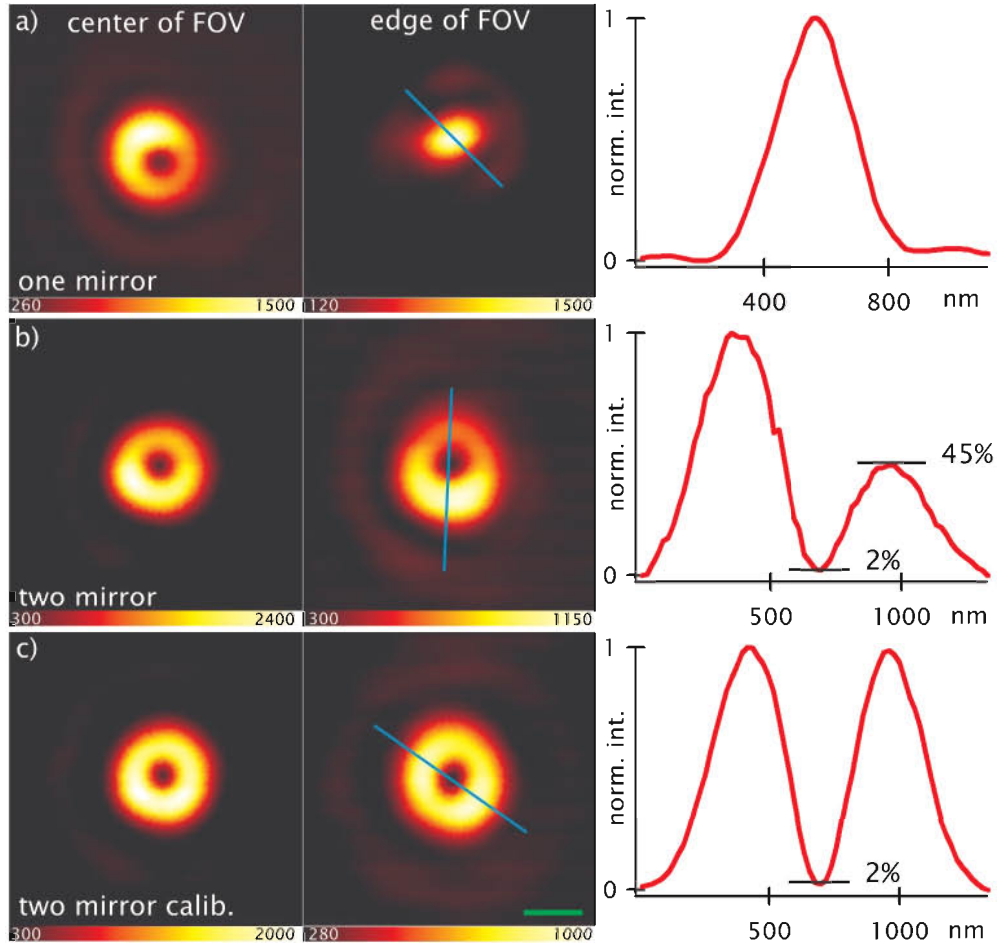


Figure 3.5: The figure illustrates the influence of an introduced beam shift to the intensity distribution in case of a doughnut PSF. Clearly only one mirror per axis is not capable of compensating the beam shift in a sufficient way to guarantee a usable STED doughnut. Instead no doughnut mode is recognizable at the edge of the FOV (upper row). The theoretical mirror ratio performs much better (middle row). However, at the edge of the FOV a asymmetrical intensity distribution is present. Only the error corrected Quadscanner ensures the optimal STED PSF for the complete FOV (lower row).

at the edge of the FOV (see fig. 3.6b). This impressive performance gap can even be increased by the additional application of the linear calibration. The usage of calibrated mirror ratios resulted in a slightly increased fluorescence signal compared to the non-calibrated ratios (see fig. 3.6c). Additionally, the images reveal a perfect symmetric representation of the beads whereas the theoretical ratio scan produces slightly asymmetric bead forms due to the asymmetric intensity distribution of the STED PSF (see fig. 3.5b) and not as high resolutions. The optimal, measured STED resolution performance was around 45nm FWHM in each direction inside the focal plane for the edge of the FOV due to the linear calibrated scan mirror ratios. The same resolution was achieved over the complete FOV.

3.4 Experimental evaluation of the QuadScanner performance

Possible scanning speed with a small ROI

The proposed calibration provides the desired image quality increase of the setup. After the optimal resolution was achieved for the complete FOV of $80\text{ }\mu\text{m} \times 80\text{ }\mu\text{m}$, the speed of the scanner was validated. Therefore a sample of fluorescent beads on a glycerol layer was prepared (see appendix A). Each scan line hold 60 pixels. The pixel size was set to 20nm because of the higher STED resolution. The STED intensity setting was the same as for fig. 3.6. The excitation was set to $100\text{ kW}/\text{cm}^2$. This value was empirically validated to be the optimal setting regarding photo bleaching and signal strength. The PMT was used for detection since the dead time of the APD was too long to count enough photons during the very short dTs. Fig. 3.7 shows every second images out of a time series. The first two images were recorded in confocal mode whereas all other images display the STED measurements. Clearly the resolution is greatly increased with STED. Analysis of the images revealed comparable resolution to fixed sample measurements with much longer dTs. The smallest reasonable dT was $4\text{ }\mu\text{s}$. Smaller dTs resulted in a not acceptable SN ratio but could still be performed by the scanner unit. An application of a detection unit consisting out of more than one APD should result in even better performance of the setup [82].

The mentioned dT of $4\text{ }\mu\text{s}$ doesn't represent the effective dT. Instead, additional pixels must be inserted for QuadScanner acceleration changes (see appendix A. The error free images resulted in 26 of such interpolation pixels needed for the $1.2\text{ }\mu\text{m}$ line width and a dT of $4\text{ }\mu\text{s}$. Thus, the effective dT was increased to approximate $5.8\text{ }\mu\text{s}$, which is around ten times faster than for common piezo stage scanner approaches [60].

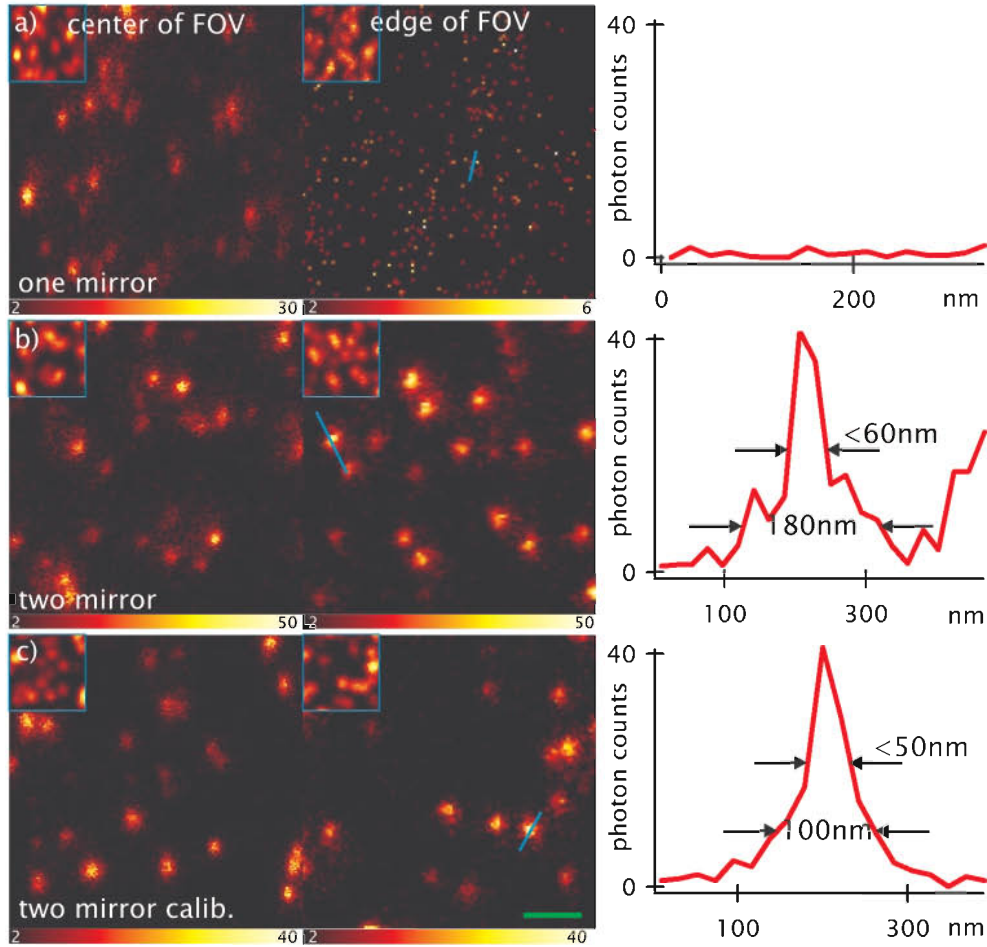


Figure 3.6: The QuadScanner enables STED measurements for the complete FOV. With one mirror per axis the introduced beam shift did not allow STED measurements in the edges of the FOV (upper row). The QuadScanner with theoretical mirror ratio is capable to perform STED measurements for the complete FOV (middle row) but only with error corrected ratios the performance worked optimal for the complete FOV. The size of the remaining stand in case of the non-calibrated QuadScanner was reduced. For the applied STED intensity the impressive resolution below 50nm demonstrated the theoretical performance of the proposed setup. The scale bar corresponds to 400nm.

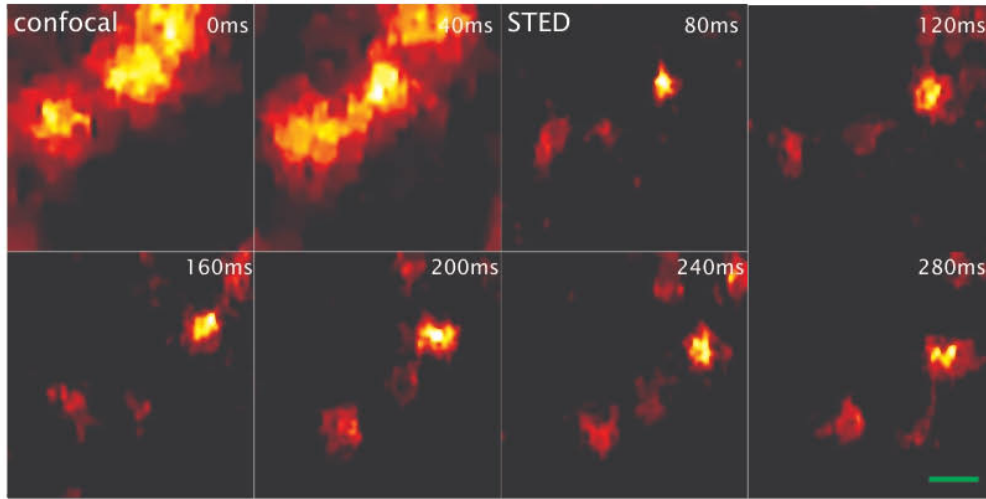


Figure 3.7: The figure presents some images picked from a series of 500 images. The first two images were recorded in confocal modus. The remaining images are recorded in STED modus. Clearly the higher spatial information is visible in STED modus. The dT was set to 4 s corresponding to around 50 frames/s. The scale bar represents 200nm. All images were filtered by anisotropic diffusion.

Living cell application with largest ever presented FOV in STED microscopy

To further validate the performance of the Quadscanner at a biologically relevant sample the amino precursor protein (APP) immunostained with Atto 633 was imaged inside N2A cells. The APP is located in the dendritic and axonal compartment of neurons [86]. It is essential for the normal synaptic function and processing, which strongly depends on the intra neuronal localization. APP plays a major role in the etiopathology of Alzheimers Disease (AD). AD is one of the most common disease of elderly people. Since the pathway of the APP is not known for sure a direct imaging of the protein movement inside living cells is of great interest. To provide a better environment for the living cells the objective lens was heated to 37°C. The excitation power and STED power were set to only 50kW/cm² and 150MW/cm², respectively to reduce photo bleaching of the dye. The dT was set to 15 μ s. The number of pixels per line was fixed to 328. Fig. 3.8 shows impressively the higher spatial information gained by STED. The higher number of pixels per line and the good image quality provided by the Quad-scanner enhanced the effective dT to only 16 μ s.

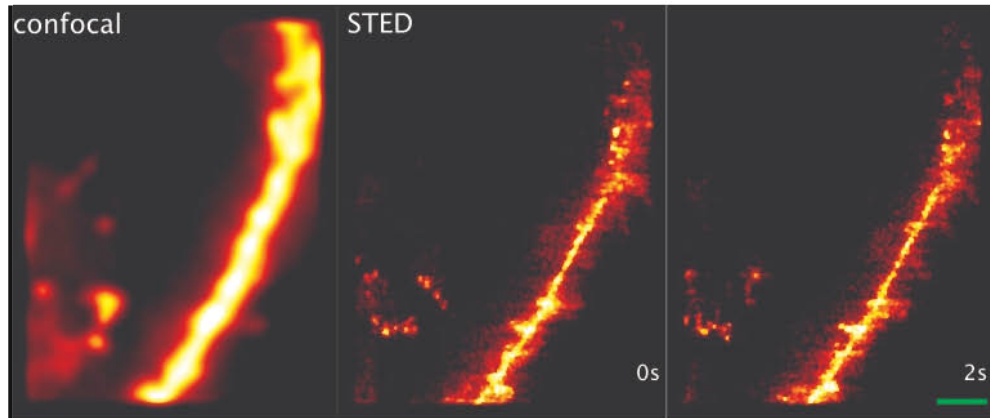


Figure 3.8: The figure presents a time series of fluorescent images recorded with the Quad-scanner. The sample consists out N2A cells in which APP was immunostained with Atto 633. The membrane on the right side of each image is represented in a non-optimal quality as STED increases only the resolution in the focal plane. Nonetheless STED reveals the APP distribution inside the focal plane (right side of each image). The confocal resolution is not high enough to provide similar spatial information. The bar represents 1 μm . All images were linearly deconvolved.

3.5 Adaptive scanning pattern in STED microscopy

The galvanometer provides the possibility to beam-scan both axes inside the focal plane and to control the speed and position of the beam. Both attributes contribute to a novel imaging technique which increases the image acquisition time for STED images according to the information present inside the ROI.

Rotation of the ROI

The advantage of the galvanometer scanner to beam-scan each axis inside the focal plane can be used to rotate the ROI. The usage of both scan axis in combination with a simple affine transformation in homogenous coordinates [87] provides the possibility to place the ROI according to the specimen orientation. Thereby, the size of the ROI can be reduced which decreases the required image acquisition time accordingly.

Fig. 3.9 demonstrates the rotation capability of the scanner at the example of fluorescent beads. Again a sample of Crimson beads was prepared (see appendix A). All settings were the same as for fig. 3.6, except the dT was adjusted to 20 ps. Through the demonstrated rotation a reduction of scan time was achieved as the ROI could be reduced from 250x250 pixels to 250x98 pixels. This improvement

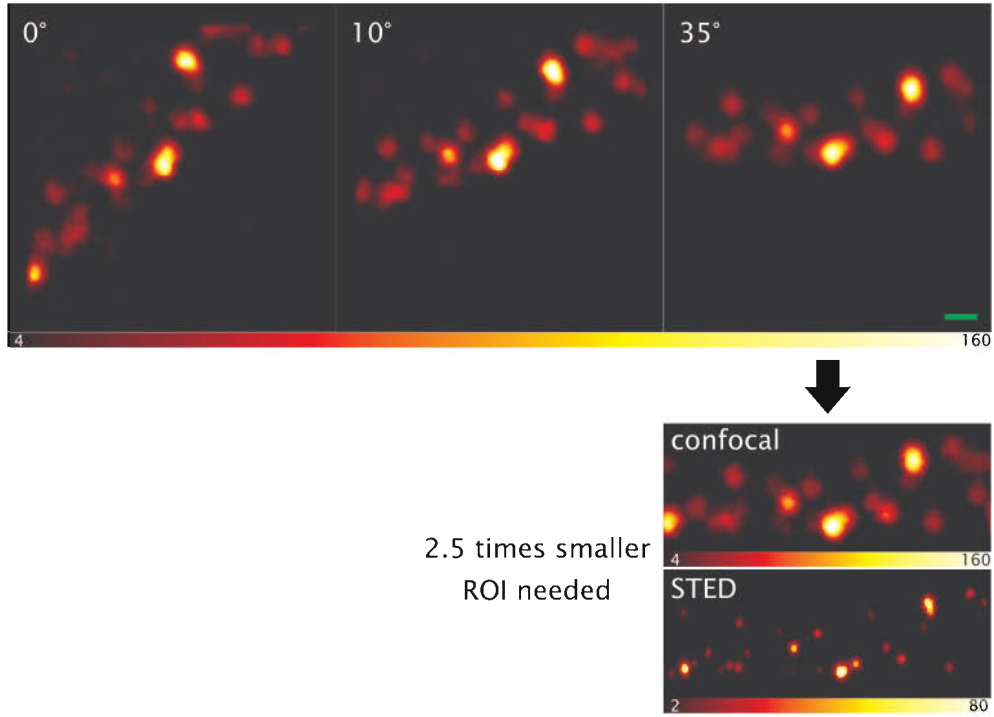


Figure 3.9: The figure shows the hardware rotation capability of the scanner. No disadvantages are generated by to this feature. Instead, a factor of 2.5 in effective scan speed improvement can be achieved by a more ideal ROI. The scale bar represents 500nm. All images were linearly deconvolved.

by a factor of 2.5 results in an effective dT of 8 s compared to the non-rotated ROI. However the information of the specimen represents a scan of 20 μ s dT and therefore provides a much better SN ratio.

Adaptive pattern scanning

The efficient use of the ROI through its rotation gives rise to the idea to scan only areas with information. The small inertia of the galvanometer scanner allows fast random positioning and can be used to efficiently scan only areas containing information in them.

The general idea is to use a pre-scan to locate the areas of interest. All subsequent scans then ignore image areas found to be empty. These areas can be located anywhere inside the FOV and need not be connected. Instead they are scanned by the galvanometer according to a pattern representing the fluorophore distribution.

Since the location of the fluorophores inside the sample is unknown before the first scan at least one scan must be performed to gain image acquisition speed for further scans thorough the knowledge of the fluorophore distribution. Hence, confocal microscopes only gain imaging speed starting with the second scan of

a series. Yet, for the main application of observing dynamic processes the scan pattern generated from the first scan would be useless for the second scan as the dynamic information is unknown.

In contrast to the confocal microscopy the RESOLFT microscopes can profit from a scan pattern even for the first scan. This fact is due to the unique feature of most RESOLFT microscopes to tune the resolution. In STED microscopy the applied depletion intensity controls the achieved resolution (see section 1.3). As a result, the introduced STED microscope can scan with confocal resolution and with an about 5 times higher resolution. The image acquisition with the higher resolution would need 25 times more pixels and therefore a 25 times longer acquisition time than the confocal scan for 2D images. Hence, a confocal pre-scan can provide the fluorophores distribution in a 25 times shorter time than the first STED scan by else identical dT. By applying the scan pattern gained from a segmentation of the confocal pre-scan the actual STED scan could be performed much faster. Actually, the STED scan increases the spatial information of the sample only at positions holding fluorescent information (see fig. 3.10).

The theoretical limit for image acquisition speed gain $gain_{aS}$ is strongly depending on the fluorophore density and distribution. It reaches its maximum in case of a single object of interest inside the ROI, which is smaller than around half of the confocal resolution. Assuming a sampling according to Nyquist, it can be described by

$$gain_{aS} = \frac{width_{ROI} \cdot height_{ROI} \cdot x_{conf} y_{conf}}{width_{ROI} \cdot height_{ROI} \cdot x_{conf} y_{conf} + (x_{conf} y_{conf})^2} \quad (3.6)$$

where $width_{ROI}$, $height_{ROI}$ are the width and the height of the ROI. x_{conf} , y_{conf} , x_{STED} and y_{STED} represent the pixel sizes in x and y for the confocal pre-scan and the STED scan, respectively.

Validation of the adaptive pattern scanning

This adaptive scanning pattern method was implemented in the scanning software. The so-called coarse and fine scan indicates the confocal and the STED scan modus. The needed partitioning of the coarse image into a binary representation was provided by the use of a threshold. Pixel shifts introduced by different scanning speeds were compensated (see appendix A).

To validate the functionality and to demonstrate the maximum improvement according to the adaptive scan pattern in combination with the Quad-scanner a sample of sparsely distributed Crimson fluorospheres was prepared (see appendix A). Fig. 3.10 presents the images acquired in confocal and in adaptive STED mode of a region of 20 μm x 20 μm . The illumination settings and the pixel size were set as in fig. 3.6. Both images represent the same fluorophore distribution. No essential information was missed due to the adaptive pattern scanning. In-

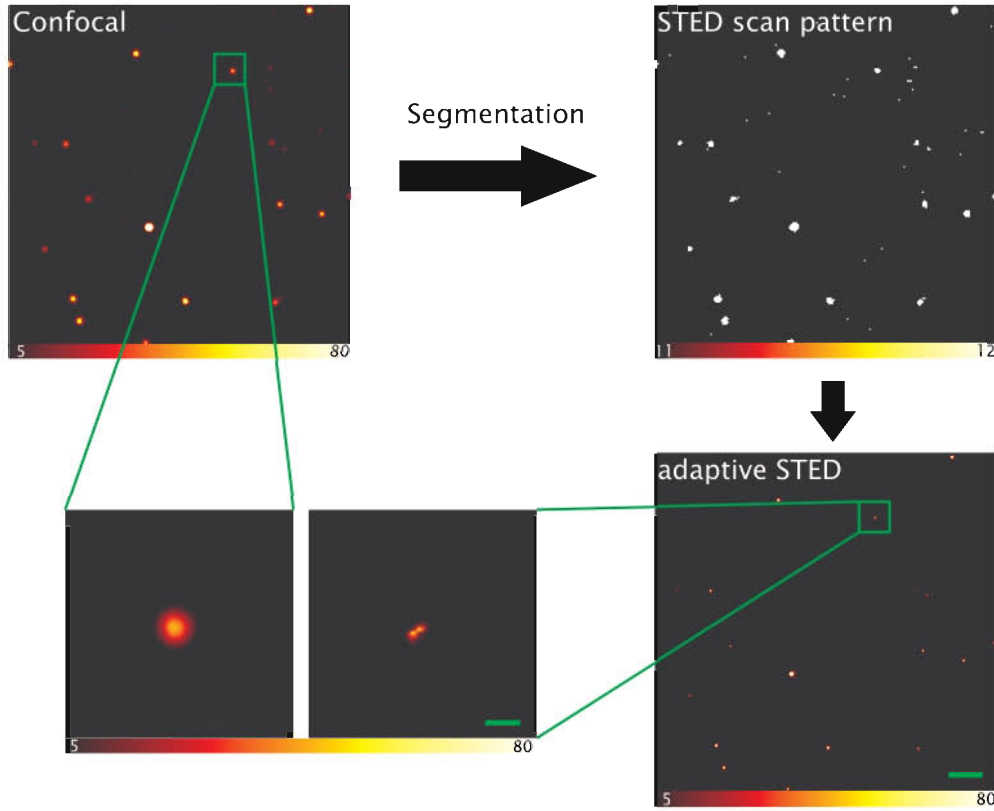


Figure 3.10: A factor 13 higher scanning speed is demonstrated. The figure shows Crimson fluorophores scanned confocally and with an adaptive scan pattern for the STED image. The segmented confocal image provides the adaptive scan pattern for the STED scan. The actual STED scan is only performed at positioned shown in white in the STED scan pattern image. Nonetheless, no information is lost but the increased resolution through STED reveals the fluorospheres distribution in more detail. The scale bars represent 2 μm for the large images and 400nm for the close-ups. All images were linearly deconvolved.

stead the STED image supplies the typical resolution of around 45nm, like in an ordinary STED scan. In contrast the adaptively scanned image was scanned 13 times faster, resulting in an effective dT of only 3.9 μs . The scan provides the same SN as a scan taken with 13 times longer dT. A reduction of the dT from 50 μs down to possible feasible 20 μs would even result in an effective dT of 1.6 μs . This speed would represent the fast ever reported STED scanning speed.

This important result has to be confirmed with measurements of biologically relevant samples to become interesting. As the main field of application for a far-field microscope is cell biology, an additional experiment was performed with primary human fibroblasts. Here, the focal adhesion protein Paxilin has

been immunostained with Atto 647N (see appendix A). The change of the focal adhesion distribution in combination with aging is of interest for biology.

These biological samples demonstrate the advantage of the adaptive beam scanner for STED microscopy compared to other scanning concepts. Typical primary human cells have sizes of several $100\text{ }\mu\text{m}$. Adhesions of interest can have sizes up to several $10\text{ }\mu\text{m}$. The usage of scanners with smaller FOVs than the Quad-scanner, like typical used piezo stage scanner, would result in the need to image several FOVs and to reposition the sample between each image acquisition. This would result in longer scan times and a later image registration per software. Even without repositioning the typical image acquisition time for a $30\text{ }\mu\text{m} \times 30\text{ }\mu\text{m}$ ROI would be around 2.5min for 20nm pixel sizes.

In contrast the typical dT of a resonant mirror scanner would be only around 40ns due to the large FOV and the constant line speed. The short dT would lead to problems with today's detection devices because even the best APDs have typical dead times in the same range leading to less usable photons. Moreover, more lines must be summed as each line holds lesser photons. This trend results in a worse duty cycle. The adaptive beam scanner has none of these disadvantages. Fig. 3.11 and fig. 3.12 impressively demonstrates the unique scanner properties. The ROIs were $15\text{ }\mu\text{m} \times 34\text{ }\mu\text{m}$ for fig. 3.11 and $40\text{ }\mu\text{m} \times 40\text{ }\mu\text{m}$ for fig. 3.12. For both scans the STED scan reveals much more structural information of the focal adhesion distribution than the confocal scan. The adaptive scan for the images in fig. 3.11 took around 28s and for the images in fig. 3.12 around 27s with an adjusted dT of $100\text{ }\mu\text{s}$ and $50\text{ }\mu\text{s}$ respectively. These values demonstrate an effective dT of $20\text{ }\mu\text{s}$ or a improvement of factor 5 in the case of fig. 3.11 and a factor of 8 or an effective dT of $6.7\text{ }\mu\text{s}$ in case of fig. 3.12.

Hence, the effective dT of fig. 3.12 is the fastest reported scan time for a STED image of a biological sample ever.

3.6 Conclusions and limitations of adaptive pattern beam scanning

The usage of stage scanner in far-field microscopy results in long scan times and induced errors during the observation of dynamic processes inside living cells. Both drawbacks prohibit the application of such scanner concepts for the observation of fast dynamic processes inside life cells and reasonable image acquisition times of large 3D structures. Nevertheless, these image modalities are the major fields of applications for the optical far-field microscopy. The solution in form of a beam scanner already applied to common confocal microscopes can be transferred to STED microscopy.

The published resonant beam scanner represents the first beam scanner imple-

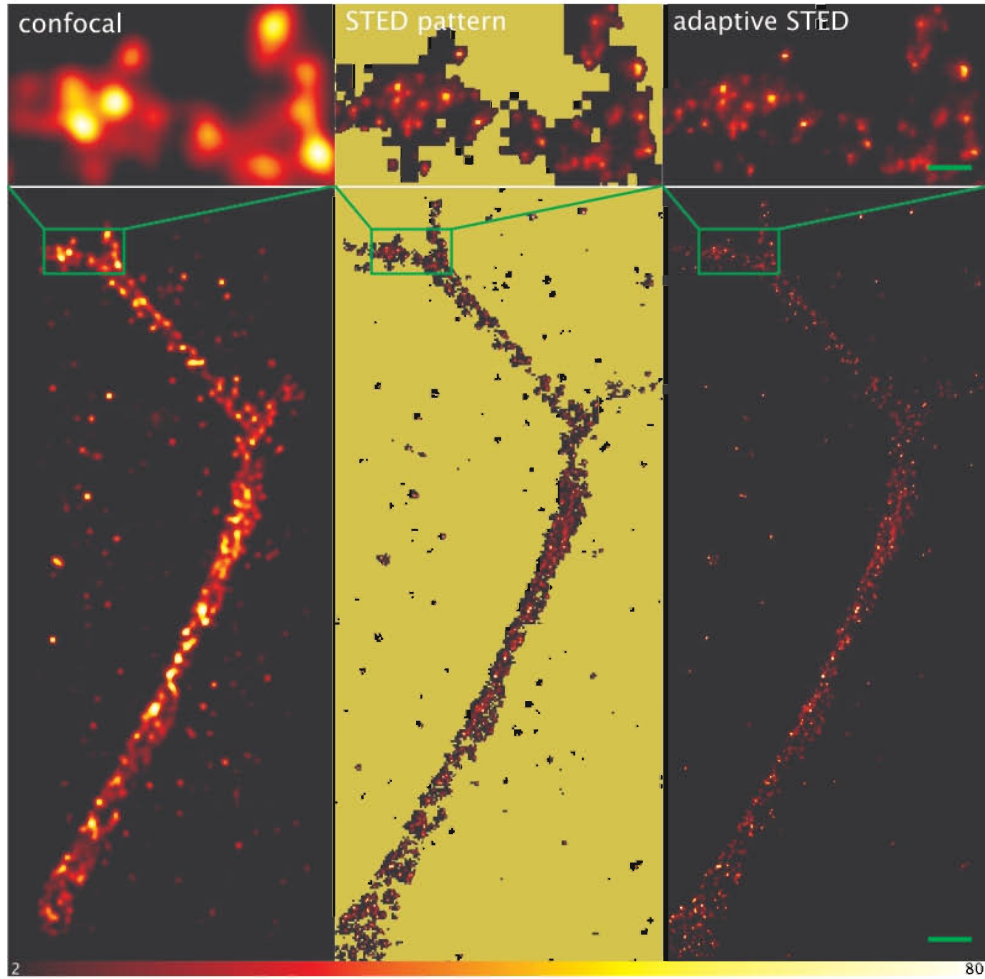


Figure 3.11: The figure shows a focal adhesion of a primary human fibroblast. The protein Paxilin has been immunostained with Atto 647N. The left image represents the confocal scan. The middle image reveals the actual scanned pixel area by a color mask. Finally, the right image shows the adaptive scan in its common representation. As can be seen in the close-up, the STED microscope reveals the single protein distribution whereas the confocal scan does not. The scan time for both images together was around 30s which relates to an effective dT of $20\text{ }\mu\text{s}$ for an ordinary STED scan. This factor 5 times higher acquisition speed compromises the image in no way. The bar in the lower row represents $3\text{ }\mu\text{m}$, the upper bar $1\text{ }\mu\text{m}$. All images were linearly deconvolved.

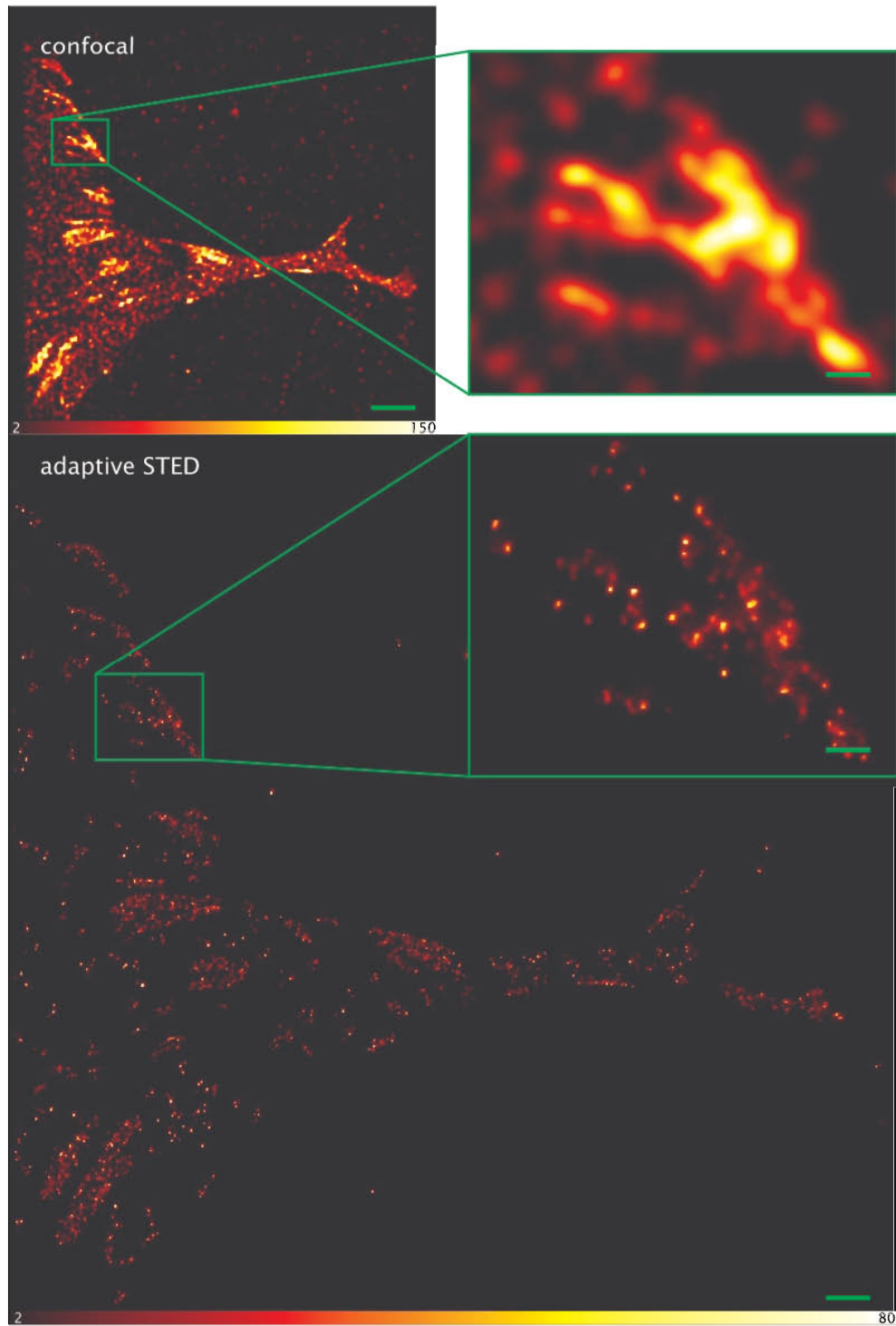


Figure 3.12: The figure shows a focal adhesion of a primary human fibroblast. In detail the protein Paxilin has been immunostained with Atto 647N. The adaptive scan provides exact the same image quality as an ordinary STED scan the same dT but was scanned 8 times faster, which corresponds to an effective dT of 6.7 μs . The scan time for both images together was around 30s. The scale bar represents a distance of 3 μm and 1 μm in the close-up. Both images were linearly deconvolved.

mented in a STED microscope. Besides its high scanning speed, it has several disadvantages such as the small FOV, the additional need for a stage scanner for the orthogonal axis inside the focal plane, a poor duty cycle and the requirement to sum line-scans to accumulate sufficient photons for a decent image quality. Especially the last handicap degrades the image acquisition speed to regions of regular galvanometer mirror scanner.

The presented beam scanning concept in this chapter is the first beam scanner based on regular galvanometers for a STED microscope. To decouple the rotation and the position of the beam complete for both scanning axes a novel four mirror approach was presented. This concept allows a completely free positioning of the scanning mirrors regarding the conjugated back focal plane. It was shown that the mirror rotation ratio of each two mirror scan unit is important for the later beam position precision. For the implementation of the Quadscanner a calibration routine was developed, which corrects the rotation ratio of each axis for the complete FOV with beam position precision better than 20 μm in the back focal plane. The STED setup does not work at its optimal performance until this calibration is carried out. This fact was demonstrated at PSF measurements and imaging of Crimson fluorospheres.

The performance of the presented beam scanner was compared with published data of the resonant scanner by duplicating an experiment of moving fluorospheres on glycerol. Using a regular scan pattern the frame rate of the Quadscanner is lower than that of a resonant scanning system.

However, this slightly handicap is overcompensated by the adaptive scan pattern. This concept uses the unique capability of STED microscopy to tune the resolution by the applied depletion intensity. A confocal pre-scan determines the regions in the FOV with fluorophore information and a successive STED scan refines the spatial information only in these regions. This completely new approach to faster beam scanning was demonstrated at technical and biological relevant samples. Depending on the information inside the FOV an image acquisition speed improvement of factor 13 was demonstrated for the technical sample and a factor of 8 for the biological sample. The latter factor reduced the overall image acquisition time to an effective dT well below the reported effective dT of the resonant scanner, resulting in the fastest reported effective dT for a biological relevant STED image. Besides the impressively enhanced image acquisition speed no drawbacks resulted from the use of the adaptive scan pattern. Instead the image quality was comparable to STED images recorded with 8 times longer dT, thereby implicating a SN ratio, which could not reached otherwise.

4 Adaptive illumination to reduce photo bleaching in STED microscopy

4.1 The reduction of the total number of switching cycles and its benefit

The novel adaptive beam scanning presented in the last chapter reduces the required image acquisition time depending on the information present in the ROI. Fluorophore-free regions are determined by a confocal pre-scan and a STED scan pattern is created according to the segmented information generated from the confocal scan including only those areas holding information. Besides the gain in image acquisition speed, this method illuminates the sample less than an ordinary STED scan with otherwise equal settings. This reduction of illumination time and therefore light dose is only achieved in regions where no fluorophores are present within the focal plane. Nevertheless, because of the cone shape of the beam at high NAs fluorophores located in another sample layer are illuminated. This fact is of special interest not only for live cell imaging where phototoxicity can be detrimental but also for any fluorescence measurements where the sample is prone to photo bleaching and dark state transitions of fluorophores.

The correlation between switching cycles of the fluorophore and photo bleaching

Photo bleaching includes processes, which render a dye completely useless for further fluorescence generation. Dark states characterize dye conditions, in which the fluorescence of the dye is prohibited. Both transitions are usually not desired in fluorescence microscopy.

Each time a fluorophore is excited from the S_0 state to the S_1 state a certain probability exists that the molecule transfers into a triplet state or is even bleached irreversibly before it returns back to the S_0 state. The probability of bleaching the dye or forcing it into a dark state in such a fluorescence cycle depends strongly on the dye itself, the micro environment around the dye and the applied laser powers. A reduction of the total number of excitation cycles reduces photo bleaching and dark state transitions.

This behavior is especially of interest for ensemble switching high resolution concepts using metastable states, as it is the case for STED microscopy (see section 1.3).

During imaging with a STED microscope the excitation beam transfers a high number of dyes in the diffraction limited volume from the S_0 to the S_1 state. The subsequent STED beam depletes most of the excited fluorophores back to the S_0 state. Only fluorophores located at or in close proximity of x_{zero} are given the chance to fluoresce. Clearly fluorophores in the complete diffraction limited volume undergo several switching cycles from S_0 to S_1 and back to S_0 while only the small fraction of fluorophores positioned at x_{zero} contribute to the signal. The high number of switching cycles performed by the fluorophores outside x_{zero} is not related to information but increases photo bleaching and dark state transitions of these dyes. A reduction of the total cycle numbers performed by the fluorophore during image registration will decrease the bleaching.

Unfortunately, the proposed adaptive beam scanning reduces the number of switching cycles only in layer outside the focal plane.

Common ways to reduce photo bleaching and major application fields

A reduction of photo bleaching and dark state transitions will broaden the range of applications of STED microscopy. Especially fields, which call for repetitive scans, such as the tracking of dynamic processes in living cells, will gain most from decreased bleaching. Further important applications will be 3D image acquisition, as each optical section is illuminated several times before it is actually recorded and the expansion of the number of applicable dyes, which are more prone to photo bleaching, such as fluorescent proteins.

Since a reduction of bleaching will be highly attractive for all fluorescence microscope techniques, several approaches to reduce bleaching were studied [59]. The addition of anti-bleaching agents is one of the more prominent approaches to decrease bleaching [58]. Several chemical compounds are known as effective anti bleaching agents. 2-mercaptoethylamin (MEA), which is an effective triplet quencher for fluorophores [88], ascorbic acid and 1,4-diazabicyclo[2,2,2]octane (DABCO) are promising candidates to improve the bleaching behavior of fluorophores [88]. However, most of these compounds cannot be used for life cell experiments.

This hint motivated further work such as the imaging modality of Triplet or Dark state RElaXation (T-Rex/D-Rex) [49]. The basic principle behind T-Rex is to give the fluorophore enough time between subsequent excitation and depletion events to relax from triplet or dark state. Since the triplet state is a long living state in the s range the laser pulse repetition rate for successive illumination is around 1MHz. This low repetition rate is directly related to long image acquisition times and dTs of several ms to s are common [73][74]. T-Rex is therefore not suited to record fast dynamic processes inside living cells. Moreover the

process targets only the reduction of long living states in the order of μs . Other bleaching pathways such as higher singlet states are affected.

Reduction of Excitation and Signal suppression Cycles (RESCue)

In this chapter an alternative idea to decrease bleaching is presented which is based on the Reduction of the total number of Excitation and Signal suppression Cycles (RESCue) [89]. The approach was triggered by the idea to scan only at positions with information introduced by the adaptive scan pattern but refines it down to each scanned pixel.

During the registration of each pixel the photon count is checked continuously to identify if fluorescence information is present at a certain location. In case no fluorophore is present in the effective PSF volume, the illumination is stopped for the rest of dT. With this strategy the most promising results can be expected in case of ensemble switching high resolution microscopy utilizing metastable states. In contrast to the adaptive scan method described above RESCue reduces the total switching cycle numbers in the focal plane in case of metastable states. However, even with stable states, a reduction of the switching cycle number of fluorophores located out of focus and of phototoxic effects is achieved.

To validate the method the STED setup described above was modified. In addition two more STED setups were altered to provide a broader range of application. Technical and biological samples were imaged to distinguish the typical bleaching reduction obtained.

4.2 The basic principles of RESCue

For a normal image acquisition process each volume element is lighted for a constant dT independent of the information present at the illuminated position. Similar to adaptive beam scanning the basic idea behind RESCue is to illuminate only at positions, which provide photon information of the sample. To achieve this adaptive illumination RESCue decides in a fraction of dT if a fluorophore is present at the actual position by analyzing the photon flux. In case no object is present the illumination of the sample is stopped for this volume element for the remaining dT or the scanner simply moves on to the next registration point. To decide whether an object is present a simple rule presented by Hoebers et al. is adapted to STED [90]. The proposed method introduces two photon number thresholds to decide upon the illumination. Through a lower threshold (lTh) it is determined if an object is present at all and through an upper threshold (uTh) the illumination of very bright objects can be reduced.

The photon information during a STED scan is only collected out of a small volume located at x_{zero} . This effective detection volume is considerably smaller than the diffraction limited trans-illuminated volume. Nevertheless, an illumina-

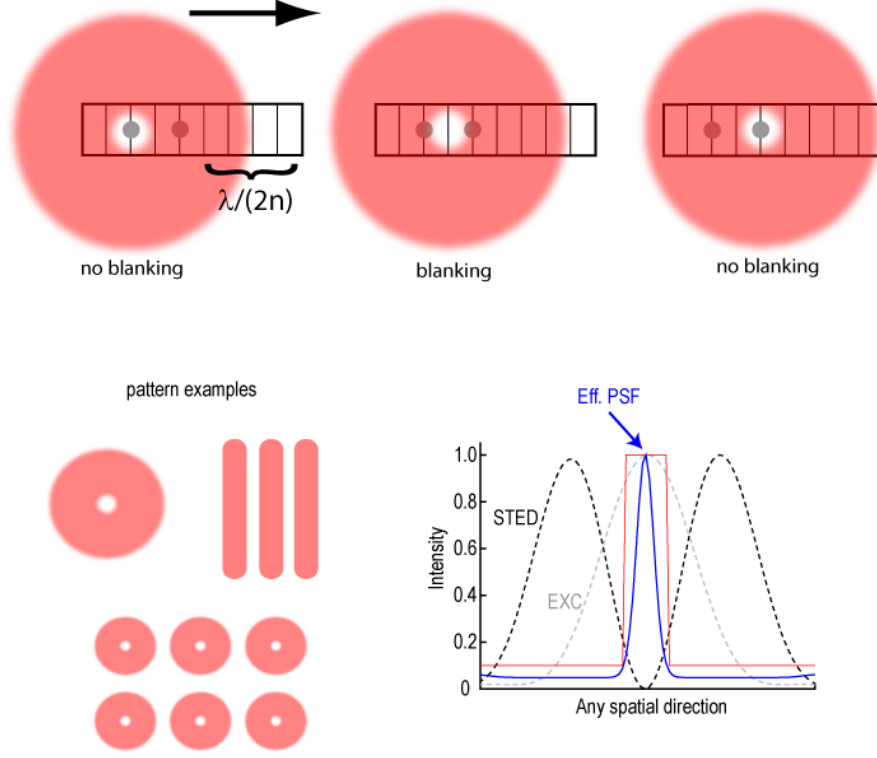


Figure 4.1: The lasers remain on for the whole dT only if an object is present within sub-diffraction accuracy. The two fluorescent objects (gray circles) are not resolvable by a conventional confocal microscope (the grid marks the pixels, the beam is scanned from left to right). In case the registration of the fluorescence is confined to the zero of the laser's beam profile inhibiting the fluorescence (red, any zero pattern), the objects are resolvable and the lasers can be blanked in regions where no fluorescence is emerging (middle). A narrower effective PSF allows exposing the sample more selectively. The number of cycles a fluorescent molecule undergoes in the RESCue-STED modality is strongly reduced compared to a conventional STED mode according to cT/dT, the systems resolution and the distribution of the fluorescent molecules. Even more: there is also the possibility that the high resolution information is crucial to reduce photo bleaching in contrast to the confocal mode.

tion decision for the small volume influences the number of switching cycles the fluorophores undergo also in the larger volume. In case no information is collected from x_{zero} the illumination is stopped and the total number of switching cycles is reduced for the complete illuminated volume without the loss of significant information (see fig. 4.1). Hence, RESCue will influence the number of switching cycles not only in out of focus regions as it is the case for confocal microscopy but also in the focal plane for all RESOLFT microscopes using metastable states. So RESCue complements the adaptive beam scanning in an optimal way.

Theoretical discussion of the illumination decision supported by lTh

For implementation a cycle time (cT) and the lTh must be defined depending on the detection efficiency and the SN before each STED scan. cT must be smaller than dT. During each pixel registration the number of photons detected within cT is compared to a lower threshold (lTh). If the number of photons is smaller than the threshold no fluorescent object is assumed in the volume at x_{zero} . A longer exposure time of this pixel would provide no more information but in contrast raises the probability to bleach the fluorophores in the complete diffraction limited volume. Consequently, the lasers are shut off for the remaining dT (see fig. 4.2a case 2). Clearly, the actual RESCue effect depends strongly on the chosen cT and lTh. The theoretical gain in switching cycle reduction for a spherical object is approximated by:

$$Gain_{lTh} \approx \frac{dT \left(\frac{V_{exc}}{V_{eff}} \right)^n}{cT \left(\frac{V_{exc}}{V_{eff}} - 1 \right)^n + dT}, \quad (4.1)$$

where n is the number of dimensions of the scan and V_{exc} and V_{eff} represent the diffraction limited illumination volume and the effective detection volume, respectively. Hereby, a sampling of the object according to the Nyquist-Shannon theorem is assumed. In practice corrections may be required, since the actual fluorophore distribution is rarely a distribution of spherical objects, which are diffraction limited spaced and show a linear bleaching dependency.

Interestingly the protective effect due to RESCue increases with higher resolution and smaller ratio cT/dT (see fig. 4.2b, c). Depending on the settings and the actual fluorophore distribution the fluorescent molecules can undergo a lower number of total switching cycles with RESCue than for a lower resolution scan without it. Actually, this is the first time higher resolution is related to less bleaching. This is not surprising because a higher resolution provides a more accurate detection of the fluorophore distribution. This information is used by RESCue (see fig. 4.1). A confocal scan will not gain any switching cycle reduction as the illumination PSF is mainly the detection PSF in the focal plane. For the out of focus planes a reduction of photon induced bleaching will be achieved.

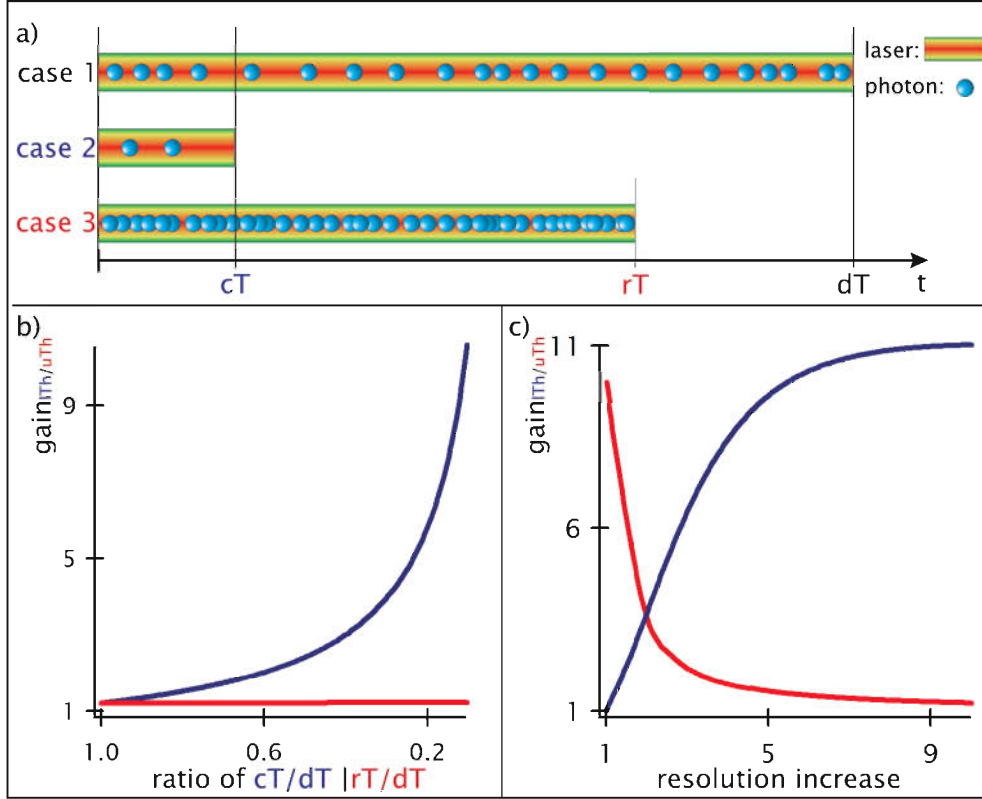


Figure 4.2: The parameter influence for RESCue; (a) Case 1 represents the condition that enough photons were detected after cT and the sample is normal illumination for the complete dT . When not enough photons were detected until cT the illuminations were blanked (case 2). The same blanking occurred in case 3, if enough photons were recorded. With decreasing ratios between cT and dT the bleaching protection increases significantly, whereas a ratio decrease between rT and dT has only a slightly positive effect (b). With higher resolution the improvement for case 2 becomes greater and the influence of the case 3 decreases for a spherical object with the size of the resolution (c).

In both cases the phototoxicity is reduced.

It has to be mentioned that the lTh as well as the cT has to be set carefully. The smallest possible lTh/cT combination is limited by the typical signal detected for background areas. This value has to be balanced with the shot noise to determine useful lTh/cT combinations.

Theoretical discussion of the illumination decision supported by uTh

Besides the lTh , which covers the possibility that no object is present, an upper threshold (uTh) can be introduced to track pixels for which a very high SN ratio is recorded. In such a case the needed SN ratio is reached before the end of

dT and the lasers can be turned off earlier. In contrast to lTh an additional timestamp has to be recorded, after which time span the uTh was reached. These read-out times (rT) must be used to correct the pixels' photon number. The correction was performed by the extrapolation of the photon count according to the ratio between rT to dT. This calculation was performed for all pixels which had reached the uTh. Since the noise plays no major role for these pixels the extrapolation should not increase the error significantly.

Similar to the lTh-case an improvement by the ratio dT/rT can be achieved theoretically for pixels with high photon numbers above uTh. In contrast to the lTh-case higher resolution decreases the achievable improvement (see fig. 4.2b, c). In fact the diffraction limited resolution represents the theoretical limit, as can be seen by:

$$Gain_{uTh} \approx \frac{dT \left(\frac{V_{exc}}{V_{eff}} \right)^n}{rT + dT \left(\frac{V_{exc}}{V_{eff}} + 1 \right)^n}. \quad (4.2)$$

The uTh resembles a measure to prevent bright spots to spend their complete fluorescence during one image acquisition. Instead, the fluorescence is conserved for future scans. These bright spots represent dense fluorophore distributions which are not resolved by the microscope. In case the resolution would be high enough even in these bright spots separated fluorophores would be measured. In such a case only the lTh would be needed for bleaching reduction.

4.3 Implementation of RESCue in STED microscopy

A typical STED setup can be easily adapted for RESCue. Two modifications are necessary. First, a fast blanking device must control the illumination of at least the excitation laser. Second, a closed loop has to be established, which utilizes the actual pixel photon number to adaptively control this shutter.

STED microscope modifications necessary for implementing RESCue

The blanking has to be fast enough to switch off the laser beam in a fraction of the adjusted cT. For the experimentally implemented cTs (see section 4.4) typical acousto optical modulators (AOM) and electro optical modulators (EOM) are fast enough. The setup presented in chapter 3 was therefore modified by an EOM to establish an illumination control of the STED laser only. The more important excitation laser diode was gated electronically via its trigger input. With this trigger the diode can be shut off within 300ns, according to its specifications. The TTL trigger signal of the photo diode is combined with the RESCue control

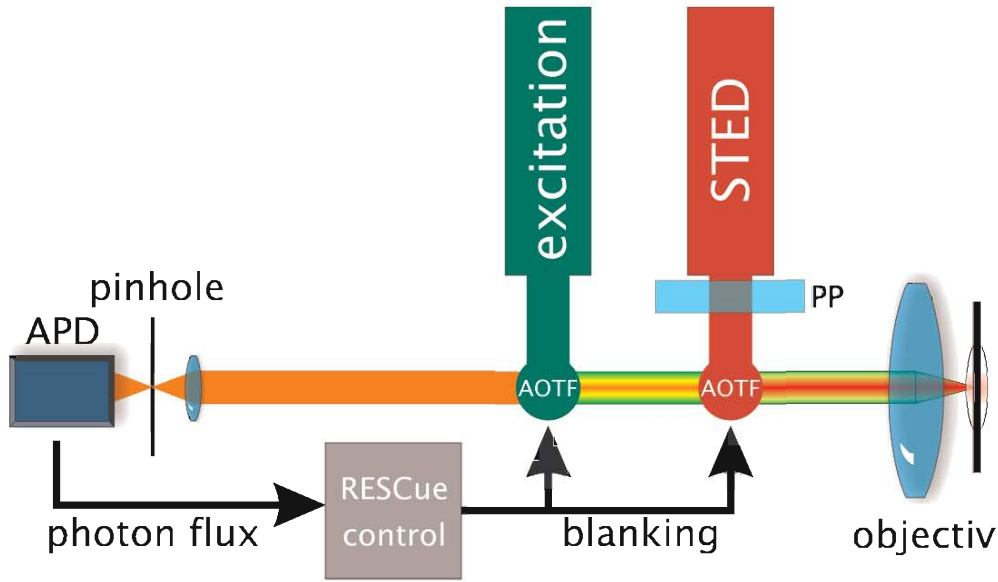


Figure 4.3: The figure represents a schematic drawing of the STED setup, which was used to measure the Nile-Red beads, the amino precursor protein (APP) and the glial fibrillary proteins (GFAP). The typically used dichroic mirrors were replaced by AOTFs. The STED donut intensity distribution in the focus is produced by a phase plate (PP). The AOTFs were controlled by the RESCue mechanism consisting of the FPGA and the custom IO board. This closed loop control distinguished between three cases (see fig. 4.2).

signal via an AND-gating in the delay box.

The concept of RESCue should provide a general improvement to all ensemble switching high resolution microscopes with metastable states. To analyze the possible advancement at all kinds of dyes and applications two other STED setups were equipped with the RESCue modality. In the setup presented by Staudt et al. [89] acousto optic tunable filters (AOTF) serving as beam splitters are used to control the illumination (see fig. 4.3).

Another modified STED setup is based on the setup presented by Harke et al. [60]. It represents the setup shown in chapter 3 but applies a common stage scanner instead of a beam scanner and the microscope stand.

RESCue control implementations

The closed loop control of the shutter system is timing critical. Hence, a stand-alone circuit board or the FPGA must be used to perform the illumination control. A home-built stand-alone circuit board applied a binary counter to track the photons measured during the cycle time [57]. In this way only the lTh could be implemented, since the uTh needs an additional recording of the rT. This simple hardware board could be easily implemented into the other STED setups but suffers from its fixed functionality.

The flexible control architecture using the FPGA mentioned in chapter 3 allows adjusting the threshold parameters during the image acquisition, in order to account for residual bleaching during repeated scans. It controlled the scanner with a loop time of 12.5ns. Hence, it was perfectly suitable to take over the adaptive control of the shutters. The FPGA scanner program was modified so that the FPGA became capable to provide the adjustment of the lTh, the cT and the uTh. In the case of uTh the photon number was directly corrected from rT to dT inside the FPGA. Besides, the rT information was transmitted to the host PC for recording.

Except for the lamina measurements, all presented experimental data was recorded with the FPGA RESCue control.

4.4 Experimental results

The RESCue-STED modality enables for the first time reduced photo-bleaching associated with increased intensities as it leads to higher resolution and therefore to a more accurate exposure control. Thus the reduction of the photo-bleaching even exceeds the fluorescence conserving in the confocal imaging. One of the ideas behind RESCue-STED is to plough back the improved bleaching behavior at higher STED intensities to push the resolution further.

The three main parameters (lTh, cT and uTh) can be freely chosen to optimize the image quality and the reduction of the photo bleaching. The user or an automatic algorithm has to provide a reasonable lTh-cT combination which accounts for all objects of interest in the sample. It turned out that the lTh parameter fundamentally influences photo bleaching during an image sequence of the same region of interest (ROI). Of course, residual bleaching occurs in the RESCue mode. Later images would therefore differ in fluorescence. Ultimately, it is necessary to provide an adjusted lTh-cT combination for each scan. As mentioned earlier this can be done by an algorithm or by the user. Nevertheless, the cT must be long enough to allow a reliable decision whether the object of interest is present or not. Finally, the parameter uTh has to be chosen depending on the desired SN.

Measurement and image analysis protocol

Miscellaneous technical and biological specimens were measured to demonstrate the reduction of the photo-bleaching by RESCue-STED compared to normal STED. The majority of the measurements were performed following the protocol above. First, a confocal overview image of the sample was recorded. Within this overview several ROIs were scanned repeatedly. Each ROI represented different settings: conventional confocal imaging (confocal), conventional STED (normal), lTh enabled RESCue-STED (lTh), uTh enabled RESCue-STED (uTh) and the lTh, uTh RESCue-STED combination (lTh&uTh). Thereafter, a second confo-

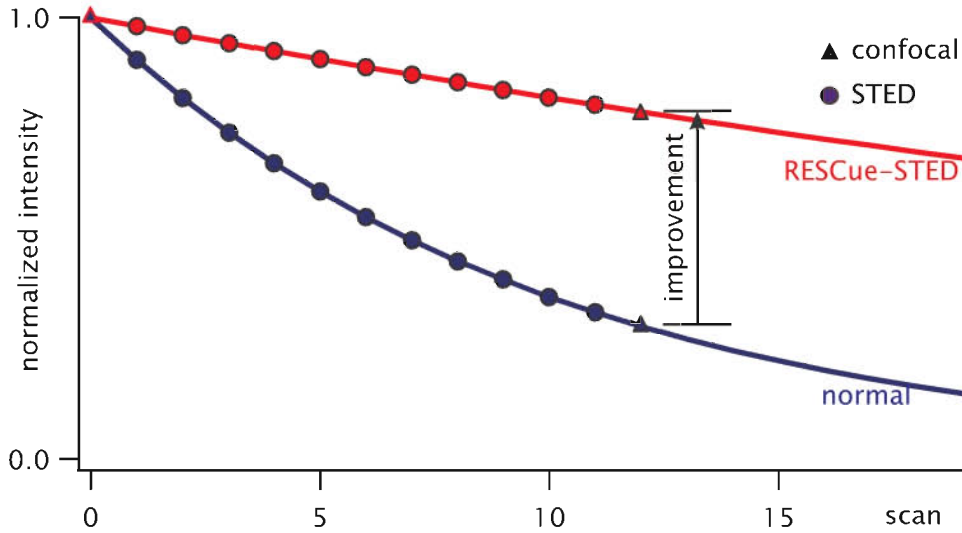


Figure 4.4: The figure demonstrates the measurement and image analyzing protocol. At the beginning of each measurement a confocal image is recorded (triangle). Thereafter a image series with different RESCue settings is recorded in STED (circle) or confocal mode. After a certain number of scans the normal STED provides no residual structural information. The remaining fluorescence in the last confocal scan is then compared for the different settings.

cal overview image including these ROIs was recorded displaying the bleaching behaviors according to the different RESCue-STED settings.

Each ROI was scanned the number of times, which was necessary to bleach the main structural information in the normal STED scan. For quantitative comparison an improvement factor is defined by the ratio of the normalized residual fluorescence (to the first confocal overview image) in the last confocal overview image between the different modes of operation (see fig. 4.4)

RESCue-STED bleaching reduction demonstrated with Nile-red fluorospheres

The Nile-Red beads were similarly prepared as the crimson beads (see appendix A). A confocal overview the fluorosphere sample was scanned (fig. 4.5a). Each of the first four ROIs in the column was imaged 10 times in each RESCue-STED mode (fig. 4.5b). The ROIs were 1200nm x 1200nm in size, scanned with a pixel size of 20nm x 20nm and a pixel dwell time of 400 μ s. The lTh was set to 5 photons, the cT to 50 μ s. The uTh parameter was 28 photons. After all ROIs were scanned, the second confocal overview scan was performed (fig. 4.5c).

The STED mode recognized sharp spots of 35nm FWHM while imaging the 21nm sized beads. Compared to the confocal image, the STED image provided

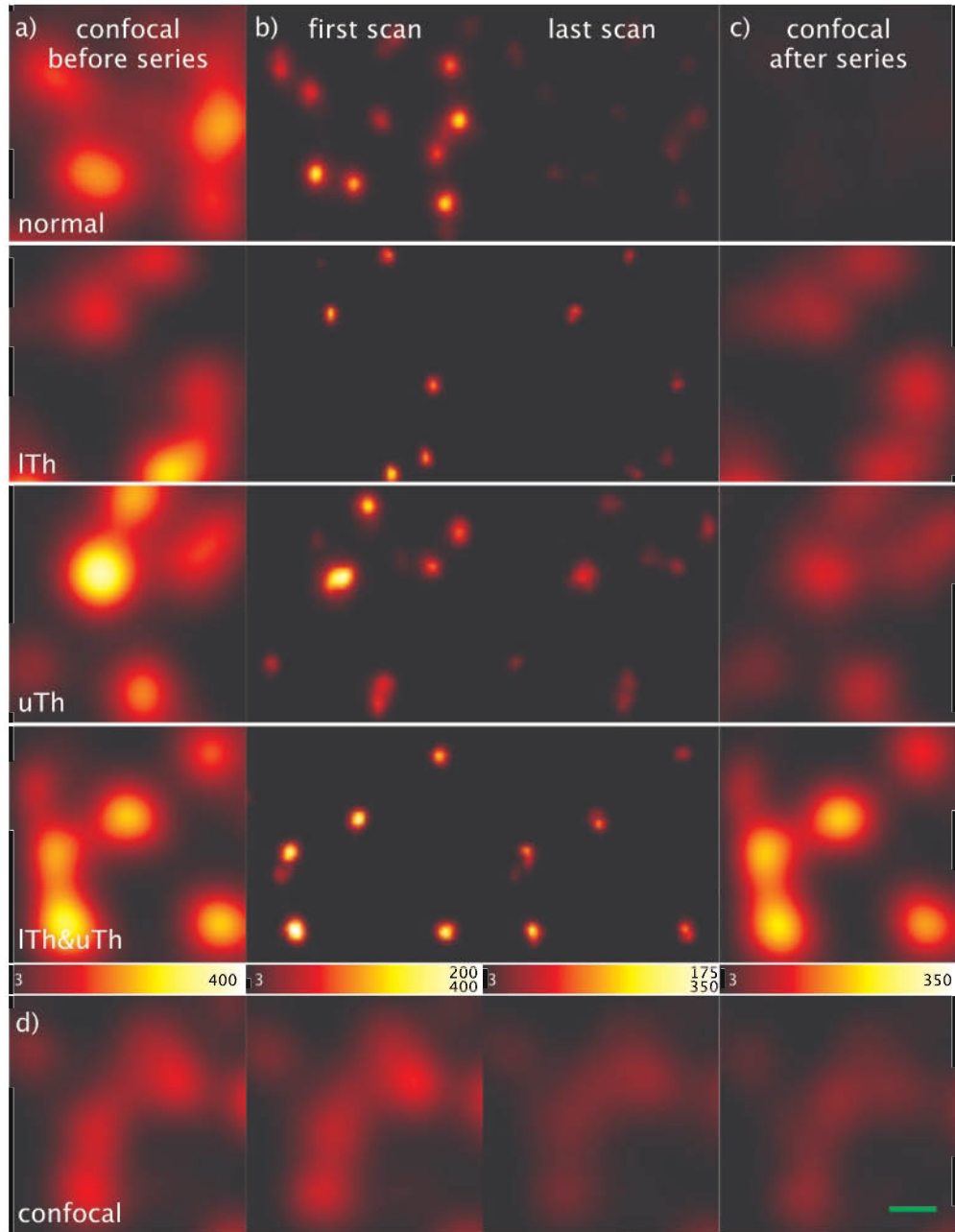


Figure 4.5: Bleaching is reduced by a factor of 12 in the RESCue mode. This improvement is exemplified by recording fluorescent Nile red nano-particles compared to the standard STED mode. A factor of 1.5 was achieved compared to the standard confocal mode (d). The confocal overview (c) presents the fluorescence of four ROIs, each after a series of ten scans performed in the STED mode (b). Each ROI is recorded with the same scan parameters but different RESCue settings. In the upper row (normal) RESCue was disabled. The second row (lTh) was imaged with a lTh of 5 and a cT of 50 μ s. The third row (uTh) displays the measurement with a uTh of 28 photons and no lTh active. The penultimate row (lTh&uTh) was imaged with lTh and uTh active. In the last row (confocal) a series is shown to demonstrate the photo-bleaching caused by pure confocal imaging (d). Only the first and last STED scan are displayed. The scale bar represents 300nm. All images were linearly deconvolved.

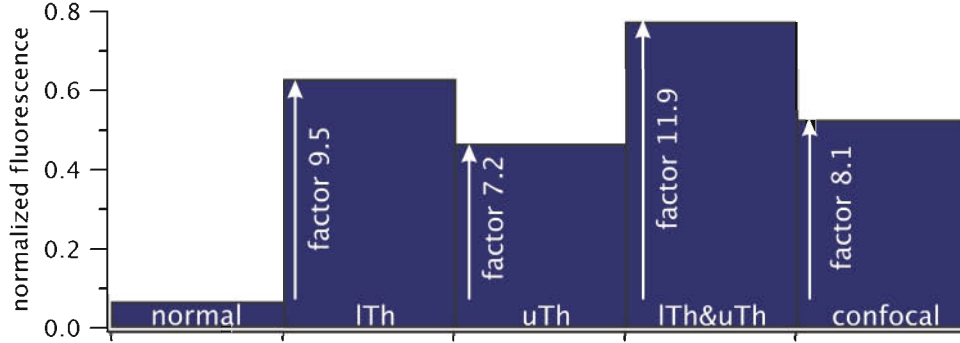


Figure 4.6: The figure shows the introduced ratio improvement factor of the normalized residual fluorescence according to the different scan modalities of fig. 4.5. The bars height corresponds to the residual fluorescence whereas the factor arrows indicate the improvement of residual fluorescence compared to the normal STED mode.

a 36-fold reduction of the spot size in the xy-plane. The photo bleaching in the conventional STED mode was apparent by a 15-fold reduced fluorescent signal after ten scans (fig. 4.5b, c and fig. 4.6 normal). The high excitation and de-excitation cycle numbers the dye molecule underwent under STED conditions was associated with a pronounced bleaching. Reduction of the excitation and STED beam dose by applying RESCue reduced the cycle numbers significantly. By introducing the lTh, an improvement of factor 9.5 was achieved (see fig. 4.5b and fig. 4.6 lTh) concerning photo bleaching. This improvement could be even exceeded by introducing the parameter uTh. This parameter alone provided a similar reduction in photo bleaching as in the case of the lTh (see fig. 4.5b uTh). The improvement was a factor of 7.2 (see fig. 4.6 uTh). Combined with the lTh the additional parameter uTh enabled a further enhancement in reducing the photo-bleaching by a factor of 1.25 compared to the RESCue modality only accounting for lTh (fig. 4.5b lTh&uTh). In total a factor of 12 in reducing photo bleaching was proved by applying the full RESCue package (see fig. 4.6 lTh&uTh) including the uTh parameter in densely labeled samples. Comparing the photo bleaching in the confocal mode (see fig. 4.5d) with that of the RESCue mode taking advantage of the lTh parameter shows impressively the potential of instantaneously adapting the high resolution information to the sample exposure: nearly 20% of the fluorescence were saved in the RESCue mode only applying the lTh compared to the confocal mode and nearly 50% compared to the full implementation of RESCue (see fig. 4.6 lTh&uTh and confocal).

The major influence of lTh in case of sparse dye distribution

Next these promising results were transferred to biological relevant problems. Amyloid precursor proteins (APP) of primary mouse neurons (DIV8) were immunostained with Atto565. Fig. 4.7a shows a confocal and a STED image respectively of the labeled APP located in the plasma membrane. The STED image displays well separated APP spots in contrast to the confocal image. The resolution in the STED mode was around 45nm and limited only by the STED laser's intensity.

With the given resolution and sparse structures a major impact of RESCue with a well adjusted lTh was predictable. The lTh was chosen with 6 photons within 40 μ s for cT. As before, a confocal overview was recorded with 50nm pixel size and a dwell time of 500 μ s (see fig. 4.7b). The three (RESCue-) STED ROIs were recorded with a dwell time of 300 μ s and else identical settings as for fig. 4.5. As shown in the images, a 4.5 fold improvement regarding the photo bleaching between the RESCue with lTh (see fig. 4.7c lTh and fig. 4.8 lTh) and the conventional STED measurement is obvious (see fig. 4.7c normal and fig. 4.8 normal). The APP was sparsely distributed over the specimen. In this case, the involvement of the RESCue parameter uTh, which was set to 25 photons led to an additional factor of only 1.11 reduction in photo bleaching, corresponding to an overall factor of 5 (see fig. 4.7c lTh&uTh and fig. 4.8 lTh&uTh).

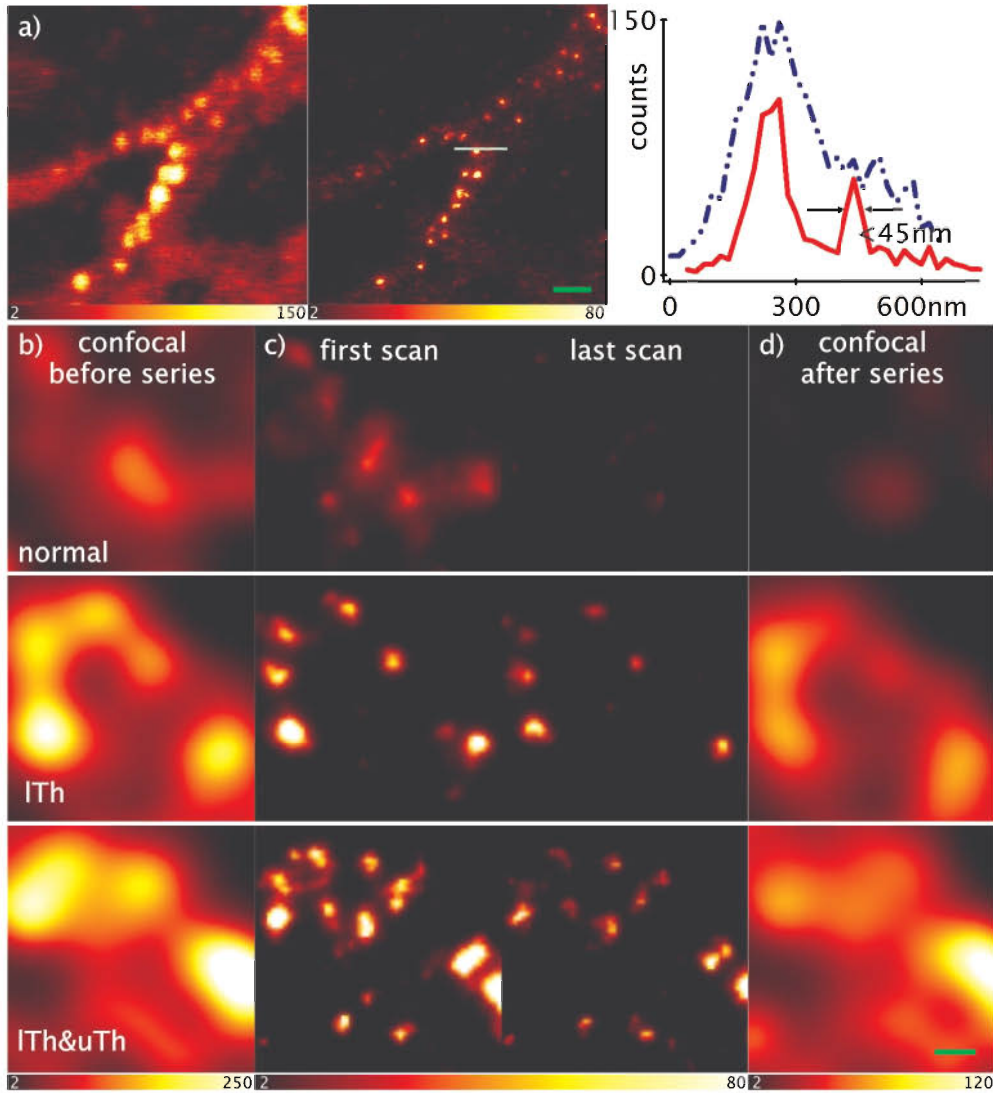


Figure 4.7: Imaging in the RESCue mode reduced the photo bleaching of Atto565 labeled APP in fixed, permeabilized primary mouse neurons by a factor of 5. Like for the Nile red fluorospheres first a confocal scan (b), then the STED scan series (c) and last a confocal overview scan (d) was performed. An additional check of the STED resolution performance (a) revealed a resolution of 45nm (a, right side). Without the RESCue mode enabled (c, normal) strong bleaching inhibited the data acquisition. Imaging under RESCue conditions led to an impressive fluorescence preservation (lTh and lTh&uTh). The RESCue parameters were set to: lTh of 6 photons, uTh to 25 and cT of 40 μ s. Because of the sparse distribution of the APP, the bleaching behavior was not significantly improved by setting the uTh. All images in b), c) and d) were linearly deconvolved. The scale bar represents 250nm.

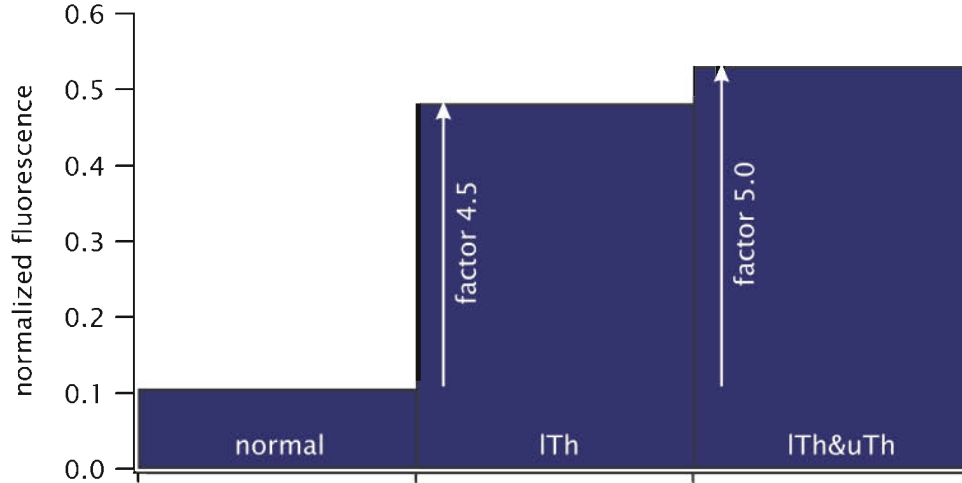


Figure 4.8: The normalized residual fluorescence for the different STED modes. The bars correspond to the residual fluorescence. The arrows indicate the improvement compared to the normal STED scan.

RESCue-STED GFAP: dense dye distributions benefit from the lTh and uTh

The influence of the parameter uTh was hindered in case of the point like distribution of the APP. To validate that only this sparse distribution of fluorescent spots prohibits a further improvement with the aid of the parameter uTh, the glial fibrillary protein (GFAP) immunostained with Atto565 was imaged. GFAP is an intermediary filament in the cytoplasm of glial cells. Here, the dye molecules were densely packed on a filament, as can be seen in the confocal image (see fig. 4.9a). Except the uTh, which was changed from 25 to 28, all settings were identical to the settings to acquire the APP data. This time, an apparent difference in the bleaching behavior between RESCue supported only by the lTh and the full implementation (lTh&uTh) could be observed (see fig. 4.9b, c lTh and lTh&uTh). As was the case with the dense bead sample, an additional factor of 1.34 bleaching reduction was achieved between the lTh-RESCue and the usage of both thresholds, resulting in an overall 3.5-fold photo bleaching behavior improvement (see fig. 4.9d).

The fluorescence of densely distributed dye molecules, as shown in fig. 4.9 , can be more preserved by using the parameter uTh. Also a given lower resolution would benefit from the uTh parameter. The uTh preserved the fluorescence further as it directly reduces the fluorescence cycles of the dye molecules leading to detectable photons, however it lacks the significance of the lTh as this threshold gains from the zero based high resolution information. In samples displaying

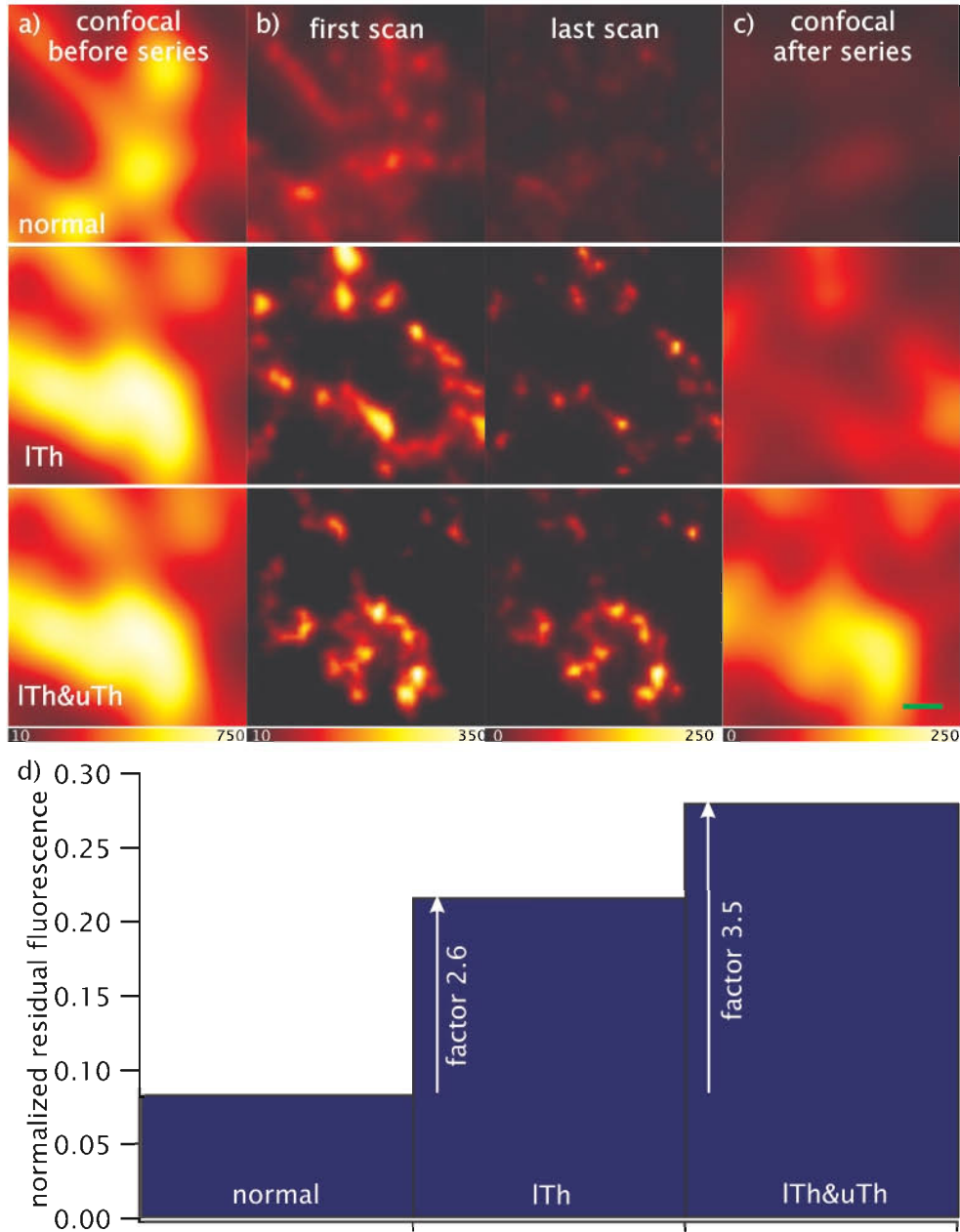


Figure 4.9: The additional parameter uTh further increased the bleaching reduction in Atto565 immunostained glial fibrillary proteins (GFAP) in glioblastoma cells (U373) to an overall factor of 3.5. Analogous to fig. 4.7, the confocal image (a) represented the sample before the accomplishment of the STED scans. Without an enabled RESCue mode, the sample bleached rapidly (b, normal). With the lTh of 6 photons and cT of $40\mu s$ the fluorescence of the densely labeled filaments could be preserved impressively (b, lTh). However, even with the aid of the lTh the fluorescence bleached significantly. Due to the additional parameter uTh of 28 photons, the bleaching reduction can be further improved by a factor of 1.34 to an overall factor of 3.5 (b, $lTh\&uTh$). After the series of STED scans a confocal overview was recorded to demonstrate the effect of the RESCue mode in preserving the fluorescence (c). All factors are collected in a bar diagram (d). All images were linearly deconvolved. The scale bar represents 250nm.

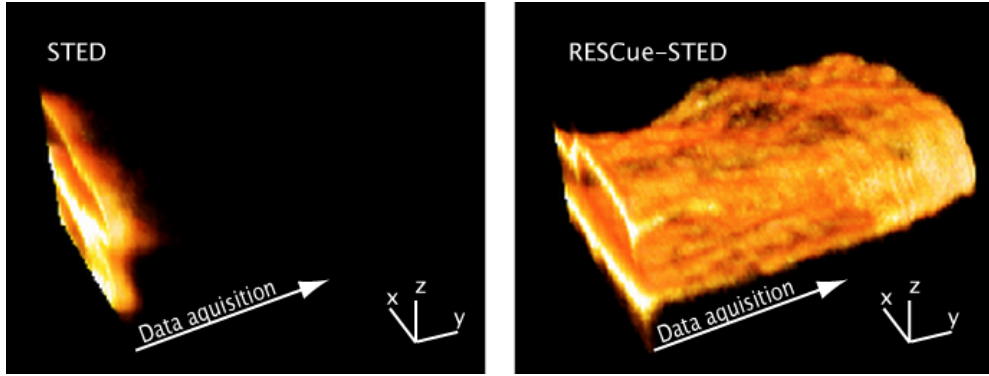


Figure 4.10: RESCue allows for the measurement of A647N immunostained nuclear lamina in neuroblastoma cells in 3D. The left image (STED) shows the attempt to image the lamina without RESCue enabled but fails because of pronounced bleaching. The image on the right side (RESCue-STED with only lTh enabled) demonstrates that the recording becomes possible with the aid of RESCue.

overlapping STED PSFs with respect to the Rayleigh criterion, the fluorescence in the middle of two hardly separable signals is probably higher than the adjusted lTh and the lasers are not blanked to reduce the switching cycle numbers. In these cases a significantly lower lTh helps, but this can in contrast degrade the image quality.

RESCue-STED of lamina: enabling measurements in three dimensions

There are not only scenarios conceivable profiting by an improved bleaching behavior under RESCue conditions. Some problems can be especially addressed by the RESCue-STED modality, thereby opening up the possibility to get the desired information. One example of that is shown in figure 4.10 illustrating the RESCue-STED application to 3D measurements. Here, Atto647N labeled Lamina was imaged in three dimensions. dT was set to 100 μ s, cT to 30 μ s and the lTh was 426 photons. The figure shows a 3D surface rendered view of the nuclear lamina. On the left hand side the measurement of the standard STED mode is presented. The 3D data stack was generated by sequential xz-scans in y-direction. After a few xz-sections the fluorescence was lost due to photo bleaching. On the right hand side a measurement performed in the RESCue-STED mode taken with the same STED settings as in the previous measurement is shown. RESCue enabled the acquisition of 3D data stacks, which could not be achieved otherwise. Especially in 3D applications, the fluorescence must be conserved in the close neighborhood of the focus by blanking the lasers whenever possible.

4.5 Discussion and Summary

The potential to observe dynamic processes in living cells as well as the imaging of 3D structures inside living cells are two major advantages of the fluorescence far-field microscopy compared to other microscopy techniques such as AFM. However, especially these fields require repetitive scans, which are connected to high light doses damaging the sample. RESCue decreases the photo-bleaching significantly even inside the focal plane for ensemble switching high resolution techniques using metastable states. Less photo bleaching increases the applicability of the microscope. In contrast to T-Rex (see section 4.1) no image acquisition speed decrease is observed.

By using the lTh parameter alone typically bleaching is reduced by a factor of four without sacrificing resolution or imaging speed. The use of uTh increases the bleaching reduction typically to a factor of 4.5. Densely labeled structures as presented with the immunostained GFAP in glial cells are even better preserved by the uTh.

Higher resolution opens up the possibility for a more selective exposure of the sample minimizing the dyes excitation and signal suppression cycle numbers. RESCue aided high resolution STED imaging bleaches less than the same scan in confocal mode. Measurements of the technical sample demonstrate impressively that the RESCue mode preserves the fluorescence by 20% better than the confocal mode with the aid of the high resolution information. The impact on relevant biological samples is analyzed at APP in neurons and the above mentioned GFAP in glial cells. However, RESCue even opens up new options. It enables the 3D measurement of lamina labeled neuroblastoma cells, which could not be imaged without RESCue.

If the resolution enhancement is based on long-lived or stable off-states, the phototoxicity should be reduced due to the diminishment of the light dose on cells.

The key point of RESCue is to detect the presence of an object by photon information. Coincident photons on two detectors would allow a fast decision on the presence of an object if this object of interest is labeled with several dyes making coincidence measurements probable.

The FPGA based RESCue implementation allows one to optimize the RESCue parameters cT, lTh and uTh during measurements. This option is especially important if a series is recorded and one needs to account for the changing properties of the samples during the measurement. If the sample is bleaching during repeated scans in life cell applications, for example, the lTh parameter can be adapted.

The major impact of RESCue lies in enabling ensemble switching high reso-

lution microscopy measurements based on metastable states of samples that are prone to photo-bleaching such as 3D STED measurements, application of coumarine dyes in biological samples and fluorescent proteins in high resolution microscopy. In the STED case the reduced bleaching in standard applications may be reinvested in higher intensities and therefore higher resolution.

But mostly, the live cell ensemble switching nanoscopy should benefit from the RESCue modality because the examination of dynamic processes within the cells calls for repeated scans. Here the impact of photo-bleaching of the fluorescent dyes is most crucial as well as the phototoxicity caused by high light doses eventually leading to artifacts and cell death. Both effects can be minimized by applying RESCue. It reduces the light dose illuminating the specimen and therefore photo bleaching and dark state transitions. This improvement is achieved avoiding anti-bleaching agents, which are interfering with life cell imaging.

5 Conclusion and Outlook

The most important field of application for optical far-field microscopes such as STED microscopy is the observation of dynamic processes and 3D structures inside living cells. Its high spatial resolution provides new insights to cell biology. The novel adaptive techniques for STED microscopy proposed in this thesis improve the performance for this task.

STED suffers from increased bleaching and limited resolution in case of a non-perfect intensity zero of the depletion pattern. Additional aberrations of the optical setup can amplify this degradation of the STED PSF and hinder the STED microscope to work at its optimum. Constant phase masks cannot provide any mean to optimize the setup. Adaptive phase mask devices, such as SLMs, deliver not only the freedom to implement any desired phase pattern using only one device but also offer the possibility to compensate for phase errors of the STED beam.

The novel error correction method presented here enables the calibration of SLMs only by phase stepping interference measurements and with considerably lower effort and higher exactness than known calibrations. For the first time such an error correction method was validated not only by phase error measurements but also with STED measurements of dye filled polystyrene micro spheres. The error corrected SLM provides a versatile tool to test new phase mask concepts and to provide for any STED setup optimal fluorescence collection efficiency and resolution.

Nevertheless, the aberrations introduced by the system are only corrected for one particular scan position. Due to sample induced refractive index variations and varying optical beam paths the aberrations change during a scan.

In the future faster SLMs could also correct for these locally varying aberrations at least for each x-y layer in a 3D scan. The required quality feedback could be provided either by an introduced beacon into the sample or a quality criterion such as highest resolution or highest signal. For the latter proposal, dyes with significantly higher bleaching resistance are necessary, such as the recently published diamond color centers [79].

With the optimized resolution and contrast performance the STED setup is prepared for imaging of static objects at least in 2D. However, the observation of fast dynamic processes inside living cells call for equally fast registration of

those events. For the first time, a beam scanner based on common galvanometers was introduced for STED microscopy. Besides the scanning speed of small FOVs down to effective pixel dwell times of $5.8\text{ }\mu\text{s}$ for technical samples, a pixel dwell time of $15\text{ }\mu\text{s}$ for considerable larger FOVs was demonstrated at biologically relevant samples without any of the disadvantages of competing concepts. These STED images of APP illustrate the unique features of the galvanometer beam scanner to image small to medium sized FOVs in unimpaired quality in time spans below a second.

This novel scanner was combined with an adaptive scan pattern, proposed for the first time. It only works effectively in combination with ensemble switching high resolution microscopy. The combination of the presented beam scanner and the adaptive pattern enabled the observation of very large FOVs with STED resolution in only a fraction of the time needed with the classical stage scanning approach. A reduction of image acquisition time with the adaptive beam scanner without any information loss compared to a normal STED scan was demonstrated by STED measurements of technical samples. Combined with the faster scanning capabilities, the imaging speed was shortened by a factor of around 30 compared to a classical stage scanner.

This advantage was used to image focal adhesions of human fibroblasts with the largest FOV ever reported for a STED microscope. The demonstrated image acquisition speed relates to the shortest ever announced pixel dwell time achieved for a biological sample imaged with a STED microscope. Additionally, the image SN ratio was comparable to scans performed with eight times longer pixel dwell time.

The still existent bleaching of fluorescent markers for living cell microscopy hinders the repetitive scans and the measurement of 3D structures of living cells with the adaptive pattern scanning STED microscope. Fluorescent proteins and coumarines are prone to bleaching. The adaptive illumination scheme "RESCue" presented in this thesis tackles this problem by adapting the selective illumination used for CLEM for STED microscopy. Hereby, the unique feature of STED to detect photons emitted by a smaller volume than the diffraction limited illumination volume significantly decreases the applied illumination dose without the loss of information this behavior is unique to ensemble switching techniques. For the first time, the better localization capability of STED compared to confocal microscopy is linked to less bleaching and dark state transitions.

This fact was validated with STED measurements of fluorescent beads. An increase of residual intensity by a factor of 12 compared to the normal STED scan and still 50% compared to a confocal scan was demonstrated. Additional measurements of biological samples revealed a similar bleaching reduction. The novel method was applied to enable the 3D STED measurement of the nuclear lamina in neuroblastoma cells. In comparison to other proposed methods, RES-

Cue does not slow down the acquisition speed. Instead, a fast scanner can profit from RESCue by an overall decreased image acquisition time.

The proposed adaptive elements represent each unique and novel possibilities to take STED deeper into the field of biological relevant applications. Each one enables measurements which were not possible before. However, these methods can be combined with each other and with already existing methods, especially for bleaching reduction. A combination of the adaptive beam scanner with RESCue is possible and should result in unique image acquisition times for large FOVs and reduced bleaching. For 3D measurements, the advantageous effects of both methods will complement each other resulting in further reduced bleaching for out of focus layers.

In the future the adaptive scan and illumination can be even further refined by recursive working algorithms using the tunable resolution of STED microscopes and combined with even faster controls such as EOMs to allow additionally triplet relaxation without sacrificing imaging speed and further improved sample protection.

Bibliography

- [1] F. de Lange, A. Cambi, R. Huijbens, B. de Bakker, W. Rensen, M. Garcia-Parajo, N. van Hulst, and C. G. Figdor. Cell biology beyond the diffraction limit: near-field scanning optical microscopy. *Journal of Cell Science*, 114(23):4153–4160, 2001.
- [2] A. I. Kirkland and L. Hutchinsons. Atomic resolution transmission electron microscopy. In P. W. Hawkes and J. C. H. Spence, editors, *Science of Microscopy*, volume I, chapter 1, pages 6400–64. Springer, 2007.
- [3] M. Knoll and E. Ruska. Das Elektronenmikroskop. *Zeitschrift für Physik*, 78:318–339, 1932.
- [4] F. Zernike. The phase contrast process in microscopic examinations. *Physikalische Zeitschrift*, 36:848–851, 1935.
- [5] R. Rottermann, W. Spirig, and B. Schoenenberger. Arrangement for dark field illumination, 1985. EP 19850113306.
- [6] J. R. Lakowicz. *Principles of fluorescence spectroscopy*. Springer, Berlin, Germany, 3 edition, 2006.
- [7] A. H. Coons, H. J. Creech, R. N. Jones, and E. Berliner. The demonstration of pneumococcal antigen in tissues by the use of fluorescent antibody. *Journal of Immunology*, 45:159–170, 1942.
- [8] O. Shimomura. The discovery of aequorin and green fluorescent protein. *Journal of Microscopy*, 217(1):3–15, 2005.
- [9] P. I. Bastiaens and A. Squire. Fluorescence lifetime imaging microscopy: spatial resolution of biochemical processes in the cell. *Trends in Cell Biology*, 9(2):48–52, 1999.
- [10] E. A. Jares-Erijman and T. M. Jovin. FRET imaging. *Nature Biotechnology*, 21(11):1387–1395, 2003.
- [11] E. A. J. Reits and J. J. Neefjes. From fixed to FRAP: Measuring protein mobility and activity in living cells. *Nature Cell Biology*, 3:E145–E147, 2001.

- [12] T. K. L. Meyvis, S. C. De Smedt, P. Van Oostveldt, and J. Demeester. Fluorescence recovery after photobleaching: A versatile tool for mobility and interaction measurements in pharmaceutical research. *Pharmaceutical Research*, 16(8):1153–1162, 1999.
- [13] D. Magde, E. L. Elson, and W. W. Webb. Thermodynamic fluctuations in a reacting system: Measurement by fluorescence correlation spectroscopy. *Physical Review Letters*, 29:705–708, 1972.
- [14] E. L. Elson and D. Magde. Fluorescence correlation spectroscopy i. conceptual basis and theory. *Biopolymers*, 13:1–27, 1974.
- [15] M. Minsky. Microscopy apparatus, 1961. US Patent 3,013,467.
- [16] M. Born and E. Wolf. *Principles of Optics*. Pergamon Press, Oxford, 6th edition, 1993.
- [17] James B. Pawley (ed.). *Handbook of biological confocal microscopy*. Springer, New York, 3rd edition, 2006.
- [18] E. Abbe. Beiträge zur Theorie des Mikroskops und der mikroskopischen Wahrnehmung. *Archiv für Mikroskopische Anatomie*, 9:413–420, 1873.
- [19] K. König, Y. Tadir, P. Patrizio, M. W. Berns, and B. J. Tromberg. Effects of ultraviolet exposure and near infrared laser tweezers on human spermatozoa. *Human Reproduction*, 11(10):2162–2164, 1996.
- [20] J. S. Ploem and H. J. Tanke. *Introduction to Fluorescence Microscopy*. Oxford University Press, Oxford, 1 edition, 1987.
- [21] H. Nyquist. Certain topics in telegraph transmission theory. *Trans. AIEE*, 47:617–644, 1928.
- [22] C. E. Shannon. Communication in the presence of noise. *Proc. Inst. Radio Eng.*, 37:10–21, 1949.
- [23] G. Q. Xiao and G. S. Kino. A real-time confocal scanning optical microscope. *Proceedings of SPIE*, 809:107–113, 1987.
- [24] W. Denk, J. H. Strickler, and W. W. Webb. Two-photon laser scanning fluorescence microscopy. *Science*, 248:73–76, 1990.
- [25] K. König. Multiphoton microscopy in life sciences. *Journal of Microscopy*, 2000.
- [26] F. Helmchen and W. Denk. Deep tissue two-photon microscopy. *Nature Methods*, 2(12):932–940, 2005.

-
- [27] W. R. Zipfel, R. M. Williams, and W. W. Webb. Nonlinear magic: multiphoton microscopy in the biosciences. *Nature Biotechnology*, 21(11):1369–1377, 2003.
 - [28] S. Hell and E. H. K. Stelzer. Properties of a 4Pi confocal fluorescence microscope. *Journal of the Optical Society of America A*, 9(12):2159–2166, 1992.
 - [29] M. C. Lang, T. Staudt, J. Engelhardt, and S. W. Hell. 4pi microscopy with negligible sidelobes. *New Journal of Physics*, 10:1–13, 2008.
 - [30] S. W. Hell and J. Wichmann. Breaking the diffraction resolution limit by stimulated emission: stimulated-emission-depletion fluorescence microscopy. *Optics Letters*, 19(11):780–782, 1994.
 - [31] J. J. Sieber, K. I. Willig, R. Heintzmann, S. W. Hell, and T. Lang. The SNARE motif is essential for the formation of syntaxin clusters in the plasma membrane. *Biophysical Journal*, 90(8):2843–2851, 2006.
 - [32] K. I. Willig, R. R. Kellner, R. Medda, B. Hein, S. Jakobs, and S. W. Hell. Nanoscale resolution in GFP-based microscopy. *Nature Methods*, 3:721–723, 2006.
 - [33] R. R. Kellner, C. J. Baier, K. I. Willig, S. W. Hell, and F. J. Barrantes. Nanoscale organization of nicotinic acetylcholine receptors revealed by stimulated emission depletion microscopy. *Neuroscience*, 2006.
 - [34] B. Hein, K. I. Willig, and S. W. Hell. Stimulated emission depletion (sted) nanoscopy of a fluorescent protein-labeled organelle inside a living cell. *PNAS*, 105(38):14271–14276, 2008.
 - [35] U.V. Nägerl, K. I. Willig, B. Hein, S. W. Hell, and T. Bonhoeffer. Live-cell imaging of dendritic spines by sted microscopy. *PNAS*, 105(48):18982–18987, 2008.
 - [36] V. Westphal, S. O. Rizzoli, M. A. Lauterbach, D. Kamin, R. Jahn, and S. W. Hell. Video-rate far-field optical nanoscopy dissects synaptic vesicle movement. *Science*, 320:246–249, 2008.
 - [37] S. W. Hell. Far-field optical nanoscopy. *Science*, 316:1153–1158, 2007.
 - [38] M. Hofmann, C. Eggeling, S. Jakobs, and S. W. Hell. Breaking the diffraction barrier in fluorescence microscopy at low light intensities by using reversibly photoswitchable proteins. *Proceedings of the National Academy of Sciences*, 102(49):17565–17569, 2005.

-
- [39] S. W. Hell. Microscopy and its focal switch. *Nature Methods*, page DOI:10.1038/NMETH.1291, 2008.
- [40] S. W. Hell. Toward fluorescence nanoscopy. *Nature biotechnology*, 21(11):1347–1355, 2003.
- [41] S. W. Hell and M. Kroug. Ground-state-depletion fluorescence microscopy: A concept for breaking the diffraction resolution limit. *Applied Physics B: Lasers and Optics*, 60(5):495–497, 1995.
- [42] S. Bretschneider, C. Eggeling, and S. W. Hell. Breaking the diffraction barrier in fluorescence microscopy by optical shelving. *Physical review letters*, 98(21):218103, 2007.
- [43] J. Keller, A. Schönle, and S. W. Hell. Efficient fluorescence inhibition patterns for RESOLFT microscopy. *Optics Express*, 15(6):3361–3371, 2007.
- [44] R. Schmidt, C. A. Wurm, S. Jakobs, J. Engelhardt, and S. W. Egner, A. Hell. Spherical nanosized focal spot unravels the interior of cells. *Nature Methods*, 5(6):539–544, 2008.
- [45] B. Harke, C. Ullal, J. Keller, and S. W. Hell. Three-dimensional nanoscopy of colloidal crystals. *Nano Letters*, 8(5):1309–1313, 2008.
- [46] B. Harke. *3D STED Microscopy with Pulsed and Continuous Wave Lasers*. PhD thesis, Georg-August University of Goettingen, 2008.
- [47] J. Keller. *Optimal de-excitation patterns for RESOLFT-microscopy*. PhD thesis, Rupertus Carola University of Heidelberg, 2006.
- [48] T. A. Klar and S. W. Hell. Subdiffraction resolution in far-field fluorescence microscopy. *Optics Letters*, 24(14):954–956, 1999.
- [49] G. Donnert, C. Eggeling, and S. W. Hell. Major signal increase in fluorescence microscopy through dark-state relaxation. *Nature Methods*, 4(1):81–86, 2007.
- [50] W. Heisenberg. *Prinzipien der Quantentheorie*. Hirzel-Verlag, Leipzig, 1st edition, 1930.
- [51] J. Lippincott-Schwartz and G. H. Patterson. Development and use of fluorescent protein markers in living cells, 2003.
- [52] E. Betzig, G. H. Patterson, R. Sougrat, O. W. Lindwasser, S. Olenych, J. S. Bonifacino, M. W. Davidson, J. Lippincott-Schwartz, and H. F. Hess. Imaging intracellular fluorescent proteins at nanometer resolution. *Science*, 313(5793):1642–1645, 2006.

- [53] M. J. Rust, M. Bates, and X. Zhuang. Sub-diffraction-limit imaging by stochastic optical reconstruction microscopy (storm). *Nature Methods*, 3:793–796, 2006.
- [54] S. T. Hess, T. P. K. Girirajan, and M. D. Mason. Ultra-high resolution imaging by fluorescent photoactivation localization microscopy (fpalm). *Biophysical Journal*, 91:4258–4272, 2006.
- [55] R. Y. Tsien and A. Waggoner. Fluorophores for confocal microscopy: photophysics and photochemistry. *Handbook of Biological Confocal Microscopy*, pages 153–161, 1990.
- [56] J. Widengren, A. Chmyrov, C. Eggeling, P. A. Löfdal, and C. A. M. Seidel. Strategies to improve photostabilities in ultrasensitive fluorescence spectroscopy. *Journal of Physical Chemistry A*, 111(3):429–440, 2007.
- [57] T. Staudt. *Strategies to reduce photobleaching, dark state transitions and phototoxicity in subdiffraction optical microscopy*. PhD thesis, Rupertus Carola University of Heidelberg, 2009.
- [58] P. S. Dittrich and P. Schille. Photobleaching and stabilization of fluorophores used for single-molecule analysis. with one-and two-photon excitation. *Applied Physics B: Lasers and Optics*, 73(8):829–837, 2001.
- [59] L. A. Deschenes and V. B. DA. Single molecule photobleaching: increasing photon yield and survival time through suppression of two-step photolysis. *Chemical Physics Letters*, 365(5):387–395, 2002.
- [60] B. Harke, J. Keller, C. K. Ullal, V. Westphal, A. Schönle, and Hell S. W. Resolution scaling in sted microscopy. *Optics Express*, 16(6):4154–4162, 2008.
- [61] M. Dyba and S. W. Hell. Photostability of a fluorescent marker under pulsed excited-state depletion through stimulated emission. *Applied Optics*, 42(25):5123–5129, 2003.
- [62] T. Watanabe, Y. Idasaki, N. Fukuchi, M. Sakai, S. Ishiuchi, M. Fujii, T. Omatsu, K. Yamamoto, and Y. Iketaki. Formation of a doughnut laser beam for super-resolving microscopy using a phase spatial light modulator. *Optical Engineering*, 43(5):1136–1143, 2004.
- [63] M. A. A. Neil, T. Wilson, and R. Juskaitis. A wavefront generator for complex pupil function synthesis and point spread function engineering. *Journal of Microscopy*, 197:219–223, 1999.
- [64] M. J. Booth, M. A. A. Neil, and T. Wilson. Aberration correction for confocal imaging in refractive index mismatched media. *Journal of Microscopy*, 192:90–98, 1998.

- [65] T. Shirai, T. H. Barnes, and T. G. Haskell. Adaptive wave-front correction by means of all-optical feedback interferometry. *Optics Letters*, 25(11):773–775, 2000.
- [66] Rueckel M., J. A. Mack-Bucher, and W. Denk. Adaptive wavefront correction in two-photon microscopy using coherence-gated wavefront sensing. *PNAS*, 103(46):17137–17142, 2006.
- [67] L. Zhu, P. C. Sun, D. U. Bartsch, W. R. Freeman, and Y. Fainman. Adaptive control of a micromachined continuous deformable mirror for aberration compensation. *Applied Optics*, 38(1):168–176, 1999.
- [68] C. Slinger, F. Li, C. Cameron, and M. Stanley. Computer-generated holography as a generic display technology. *IEEE Computer*, 38(8):46–53, 2005.
- [69] Y. Igasaki, F. Li, N. Yoshida, H. Toyoda, T. Inoue, N. Mukohzaka, Y. Kobayashi, and T. Hara. High efficiency electrically-addressable phase-only spatial light modulator. *Optical Review*, 6(4):339–344, 1999.
- [70] M. Booth, T. Wilson, H. B. Sun, T. Ota, and S. Kawata. Methods for the characterization of deformable membrane mirrors. *Applied Optics*, 44(24):5131–5139, 1999.
- [71] A. Jesacher, A. Schwaighofer, S. Fuerhapter, C. Maurer, S. Bernet, and M. Ritsch-Marte. Wavefront correction of spatial light modulators using an optical vortex. *Optics Express*, 15(9):5801–5808, 2007.
- [72] X. Xun and R. W. Cohn. Phase calibration of spatially nonuniform spatial light modulators. *Applied optics*, 43(35):6400–6406, 2004.
- [73] G. Donnert, J. Keller, R. Medda, M. A. Andrei, S. O. Rizzoli, R. Luhrmann, R. Jahn, C. Eggeling, and S. W. Hell. Macromolecular-scale resolution in biological fluorescence microscopy. *Proceedings of the National Academy of Sciences*, 103(31):11440, 2006.
- [74] G. Donnert, J. Keller, C. A. Wurm, S. O. Rizzoli, V. Westphal, A. Schönle, R. Jahn, S. Jakobs, C. Eggeling, and S. W. Hell. Two-color far-field fluorescence nanoscopy. *Biophysical Journal*, page doi:10.1529/biophysj.107.104497, 2007.
- [75] E. Auksorius, B. R. Boruah, C. Dunsby, P. M. P. Lanigan, G. Kennedy, M. A. A. Neil, and P. M. W. French. Stimulated emission depletion microscopy with a supercontinuum source and fluorescence lifetime imaging. *Optics Letters*, 33(2):113–115, 2008.

- [76] F. L. Bookstein. Principle warps: Thin plate splines and the decomposition of deformations. *IEEE Transactions on Pattern Analysis and Machine Intelligence*, 2(6):567–585, 1989.
- [77] V. Westphal and S. W. Hell. Nanoscale resolution in the focal plane of an optical microscope. *Physical Review Letters*, 94:143903, 2005.
- [78] P. Dedecker, B. Muls, J. Hofkens, J. Enderlein, and J. I. Hotta. Orientational effects in the excitation and de-excitation of single molecules interacting with donut-mode laser beams. *Optics Express*, 15:3372–3383, 2007.
- [79] E. Rittweger, K. Y. Han, S. E. Irvine, C. Eggeling, and S. W. Hell. Sted microscopy reveals crystal colour centres with nanometric resolution. *Nature photonics*, page DOI: 10.1038/NPHOTON.2009.2, 2009.
- [80] B. R. Rankin, R. R. Kellner, and S. W. Hell. Stimulated-emission-depletion microscopy with a multicolor stimulated-raman-scattering light source. *Optics Letters*, 33(21):2491–2493, 2008.
- [81] D. Wildanger, E. Rittweger, L. Kastrup, and S. W. Hell. Sted microscopy with a supercontinuum laser source. *Optics Express*, 16(13):9614–9621, 2008.
- [82] V. Westphal, M. A. Lauterbach, A. Di Nicola, and S. W. Hell. Dynamic far-field fluorescence nanoscopy. *New Journal of Physics*, 9(435):1–10, 2007.
- [83] Y. S. Bae, S. Moon, and D. Y. Kim. High-speed image acquisition synchronized with the motion of galvanometer scanner for confocal microscopy. *Proc. SPIE*, 6861:686116–8, 2008.
- [84] P. Verboven and B. Brugge. Einrichtung zur ablenkung eines lichtstrahls, 1990. DE Patent 4026130 A1.
- [85] J. Nurmi. *Processor Design: System-On-Chip Computing for ASICs and FPGAs*. Springer, Netherlands, 1th edition, 2007.
- [86] S. Back, P. Haas, J. Tschaepe, T. Gruebl, J. Kirsch, U. Mueller, K. Beyreuther, and S. Kins. In neurons app can be transported independent of any sorting signal to the axonal and dendritic compartment. *Journal of neuroscience research*, 85(12):2580–2590, 2007.
- [87] A. Moebius. *Der barycentrische Calcul*. unkown, 1827.
- [88] L. L. Song, C. A. G. O. Varma, J. W. Verhoeven, and H. J. Tanke. Influence of the triplet excited state on the photobleaching kinetics of fluorescein in microscopy. *Biophysical Journal*, 70:2959–2968, 1996.

-
- [89] T. Staudt, A. Engler, B. Harke, J. Engelhardt, and S. W. Hell. Reduction of excitation and signal suppression cycles (rescue) in zero based high resolution optical microscopy. *Optics Express*, page in preperation, 2009.
- [90] R. A. Hoebe, C. H. V. Oven, T. W. J. G. Jr., P. B. Dhonukshe, C. J. F. V. Noorden, and Manders E. M. M. Controlled light-exposure microscopy reduces photobleaching and phototoxicity in fluorescence live-cell imaging. *Nature biotechnology*, 25:249–253, 2007.
- [91] C. G. Dotti and K. Simons. Polarized sorting of viral glycoproteins to the axon and dendrites of hippocampal neurons in culture. *Cell, Cambridge, Mass.*, 62:63–72, 1990.
- [92] M Encinas, Y. Iglesias, Y. Liu, H. Wang, A. Muhaisen, V. Cena, C. Gallego, and J. X. Comella. Sequential treatment of sh-sy5y cells with retinoic acid and brain-derived neurotrophic factor gives rise to fully differentiated, neurotrophic factor-dependent, human neuron-like cells. *Journal of Neurochemistry*, 75:991–1003, 2000.
- [93] L. Zhu, P. C. Sun, D. U. Bartsch, W. R. Freeman, and Y. Fainman. Wave-front generation of zernike polynomial modes with a micromachined membrane deformable mirror. *Applied Optics*, 38(28):6019–6026, 1999.
- [94] N. Otsu. A threshold selection method from grey level histograms. *IEEE Transactions on Systems, Man, and Cybernetics*, 9:62–66, 1979.

A Appendix

Cell culture and immunocytochemistry

Crimson and Nile Red fluorospheres and gold spheres

The gold spheres (80nm) or Crimson or Nile red filled polystyrene micro spheres (specified diameter, 36nm Crimson; 21 nm Nile red; 2% solids in distilled water; Molecular Probes) were positioned onto a poly-l-lysine (Sigma, Germany) coated coverslips and mounted in DABCO containing Mowiol (Sigma, Germany) to avoid molecular diffusion.

Crimson fluorospheres on glycerol

Like proposed in [82], diffusing beads were prepared by first cleaning the cover slip with detergent Mucosol and making the surface of it hydrophilic in a plasma cleaner. After passivating with 1M NaOH 36nm Crimson fluorospheres (Invitrogen, Germany) were mixed with 20 µl glycerol and 1 µl of 10M NaOH. This mixture was spincoated onto the cover slip at 10000rpm.

APP: N2A cell preparation for living cell measurements

N2a cells were grown on FluoroDish (World Precision Instruments, USA). One hour before transfection growth media was replaced by OptiMEM (Invitrogen, Germany). For transfection 6 µg plasmid DNA (pcDNA3.1(+)_APPntmyc) was diluted in 200 µl of pre-warmed OptiMEM and mixed gently. In a second Eppendorf tube 6 µl Lipofectamin 2000 were mixed with 200 µl OptiMEM, and incubated for 5min at room temperature. For complex formation the diluted DNA and diluted transfection reagent were combined, inverted several times, and incubated at room temperature for 20min. The cells were washed twice with 1x PBS, before the mixture was added drop-wise onto the cells and cells were then incubated at 37°C and 5% CO₂. The media was replaced by normal growth media after 3-5h. 18-19h after transfection dishes with transfected cells were placed on ice to block endocytosis and incubated with cold OptiMEM containing Atto633 (Atto-tec, Germany) conjugated anti-APP antibody (6E10, mouse anti-A ; monoclonal, Signet, Germany) for 30min. Then, cells were washed with ice cold 1x PBS, prewarmed culture medium was added and cells were directly investigated by STED microscopy.

APP: primary mouse neurons (DIV8) preparation for RESCue experiments

Embryos (E14) from wt (C57BL/6NCrl; Charles River) mice were separated and dissociated mixed cortical neuron cultures were prepared as described previously [91]. Neurons were grown on poly-l-lysine-coated 15mm coverslips (Marienfeld, Germany) in serum-free Neurobasal Media (Gibco, Germany) with B-27 supplement (Gibco, Germany), 25 μ M glutamate (Sigma, Germany), and 0.5mM glutamine (Sigma, Germany). For immunocytochemical analysis, primary neurons were fixed with 4% PFA (Sigma, Germany) and permeabilized 10min with 0.1% NP-40/Nonidet (Fluka, Germany) in PBS. Cells were incubated with primary antibody (monoclonal anti-APP-antibody 4G8 (Chemicon, CA) diluted in 5% goat serum in PBS) at 4°C overnight, washed with PBS, incubated with secondary antibody (Atto565 goat anti-mouse IgG, 10 μ g/ml), and embedded in Mowiol (Sigma, Germany) on glass coverslips.

Primary human cells preparation for adaptive pattern scanning

The primary human fibroblast cells were fixed with 4.5% PFA (Sigma, Germany) for 10min and prepared with 0.1% in PBS triton x100 for 3min. The cells were blocked in 0.5% BSA in PBS for 10min. Before the incubation with the primary antibody, the cells were washed with 1x PBS and then incubated with anti-pax-antibody (Sigma, Germany) for 1h. After washing with 1x PBS the cells were incubated with Atto647N anti-rabbit-antibody for 1h. Finally after washing them for one night in 1x PBS the cells were mounted in Mowiol (Sigma, Germany) containing DABCO (Sigma, Germany) as an antioxidant.

Glioblastoma cell preparation for RESCue experiments

For immunocytochemistry, the U373 glioblastoma cells were seeded on standard glass coverslips to a confluency of 50-80% and permeabilized with cold methanol (-20°C) for 4-6min. The cells were subsequently washed in PBS with 1% BSA (blocking buffer) and incubated with primary antibodies (anti GFAP mouse IgG, Sigma, Germany). After 1h of incubation, the cells were washed with blocking buffer for 10min and incubated with secondary antibodies (Atto565 goat anti-mouse IgG) for 1h after the protocol from Molecular Probes, Carlsbad. For imaging, the cells were mounted in Mowiol (Sigma, Germany) containing DABCO (Sigma, Germany) as an antioxidant.

Immunostaining of the lamina of neuroblastoma cells

The SH-SY5Y neuroblastoma cell line was grown as described previously [92]. Cells were seeded on standard glass coverslips to a confluency of about 80%. For immunostaining of the nuclear lamina, the cells were fixed with 3.7 PFA for 15min followed by a 5min-treatment with Triton X-100. Before the incubation with the primary antibody, the cells were blocked in 1% BSA in PBS for 5min. Anti-lamin B1 rabbit IgG (Abcam, Cambridge, UK) was used as primary antibody, anti-rabbit conjugated Atto 647N IgG as secondary antibody respectively. Both antibodies were diluted in blocking buffer. Postfixation was carried out with 3.7% PFA for 10min. Cells were mounted in Mowiol.

Software

Each figure illustrates some part of the coding work done for the controlling software.

User interface of the SLM error correction and control software

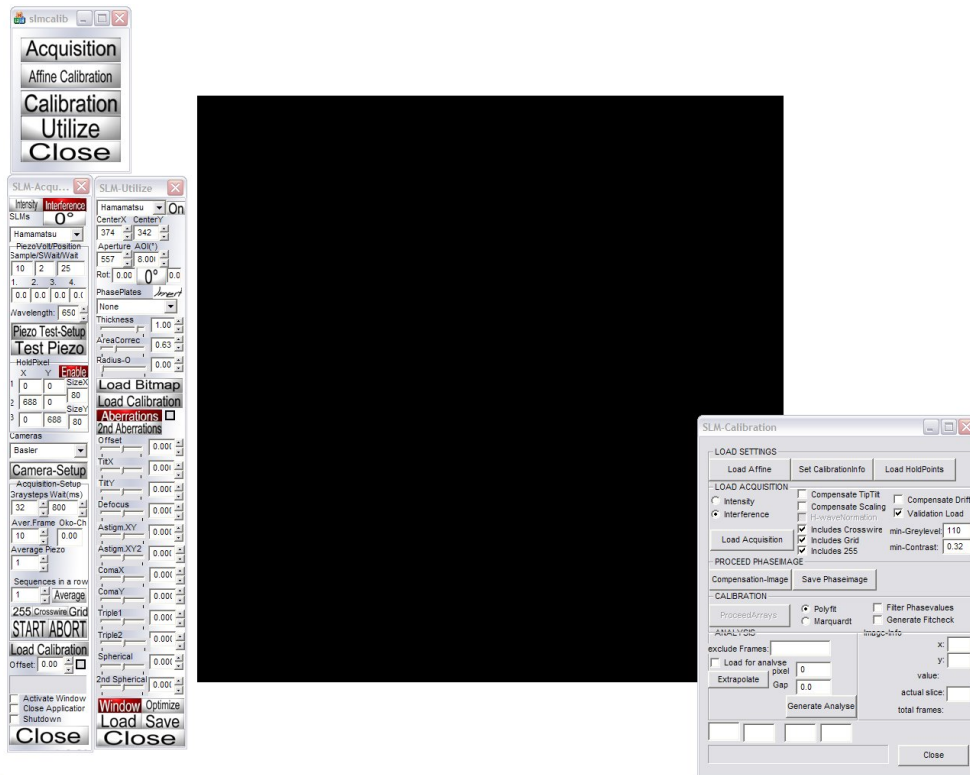


Figure A.1: The GUI for the SLM error correction and the control GUI for aberration correction

The implementation of the scanning software in Labview

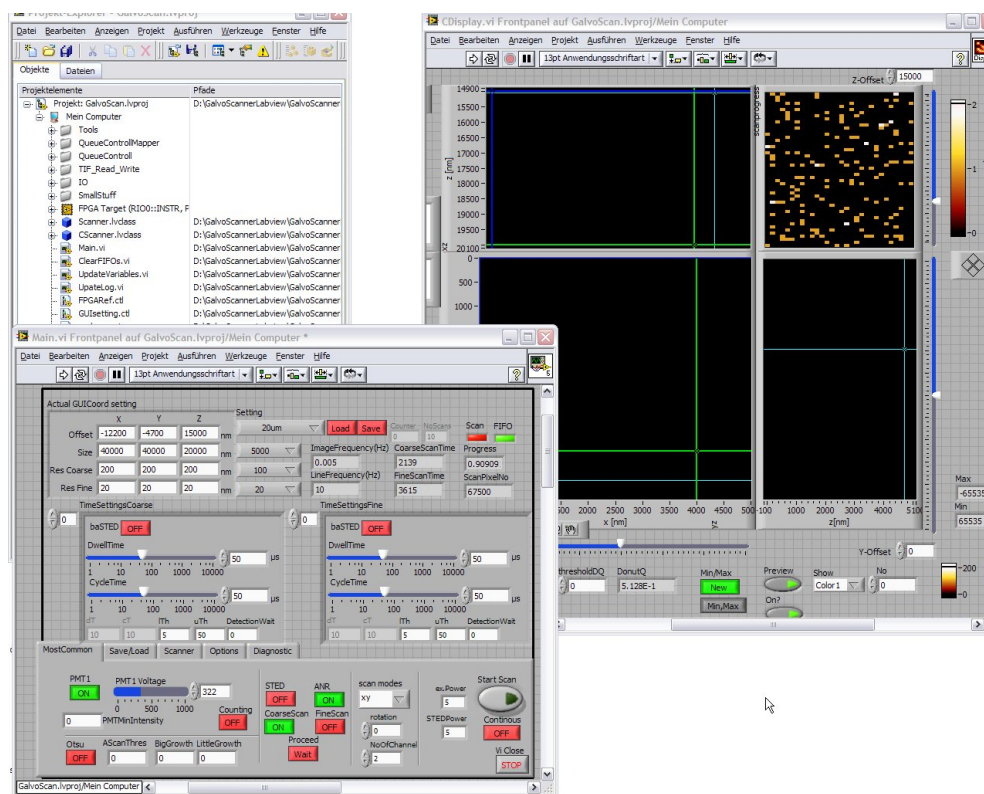


Figure A.2: The scanner software

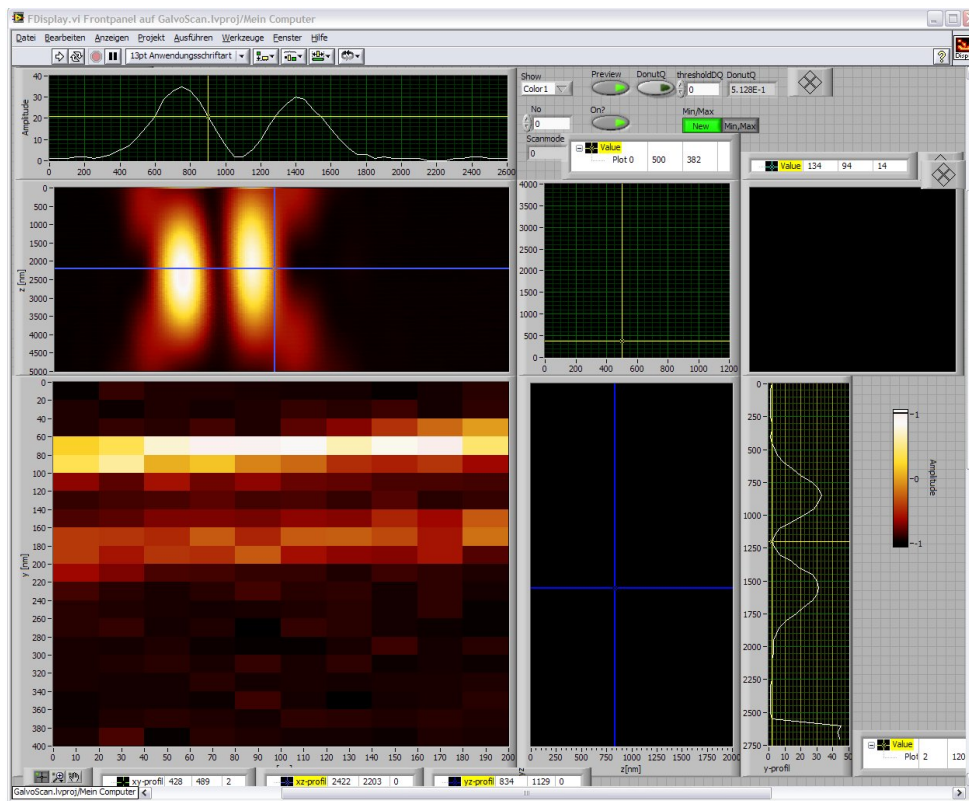


Figure A.3: The scanner software

Figure A.4: A more detailed representation of one layer of the code written for the FPGA program

Aberration correction with SLMs

The use of a fully calibrated SLM goes beyond the possibility to apply any wanted phase mask. Since the SLM can be freely programmed even inside the optical path of the STED beam, it can be used to (pre-) compensated any phase error introduced by the setup.

Since each pixel can be adjusted independently an efficient way of controlling all pixels for aberration correction must be found. A commonly used set of orthogonal functions correlating with many known optical errors are the Zernike polynomials [93] .

To provide the aberration compensation the SLM control software was modified to produce the first 22 Zernike polynomials. Fig. A.5 shows the first eleven Zernike modes (the piston mode is not shown).

For the STED setup used for the experimental validation in this work no major degradation due to aberrations was detected. Hence, all measurements were performed by using only the Tip-mode. This mode was used to adjust a phase ramp onto the SLM to ensure a different STED PSF minimum position compared to the position of the reflected light of the coverslip.

IO Board layout for the FPGA card

For using the FPGA as a controlling device for the complete optical and electrical setup an additional IO board was designed to provide fast access to all analog and digital input and outputs. Fig. A.6 shows the designed PCB later constructed from the DKFZ Elektronikwerkstatt.

The use of additional pixels to provide smooth acceleration changes

Since the galvanometer driven mirrors perform two acceleration changes at the beginning of each scanned line, the first pixels in each line are erroneous. An implementation of a bi-directional scan would reduce the number of erroneous pixels but would not completely solve the problem. Instead a number of interpolation coordinates are feed to the scanner for each performed jump to provide a more continuous acceleration change. These, so called insert pixels, are not only calculated at the beginning of each line but are also necessary for the adaptive scan pattern.

The insert pixels lead to error free images even for fast scans but decrease the efficiency of the duty cycle for a smaller number of line pixels.

The user or an automatic routine can provide the number of insert pixels. The








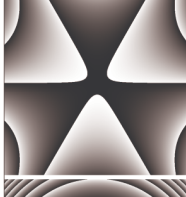

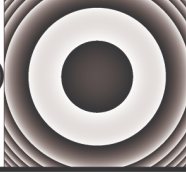
Term	$Z_i(r, \theta)$	Image	Term	$Z_i(r, \theta)$	Image
Tip	$2r \cos \theta$		ComaX	$\sqrt{8}(3r^3 - 2r) \cos \theta$	
Tilt	$2r \sin \theta$		ComaY	$\sqrt{8}(3r^3 - 2r) \sin \theta$	
Defocus	$\sqrt{2}(2r^2 - 1)$		Triple1	$\sqrt{8}r^3 \cos 3\theta$	
Astigmatism1	$\sqrt{6}r^2 \sin 2\theta$		Triple2	$\sqrt{8}r^3 \sin 3\theta$	
Astigmatism2	$\sqrt{6}r^2 \cos 2\theta$		Spherical	$\sqrt{5}(6r^4 - 3r^2 + 1)$	

Figure A.5: The figure displays the first 11 Zernike polynomials, excluding the zero order piston mode. On the left their commonly used designation is shown, followed by their function description in spherical coordinates and last an image representation of the Zernike mode out of the control software.

routine considers the distance of the maximal jump d_{max} and the set dT to calculate the number of interpolated pixels no_{ip} using

$$no_{ip} = \frac{d_{max} 40 \mu s}{2 \mu m dT} + \frac{80 \mu s}{dT} \quad (A.1)$$

Hereby, the first term describes the time needed for the scanner to rotate over a certain distance. The second term represents the time for two inertia changes typically needed for each jump.

With a scan line consisting out of 60 pixels the theoretical limit of the effective dT would be $2.7 \mu s$ as can be seen by

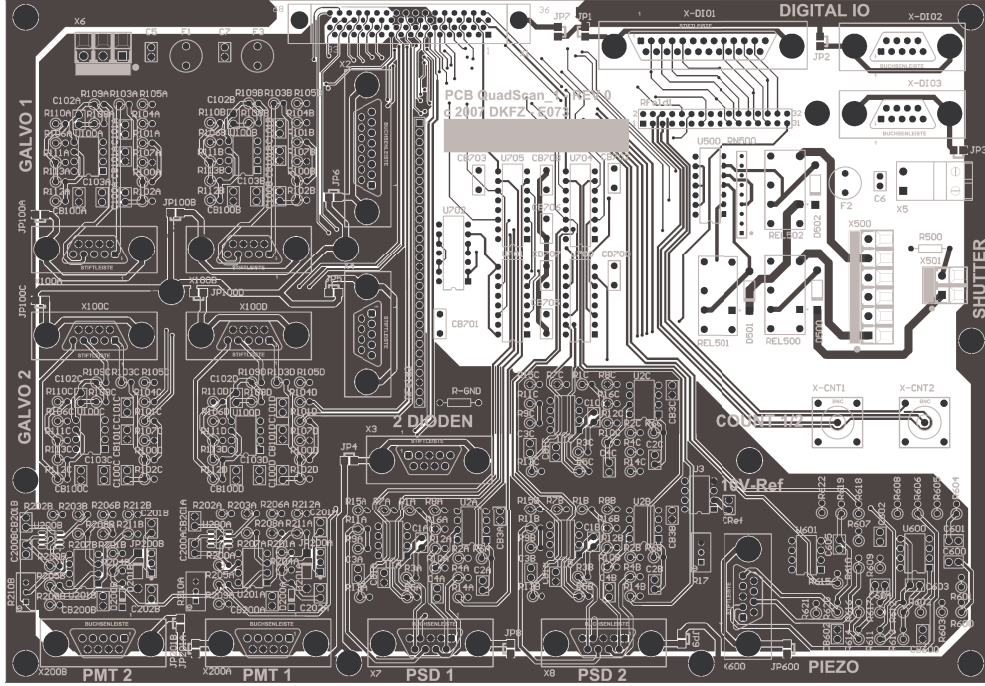


Figure A.6: The figure illustrates the manufactured PCB for the used IO-board.

$$dT_{eff} = \left(\frac{no_{ip} + pixel_{line}}{pixel_{line}} \right) dT, \quad (A.2)$$

where $pixel_{line}$ is the number of pixels per line and dT_{eff} represents the effective dT.

It is also clear that a higher number of pixels per line leads to a better duty cycle and shorter possible effective dTs.

Algorithms for adaptive pattern scanning

For the adaptive pattern scanning a threshold is used. All pixels with photon numbers below this threshold do not contribute coordinates to the adaptive scan pattern whereas the coordinates of all pixels above the threshold are sorted into the scan pattern.

The threshold can be provided by the user. Since the user has to determine the typical photon numbers of pixels with fluorophore information, this is a time consuming task, which limits the usability of the adaptive scan pattern. Especially for samples with high photo bleaching the threshold must be adjusted after each

coarse scan.

In order to circumvent this problem an automatic routine must supply the required threshold in a much shorter period of time than the complete image acquisition time. One possible algorithm fast enough to provide a reliable threshold for fluorophore images is a threshold algorithm according to Otsu [94]. It assumes two distributions present in the image. This premise is fulfilled by all monochromatic fluorescence images. All presented adaptive measurement applied the Otsu segmentation routine.

The first implementation of the concept resulted in a pixel shift between the coarse and the fine scan pattern information. This problem is not inertia dependent as the erroneous pixels after jumps but results from different scanner speeds. An analysis of the scanner behavior for different speeds revealed a linear dependency between the induced pixel shift and the scanner speed (see fig. A.7). The data was acquired by measuring the introduced shift of the center of the excitation PSF due to different mirror rotation speeds. The software was adapted using this linear pixel shift function between the coarse and the fine-scan for all presented experimental data.

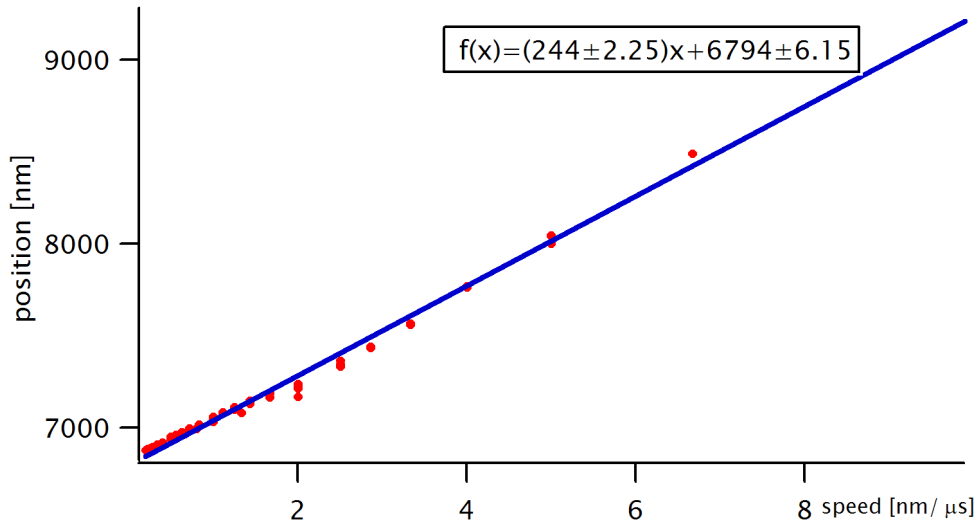


Figure A.7: The figure shows the induced pixel shift due to different scan speeds. The red points represent the measured data. The blue line shows the linear least square fit of the experimental data. The linear fit represents a good approximation of the real function.

Acknowledgements

The SLM error correction was performed in the department of NanoBiophotonics at the Max-Planck-Institute for Biophysical Chemistry in Göttingen. The rest of the thesis was carried out at the department of high resolution optical microscopy at the German Cancer Research Center in Heidelberg.

First of all, I want to thank Prof. Dr. Stefan W. Hell without his ideas nothing of this would be possible. He not only proposed this challenging project but delivered all the needed support to accomplish it successfully. His great input and the profound discussions with him gave me new insights into so many topics.

Next, I would like to thank Prof. Dr. Karl-Heinz Brenner at the Institute for Computer Engineering of the University of Heidelberg, for the interesting discussions and his time and support as a referee of my thesis.

Special thanks go to Dr. Johann Engelhardt. Through his intensive knowledge in electronics, optics and work-flows I learned essential things for this thesis.

A major part of the experimental measurements were not possible without the extensive help of our collaborators. I like to thank

- Jasmin Zahn from the group of Prof. Dr. Joachim Spatz from the MPI Stuttgart for the focal adhesion samples
- Simone Back from the group of Prof. Dr. Stefan Kins from the ZMBH Heidelberg for the APP samples of primary mouse neurons and living N2A cells
- Silvia Löbermann from the MPI Göttingen for the preparation and prompt delivery of any needed antibody.

I have to thank Prof. Dr. Wolfgang Semmler and Prof. Dr. Joachim Spatz for being my promoters for the DKFZ PhD program.

I want to thank my co-workers at the DKFZ for their cooperation, their friendship and the very pleasant time.

Foremost, I want to thank Matthias Reuss with whom I shared the STED setup and whom did the complete optical and mechanical design of it. Without his support most of the thesis would be theory.

Further thanks goes to Thorsten Staudt and Dorothea Hahn. I had many good discussions with you and the time would not have been fun without you two. Next, I want to thank Jale Ozcelik for being the organizing head of the departments leisure times.

Additionally, I want to thank Matthias Reuss, Thorsten Staudt, Dr. Johann Engelhardt and Pit Bingen for the extensive and nerve-racking proof reading of this manuscript.

Moreover, I want to thank the following member of the department of NanoBio-photonics for their help and support during my time at the MPI:

- Dr. Christian Eggeling for the help when it was needed most
- Dr. Volker Westphal for his supervision of the SLM project and proof reading
- Dr. Lars Kastrup for his extensive support with ideas and proof reading
- Dr. Robert Kellner for extensive help with PSF measurements and Latex
- Dr. Jan Keller for simulations and discussions about programming
- Dr. Arnold Giske for the best experimental advice.
- Harald Meyer for technical assistance.
- Jaydev Jethwa for technical assistance and proof reading
- Brian Rankin for supportive assistance and good dialogs
- Dr. Stefan Bretschneider, Dr. Martin Andresen, Dr. André Stiel for good dialogs and nice badminton games

A great thanks to the optical and mechanical workshop in Göttingen and even greater thanks to the electrical workshop around Jürgen Vierling and the mechanical workshop around Heinrich Rühle. All departments contributed essential parts to the STED setup.

I want to thank my parents for their ongoing support and Boris, Rosa and Sergej Woronkow to always give me the feeling to be at home. Last, I want to thank Olga Woronkow. It was a hard time. Thanks, that you are still with me.

Heidelberg, April 2009

